Advancements in MRI Temperature Map Reconstruction for Real-Time Guidance of Thermal Therapies

By

Pooja Gaur

Dissertation

Submitted to the Faculty of the

Graduate School of Vanderbilt University

in partial fulfillment of the requirements

for the degree of

DOCTOR OF PHILOSOPHY

in

Chemical and Physical Biology

May, 2016

Nashville, Tennessee

Approved:

E. Brian Welch, Ph.D.

William A. Grissom, Ph.D.

Charles F. Caskey, Ph.D.

Ted L. Anderson, M.D., Ph.D.

Thomas E. Yankeelov, Ph.D.

ACKNOWLEDGMENTS

Chapter 3 appears in its entirety as: Gaur P, Grissom WA. Accelerated MRI thermometry by direct estimation of temperature from undersampled k-space data. Magnetic resonance in medicine. 2015 May;73(5):1914-25.

Chapter 5 appears without the appendix as: Gaur P, Partanen A, Werner B, Ghanouni P, Bitton R, Butts Pauly K, Grissom WA. Correcting heat-induced chemical shift distortions in proton resonance frequency-shift thermometry. Magnetic resonance in medicine. 2015 Aug; *In press*.

TABLE OF CONTENTS

LIST OF TABLES

LIST OF FIGURES

Chapter 1

Introduction

1.1 Synopsis

The overall goal of the work presented in this thesis is the development and validatation of accelerated magnetic resonance imaging (MRI)-based temperature reconstruction algorithms for use with volumetric heating treatments. Recent technological developments have combined thermal therapies for patient treatment with MRI for assessment of temperature changes in the brain and body. In particular, MRI-guided focused ultrasound (MRgFUS) is increasingly being used to treat cancer [1, 2, 3, 4], relieve pain from bone metastases [5, 6], stimulate deep brain tissue to treat neurological conditions [7], and facilitate drug delivery across the blood-brain barrier [8]. MRgFUS-induced gene expression has also been demonstrated in animal studies [9].

Although therapeutic applications of MRgFUS are increasing, their potential is fundamentally limited by the ability to measure temperature changes accurately and quickly throughout the body. MRI-based temperature maps can address these limitations noninvasively [10], and offer the advantages of high spatial resolution, excellent soft tissue contrast, and a simple (linear) measurement of temperature over the typical treatment range [11]. Currently, many MRgFUS treatments are limited to 2D imaging in only the few centimeters around the heating target. Faster temperature measurements are needed to allow the entire area exposed to ultrasound energy to be imaged within an acceptable time frame for guiding and monitoring treatment. Accurate and volumetric measurements are necessary to (1) validate that the treatment is optimally delivered to the tissue of interest, (2) enable continuous volumetric treatment, and (3) ensure that exposure to the surrounding tissue is limited. Restrictions imposed by the ultrasound equipment limit the number of image coils that can be placed near the body, reducing the potential of parallel imaging techniques

to accelerate MRI scans. Therefore, data undersampling is needed to achieve higher spatial coverage without sacrificing temporal resolution. The developments presented in this thesis were formulated to promote robust, real-time MRI reconstruction methods that produce accurate temperature maps from undersampled data. With this in mind, the objectives addressed in later chapters are as follows:

Chapter 3: Reconstruct temperature maps from highly undersampled data. We propose to accelerate temperature estimation by fitting undersampled k-space data to a highly constrained model. We solve for the phase shift resulting from the change in proton resonance frequency (PRF) with temperature, where the overall image magnitude is expected to match that of an image collected before heating. This approach will resolve temperature changes at full temporal resolution, since it does not rely on smoothing across time to suppress aliasing artifacts.

Chapter 4: Reconstruct temperature from undersampled brain MRgFUS data using spatial segmentation. Temperature monitoring during MRgFUS procedures in the brain is currently limited to a single image slice. Between focused ultrasound sonications, circulating water prevents skull overheating, but also creates signal variations that disrupt correlations between images collected before and during treatment (which are relied on to overcome undersampling artifacts), leading to errors in temperature measurements. We propose a spatially-segmented iterative reconstruction method, which applies the k-space hybrid model (developed in Ch 3) to reconstruct temperature changes in the brain and a nonlinear conjugate gradient method to reconstruct the image in the water bath.

Chapter 5: Correct chemical shift image distortions that arise from tissue heating. Tissue heating results in a change in PRF and can be measured directly from a change in image phase. However, the PRF change also leads to a spatially dependent chemical shift that distorts the image if left uncorrected. We will fit a constrained model of the temperature phase shift and off-resonance term to the k-space data. Since the temperature-induced phase change will be determined prior to image reconstruction, we hypothesize the

chemical shift can be corrected to produce an undistorted image.

Results outline the development of a constrained model that is fit directly to undersampled k-space measurements to accelerate data acquisition and reconstruction during treatment procedures. Reconstruction directly from k-space produces images and temperature maps that are free of chemical shift distortion and undersampling artifacts, without loss of temporal resolution. The presented methods will readily extend to 3D imaging, thereby facilitating volumetric measurements during interventions. This will permit more accurate targeting of heating focal points, expand imaging coverage to allow continuous treatment across a volume, and improve safety by providing a more complete picture of treatment effects in the body. Advancements in these areas will help enable treatments that cannot be performed safely and effectively with the current technology.

1.2 Significance

Thermal interventions are an alternative to certain traditional surgical procedures, with the number and use of applications increasing with the development of new technology [12]. With phased array transducers, ultrasound energy is generated outside the body and delivered noninvasively to a specific location within the tissue. This technology can deliver treatment to deep tissue without damaging the intervening structures between the treatment target and the transducer [13, 14, 15, 16, 17, 18]. Additionally, focused ultrasound can achieve high intensity energy deposition within a narrow target area [19, 20, 21, 22]. This technique is especially useful for treating regions with small functional areas and densely packed structures where surgery or other interventions may be difficult or unsafe [23, 24, 25]. Because these methods deposit energy across a volume in the body, it is necessary to measure temperature rises throughout the tissue to ensure patient safety during the treatment. Excess or unintentional heat deposition could occur through error or because of proximity to high absorption areas, such as bone [20]. Invasive probes provide thermometry measurements, but are limited to recording at one spatial location and may interfere

with ultrasound energy propagation [26]. Volumetric rather than single-point temperature measurements are needed to adequately monitor heating induced by the intervention and to enable continuous volumetric treatment. MR thermometry provides quantitative temperature imaging with sufficient sensitivity to resolve temperature changes at levels below the threshold for tissue damage [27, 28]. Effectively, this is a map of heating in the body that provides both reliable visualization of the tissue and measurement of treatment effects. However, improvements in thermometry accuracy and spatio-temporal resolution are needed to enable emerging MRgFUS treatments and determine their feasibility [10]. The objective of this work is to develop and validate a method for volumetric MR thermometry at a high frame rate, which will improve the accuracy, safety, and efficacy of thermal therapies such as MRgFUS.

1.2.1 The patient context

1.2.1.1 Early advances in focused ultrasound therapy

Focused ultrasound was first introduced in the 1940s, with demonstrations of brain lesion formations with craniotomy in feline, canine, and non-human primate studies [13, 19]. Noninvasive, targeted lesion formation were further demonstrated in animals in the 1950s. Histological studies revealed the localized thermal effect and showed that lesions were produced without damage to intervening tissue [23, 29]. In the late 1950s, reversible neuronal activity in response to focused ultrasound stimulation in the cortex and spinal cord was observed in felines [30, 31]. Limitations were noted in treatment targeting and evaluating the extent of thermal damage in vivo.

A transducer system for human treatment was developed and used to treat patients with Parkinson's disease. A sterotactic frame and X-ray imaging provided reference for guiding the treatment. These treatments demonstrated clinical feasibility of focused ultrasound for selectively targeting subcortical brain structures to treat neurological conditions without

damaging other brain regions [32]. Neurological treatments were also performed in patients to successfully relieve pain from neuromas, which were carefully located prior to treatment administration, and other sources of pain from trauma or illness [31, 33].

Mechanisms of tissue modulation were observed based on the acoustic intensity applied. Thermal effects were attributed to lesion formation at low intensity and long treatment exposure times. At increased intensities, lesions were produced by mechanical effects. At high intensity and short duration, lesions were created by cavitation. Lesions from cavitation formed more quickly than thermally-induced lesions and were more likely to occur at tissue and fluid boundaries than at the ultrasound focus, where agitation and collapse of bubbles produced tissue damage [34].

Ultimately, the inability to image brain structures in individual patients, to determine the focal spot of the ultrasound beam for accurate positioning prior to creating permanent thermal lesions, and to obtain feedback of thermal dose delivery during treatment were major limiting factors in the progression of focused ultrasound therapy [35].

1.2.1.2 MR-guided focused ultrasound surgery

The development of MRI, remarkable on its own, held revolutionary potential for meeting the unmet needs of focused ultrasound applications. In the early 1990s, MRI was proposed for imaging focused ultrasound treatment and demonstrated to be effective in planning, monitoring, and evaluating lesion formation [36, 37, 38]. Focal heating effects were observed in real-time from signal intensity changes in magnitude images during ultrasound sonication [37].

As a noninvasive and highly localized therapeutic modality, MRgFUS is a compelling alternative to traditional surgery. Invasive surgical procedures carry higher anesthesia risks, long recovery times, greater collateral damage to tissue, and risks of bleeding and infection [7]. However, surgery readily allows the collection of tissue and tumor samples, permitting the study of molecular markers [39]. Treatment efficacy has been shown to be high with

proper MRgFUS targeting [40, 41, 42]. In situations where traditional therapies are not available, such as in the treatment of inoperable brain tumors or drug-resistant illness, or where existing treatment comes at high personal cost, like loss of fertility, MRgFUS offers a unique opportunity for patient care [3, 4, 43, 44].

1.2.1.3 Neural applications of MRgFUS

Brain treatment has been described as an ideal application for MRgFUS, which provides the opportunity to non-invasively and repeatably deliver targeted thermal energy without damaging intervening tissue under real-time, non-ionizing image monitoring [10]. As such, MRgFUS can potentially reach neural targets that are too risky to treat with other surgical methods such as incision, deep-brain stimulation, and radiofrequency ablation, while also reducing risks of bleeding and infection [7, 4, 45].

Whereas most applications of MRgFUS employ an ultrasound transducer that is placed generally just outside the body, an even more specialized device is required for delivering therapy through the skull. The current state-of-the-art MRgFUS system for brain treatments uses a helmet-like array of transducers that surrounds the patient's head (Fig 1.1). The gap between the head and the transducer array is filled with cool water, which is circulated after each focused ultrasound sonication to reduce heating in the skull (which absorbs 30-60$\times$ more acoustic energy than tissue [4]). The development of this equipment, combined with tools to compensate for ultrasound phase aberrations caused by varying skull thicknesses, has enabled transcranial applications of MRgFUS which target central regions of the brain [10, 7, 4, 46, 47].

Following preclinical validations of transcranial MRgFUS technology in the mid-2000s, thermal ablation treatments in patients have been on the rise [48]. The first transcranial MRgFUS treatments began in 2008 for glioblastoma and neuropathic pain [7, 4]. Although these initial glioblastoma treatments were successful in MRgFUS targeting, it was not until 2014 that enough thermal energy to cause tumor damage was administered [49]. February

2011 marked the beginning of clinical trial treatments for essential tremor targeting the thalamus [44, 50, 45]. MRgFUS treatments for Parkinson's disease began as early as 2012 [51, 52]. Clinical trials for MRgFUS treatment for obsessive-compulsive disorder started in 2013 [53]. In 2015, a clinical trial using MRgFUS to treat patients with depression began. In addition to surgical applications, non-thermal treatments are also being performed, in which ultrasound energy is used to stimulate tissue without delivering heat. Notably, in November of 2015, MRgFUS was first used to momentarily open the blood-brain barrier to deliver targeted chemotherapy drugs to a brain tumor in a patient [8]. Additional MRgFUS applications, such as vascular surgery and liquification of blood clots in the brain, have also been proposed [16, 54]. These pioneering and rapidly advancing applications of brain MRgFUS therapy have been fundamentally enabled by recent technological developments, including improvements in transcranial focused ultrasound devices and real-time treatment imaging.

Though central to the success of these treamtents, the hemispheric transducer array also creates unique challenges for MR imaging. It partially shields the head from radiofrequency pulses that are applied to generate MR signal and also hampers signal reception. Its size and positioning prevent the use of MR head coils by occupying the space immediately around the head, and the body coil is typically used to transmit and receive signals instead [55]. Since MR receive coils are not located close to the body, the relative signal to noise ratio in images is poor. To accommodate the water bath, the imaging field of view must be larger than would otherwise be prescribed for brain imaging, increasing the scan acquisition time. Perturbations in the water bath from ultrasound pulses and motion from water circulation during dynamic image acquisition also cause aliasing of signal in the brain. Aliasing of the water bath signal into the brain region is especially problematic for model-based temperature reconstruction from undersampled data since the water motion is unpredictable.

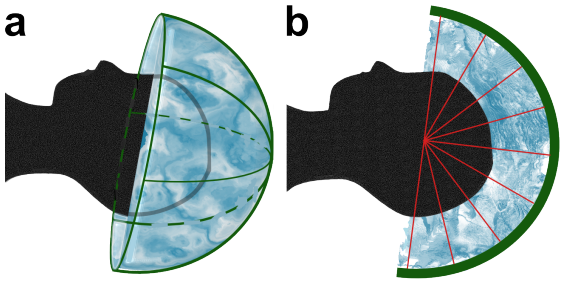

Figure 1.1: Illustration of transcranial MRgFUS setup. (a) The hemispheric transducer (green) surrounds the patient's head with an intervening water bath (blue) for ultrasound coupling. (b) Cross-sectional view depicts a central focus produced by converging ultrasound waves originating from transducers along the hemispheric array (red lines). Water is circulated through the bath between sonications to cool the skull.

1.2.1.4 Treatment setup

MRgFUS treatments are usually carried out at 1.5 or 3T MRI scanners. Conscious sedatation is provided to minimize patient discomfort and motion [56]. For transcranial MRgFUS, the patient's head is stabilized in a stereotactic frame after application of a local anesthetic [47]. Accurate mapping of skull density and thickness is essential to the success of transcranial MRgFUS treatments, since transducer phase delays must be accurately tuned in order to achieve ultrasound focusing in the brain [57]. Failure to achieve intracranial focusing or sufficient thermal deposition results in under-treatment and reduced therapeutic efficacy [4]. Phase correction factors for transcranial MRgFUS are derived from prior X-ray computed tomography (CT) scans. The transcranial transducer operates at a lower frequency than the body transducer (650 kHz instead of 1 MHz range) to reduce heat absorption in the skull, and produces a $3\times3\times4$ mm^3 focal spot [58]. Focal spots with 4, 8, 12, and 16 mm diameters and lengths of a few cm can be produced using the body transducer [59, 3].

T_1-weighted images are acquired for treatment planning and verifying that the transducer beam has a clear path to the targeted regions. Temperature imaging scans are collected during therapy under the control of the MRgFUS treatment software, which adjusts the scan duration and image placement for each sonication. To verify focal spot location,

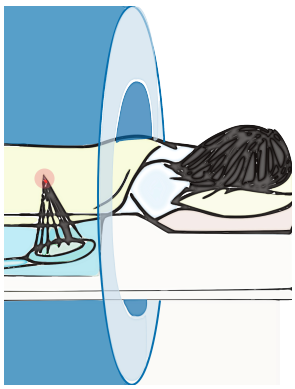

Figure 1.2: Illustration of body MRgFUS setup. An ultrasound transducer embedded in the MRI table (highlighted in blue) delivers energy to selectively heat a single focal point (highlighted in red) in the body, without affecting any intervening tissue.

test sonications producing small temperature rises are performed prior to treatment. The patient can interrupt the treatment at any time using an emergency stop button.

Most MRgFUS transducers deliver energy from outside the body. The transducer is placed near the patient or, in the case of tabletop systems, the patient is positioned on an MRI table with an embedded transducer (Fig 1.2). Energy is delivered into the body in a relatively broad shape which narrows as distance from the transducer increases, until the ultrasound waves come together like the tip of a cone. The waves converge at the focal point of the transducer, where they add constructively. Outside of the focus, the ultrasound waves are out of phase and have no net effect. Therefore, by design, it is only at the focal point that MRgFUS treatment is delivered. The focal target can be chosen at different locations and depths in the body within the transducer range.

1.2.1.5 Targeted thermal heating

When applied at high intensity, ultrasound waves can impart enough heat into tissue to cause irreversible cell damage. Once the cells reach temperatures above 50°C, a physical change occurs [60, 61]. Protein denaturation causes irreversible cellular harm known as coagulation, and is observed at a range of 55°C-95°C for different proteins. However, many critical proteins in tissue reach the coagulation threshold at 60°C [61]. In practice,

MRgFUS procedures typically heat tissues to above 55-60°C, in order to trigger cell death in the area being treated [43].

Thermal ablation results in the formation of lesions within the focal region of the transducer, which is an ellipsoidal shape, with a small transition zone between damaged and healthy tissue [62]. MRgFUS sonications that cause peak tissue heating of 55-60°C typically result in visible lesions on the order of 3-5 mm in diameter, with better than 1 mm targeting accuracy [58, 63, 47]. To ablate larger volumes, sonications are applied sequentially until the small lesions are sufficient to cover the desired treatment area. Since the lesions are ellipsoids, treatment planning includes some overlap between focal targets to reduce gaps of untreated tissue within the area outlined for MRgFUS therapy. If the water in tissue is reaches its boiling point, bubbles arise and lesions are formed in an irregular and unpredictable shape. Therefore, to systematically cover a volume with overlapping lesions, a cooling period is needed before successive sonications [64].

The extent to which thermal damage occurs and lesions are formed depends heavily on the intensity and exposure time of the tissue to heat [62, 61]. To characterize the amount of energy absorbed by tissue at a given temperature T and time t, thermal dose is measured. The accumulated thermal dose is expressed in terms of the equivalent number of minutes of exposure at 43°C using the relation

$$t_{eq}(t) = \int_0^t C^{(43-T(s))} ds \tag{1.1}$$

where C is equal to 0.5 at temperatures above 43°C and 0.25 below 43°C [65, 66]. Although biological effects vary by tissue, coagulative necrosis is considered to occur when thermal dose exceeds 240 equivalent minutes (Table 1.1).

Importantly, thermocoagulation is limited to tissue at the focal target of the ultrasound transducer under normal circumstances [62]. However, there are risks that unintentional heating could occur outside of the focus where variations in tissue composition arise. Heat

Table 1.1: Thermal dose thresholds

Equivalent minutes	Effect
0-30	No thermal damage
30-240	Possible thermal damage
over 240	Irreversible thermal damage

absorption from ultrasound depends on tissue properties, and can be heightened at boundaries between tissue and air or bone, where speed of sound changes can cause propagating waves to reflect back from tissue interfaces. Tissue overheating can cause thermal damage or pain and, therefore, caution should be exercised when administering treatments [67].

1.2.1.6 Injuries, and the need for image guidance and monitoring

In a study of 1038 patients, initially 10-20% had burns after focused ultrasound surgery without MRI guidance [68]. This rate was reduced to less than 5% by the end of the trial, which is attributed to improved expertise in administering the treatment and identifying signs of tissue damage using ultrasound imaging. In a recent study, 100% of 114 patients treated for liver and pancreatic tumors experienced injuries along the abdominal wall following focused ultrasound surgery without MRI guidance [69]. These injuries, as well as injuries to the ribs and surrounding soft tissue, may be a result of energy reflection and absorption from air-tissue and bone interfaces.

While not common, burns on the skin or in other tissue have been reported as adverse effects from MRgFUS treatments [70]. Injury from unmonitored lipid heating is of particular concern in tissues with high fat composition, such as breast and fatty tissue surrounding other organs [71, 72, 73]. However, because MRgFUS treatments direct energy through the skin and fatty tissue, this type of injury is always possible. This is particularly true because repeated sonications are typically needed to fully treat a target, which result in accumulation of heat in the tissue near the transducer [38].

MR thermometry during treatment improves safety monitoring in aqueous tissue [38,

21], but typically excludes signal from lipids. Effectively, this leaves adipose tissue unmonitored. Using MRgFUS with fat-suppressed imaging, 2 of 6 patients treated for uterine leiomyomas experienced skin burns and blisters on the abdominal wall [3]. Of 28 breast cancer patients treated with fat-suppressed MRgFUS, one was discovered to have a severe skin burn [40]. This injury resulted from poor treatment administration throughout the session, and was not discovered until the session ended. With adequate temperature monitoring, including in adipose tissue, these types of injury can be detected and limited [72, 74].

1.2.2 Accelerated temperature imaging for volumetric feedback

For effective feedback during therapy, temperature maps should be generated in real-time as the treatment progresses [26]. Since the measurements are time-sensitive, they lose relevance after too long a delay. At temperatures close to 50°C, a significant effect on the tissue can occur in a time window of only a few seconds [75]. Increases of 3°C/s in the target region, with doubling of thermal dose rate every 1°C, can occur during typical treatments [76]. Recently, techniques for real-time thermometry covering a spatial window around the heating target have been reported [77, 78, 79, 80]. However, significant heating can occur outside of the targeted area. Therefore, accurate maps of temperature change throughout all of the tissue exposed to treatment are needed to ensure patient safety [72].

An example of a typical temperature imaging acquisition for MRgFUS in the body is six 2D slices collected in 3 seconds with a spatial resolution of $2.5\times2.5\times7$ mm^3 (Fig 1.3). Of these, three slices are centered at the heating focus, perpendicular to the ultrasound beam propagation, and one is positioned parallel to the beam path. The remaining two slices are placed near the skin surface and beyond the focus to monitor unintentional heating outside the treatment zone [59, 72]. This imaging protocol limits sonications to only one focal location at a time and requires repositioning of image slices between each sonication, thereby precluding the use of more efficient sonication trajectories. In particular, multi-

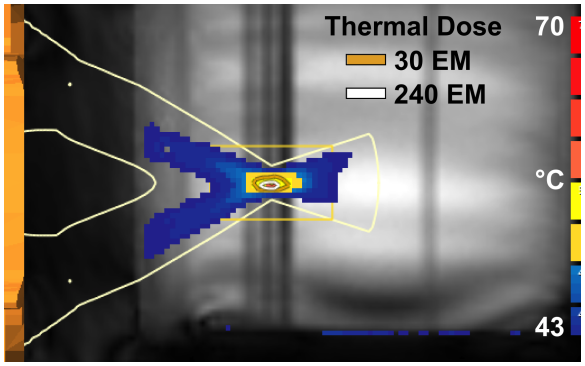

Figure 1.3: MRgFUS temperature and thermal dose maps. The color-coded temperature map is displayed over a gel phantom image. The transducer is depicted in gold at the far left, with the ultrasound beam path toward the treatment focus (centered in the yellow box) outlined in off-white. Thermal dose contours at the focus outline regions of thermal damage at 30 (orange) and coagulation at 240 (white) equivalent minutes (EM). Six images are collected for temperature monitoring every 3 s with a spatial resolution of $2.5\times2.5\times7$ mm^3. Dark vertical bands indicate the location of near-field (left-most), focal (center 3), and far-field (right-most) image slices.

focal sonications target multiple locations simultaneously, reducing long treatment times [81]. This setup also cannot fully detect excessive heating that can occur between the transducer and the thermal target, or beyond the ultrasound focus, particularly near acoustic interfaces in the body. For brain MRgFUS applications, temperature monitoring consists of only one imaging slice with 3-5 mm thickness with updates every 5 s [4, 82].

It is not viable to simply extend the current scan protocol for thermometry to increase spatial coverage. This would lead to long scan durations and a loss of temporal resolution in monitoring thermal changes, because the scan time for PRF imaging needs to be sufficiently long to acquire images with good phase contrast. Specifically, the signal in a gradient echo sequence is optimized when the echo time is on the order of the T_2^* relaxation time of the tissue [83, 84] and the repetition time is long [83]. Therefore, some form of acceleration, either in image acquisition or data reconstruction, is needed to enable 3D coverage.

MR methods such as parallel imaging [85] and compressed sensing [86, 87] have been proposed for accelerated thermometry, but are insufficient on their own to provide the needed acceleration for thermometry applications because of limited MR coil access [76].

These methods rely on many coils in close proximity to the body, but it is not feasible to place a large number of coils near the body without obstructing the ultrasound path. As a result, development of ultrasound-compatible coil arrays are currently an active area of research [88, 89, 90]. Other existing methods suppress undersampling artifacts using temporal regularization [91], predictive filtering [76, 92], and phase-constrained compressed sensing [93]. With temporal regularization approaches, there is a trade-off between reducing image artifacts and maintaining temporal resolution.

This work presents developments in reconstruction methods for undersampled data that can be combined with multi-coil imaging when available. It would take 15 s to image from the abdomen to the spine, approximately 21 cm in depth [94], by adding slices to the existing thermometry protocol (illustrated in Fig 1.3). A factor of 5$\times$ acceleration is necessary to maintain temporal resolution for updating temperature maps. Acquiring isotropic $2.5\times2.5\times2.5$ mm^3 spatial resolution of this volume in 3 s would require 14$\times$ acceleration, or 42 s without acceleration. Increasing scan coverage during brain MRgFUS from 3 mm to 9 cm by stacking images would lengthen scan time to 150 s per volume (30$\times$). Volumetric imaging, either through 3D sequences or multislice scans, would provide continuous monitoring needed for more efficient, parallelized MRgFUS targeting such as multi-focus sonications. Increased spatial coverage is also a requirement for the evaluation of potential new treatment options, such as expanded treatment envelopes for transcranial MRgFUS [46].

In addition to enabling greater spatial coverage, accelerated imaging would permit finer spatial sampling during the same time frame. Spatial resolution should be high enough to resolve both the anatomical features of interest and the focal heating region, and current goals are 1-2 mm in practice [75, 76]. Improved spatial resolution will enable targeting of smaller, more diffuse lesions in addition to the large, distinct tumors that are currently treatable.

1.2.3 Heat-induced artifacts in images and temperature maps

In practice, most MRgFUS procedures rely on proton resonance frequency (PRF) shift-based thermometry. Protons precess at a characteristic resonance frequency when their alignment with the main magnetic field of the MRI scanner is disrupted (i.e., by a radiofrequency pulse). This resonance frequency is directly proportional to the strength of the magnetic field [95]. Hydrogen bonds stretch as temperature increases, resulting in higher electron shielding of protons from the main magnetic field. Effectively, this reduces the field strength observed by the protons and, consequently, their resonance frequency [96]. The PRF shift varies approximately linearly with temperature [97] for most aqueous tissues, with a chemical shift coefficient of 0.01 ppm/°C over temperatures of 20-80°C [98]. The change in PRF is measured via the phase difference between images collected during heating and reference images taken at a baseline temperature. PRF shift temperature measurements have been reported with better than +/-1°C accuracy with 3°C temperature rise in brain [96] and +/-1.6°C over 20-50°C temperature change in muscle [99]. Since a 1°C increment corresponds to a relatively small chemical shift of 0.01 ppm, measurements based on the PRF shift are sensitive to other sources of field fluctuations [99].

An existing challenge affecting the accuracy of PRF-based measurements is heat-induced distortion [11]. The temperature rise induces susceptibility changes in tissue, which lead to errors in temperature measurements, as well as image magnitude artifacts [100]. Corrections for temperature-induced variations in bulk magnetization susceptibility have been proposed [101, 102, 103]. Additionally, it is necessary to correct image distortions that arise from the heating itself in order to reconstruct maps accurately. The shift of frequency with temperature causes an error in the spatial encoding of the signal. That is, the image pixels are shifted in the images and temperature maps because of the frequency offset. The appearance of the hotspot distortion depends on the MRI signal sampling trajectory that is used. The artifact manifests as a pixel shift in 2DFT and EPI readouts, and creates a blurring artifact in spiral readouts. Multi-shot acquisition schemes can reduce these er-

rors to some degree, but do not eliminate them entirely [104, 105]. Errors in thermometry translate to errors in thermal dose calculations, which are used to model heat deposition and thresholds for tissue coagulation. Therefore, accurate measurements are critical for effective treatment administration [75].

1.3 Innovation

The goal of this work is to improve temperature measurement accuracy and temporal resolution in MR thermometry. We will reconstruct temperature maps by fitting a constrained model to undersampled k-space data, without reconstructing a full complex image at each dynamic. By reconstructing temperature maps directly from k-space, heat-induced chemical shift distortions and undersampling aliasing artifacts can be removed as part of the reconstruction process. The proposed method will correct for artifacts from both chemical shift effects and data undersampling, without compromising temporal resolution, to produce accurate, accelerated temperature maps.

Temperature changes are reconstructed by fitting a hybrid multibaseline and referenceless image model directly to k-space data [106]. This temperature model has been shown to produce robust measurements, especially in the presence of tissue motion [106, 82]. The multibaseline approach combines multiple baseline or reference images to form a library of the anatomy prior to heating. The referenceless component fits a smooth phase shift term as a combination of polynomials. We constrain the magnitude of the reconstructed image based on the fully-sampled baseline images, model the background phase changes and heat-induced magnitude image attenuation, and solve for the heat-induced phase shift. The model components are illustrated in Fig 1.4. Aliasing artifacts from undersampling are suppressed by incorporating fully-sampled baseline images in the model. Temperature maps are reconstructed without temporal smoothing that causes a loss of temporal resolution. Additionally, off-resonance phase accrual originating from the PRF shift with heat can be incorporated in the k-space model to reconstruct temperature maps free from

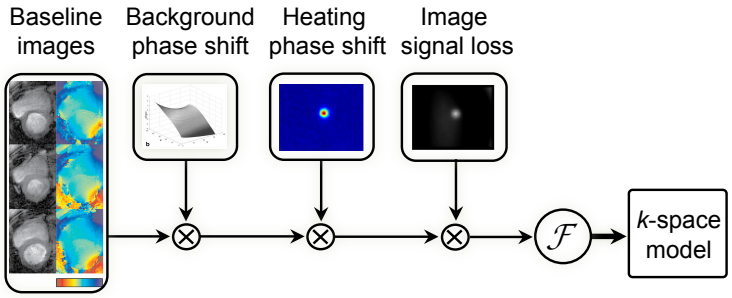

Figure 1.4: Illustration of temperature model. The image with heat is modeled by a linear combination of fully-sampled complex baseline images, a background polynomial phase shift to capture slowly-varying changes such as those caused by scanner drift, a focal heat-induced phase shift, and accompanying heat-induced image magnitude attentuation. A Fourier Transform is used to obtain the k-space signal model.

heat-induced distortions.

We present a novel, spatially-segmented approach for reconstructing temperature maps from undersampled brain MRgFUS data to avoid aliasing artifacts caused by water bath motion. Circulating water in the bath between sonications creates unpredictable signal changes in dynamic images that are not captured by baseline images. These dynamic signal variations cause errors in temperature maps reconstructed by model-based methods when they are not accounted for. To overcome errors arising from the water bath signal, we fit the developed k-space temperature model to the brain image only and reconstruct a model-free image in the water bath.

Chapter 2

MRI thermometry

2.0.1 Introduction

Reliable temperature mapping is critical for measuring tissue heating during thermal therapies. High temperature elevations can be applied in short bursts, or small heat changes can be induced over sustained periods depending on the type of treatment [71].

Some invasive procedures use a thermometer embedded in a surgical needle to record temperature. However, this only provides a measurement at a spatial location close to the probe, and does not give a complete picture of temperature change across the tissue. The invasive nature of this type of measurement can also cause concern or complication. In the case of ultrasound procedures, the needle may interfere with the treatment [11].

Ultrasound can be used to determine changes in temperature through speed of sound, attenuation coefficient, and backscattered energy measurements. Ultrasound is affordable, safe, and portable, which provides practical advantages. Although temperature imaging is not available during clinical treatment, echo changes are used to infer tissue effects for guiding thermal therapies such as high intensity focused ultrasound for tumor ablation [107, 108]. Still, the current sensitivity is generally not optimal for monitoring tissue heating during treatment procedures [109, 110]. Ultrasound attenuation varies with temperature and rate of thermal delivery, and increases in lesioned tissue [111, 60]. The speed of sound changes nonlinearly with temperature in the range used for therapy, has varying sensitivity with temperature, and is affected by thermal expansion in tissue [112, 113, 109, 114]. Thermal lesions induced by focused ultrasound can be visualized using B-mode imaging only if gas bubbles are present, and other imaging techniques are required to validate treatment outcomes [115].

MRI allows noninvasive temperature measurement and concurrent visualization of tis-

sue during heating procedures. With high spatial resolution and excellent soft tissue contrast, it can be used both for temperature mapping and localization of anatomic structure for planning and monitoring. Post-treatment evaluation using contrast-enhanced imaging provides feedback on therapeutic effects in tissue.

2.0.2 Imaging principles, in brief

2.0.2.1 Ultrasound

Piezoelectric crystals convert voltage that is used to drive the transducer into pressure waves, which propagate into the body with adequate coupling by gel, for example. The impedance between the transducer and body must be sufficiently matched to permit transmission of the high frequency pressure waves. Without matching, pressure waves will be reflected at the interface between the two media. In ultrasound imaging, partial reflections at boundaries are detected by the transducer and used to determine boundary position based on the time delay of the received signal and the speed of sound of the traveling wave in the body. Variations in speed of sound between tissues cause angular changes in the propagating wave at tissue boundaries [116].

Pressure waves traveling through tissue cause mechanical motion, and friction between tissue layers can lead to heat absorption. Thermal absorption is proportional to the acoustic intensity of the wave. Operating at low intensities, diagnostic ultrasound produces negligible heating effects. In high intensity focused ultrasound treatments, coagulative necrosis in tissue can be induced in only a few seconds [108].

2.0.2.2 Magnetic resonance imaging

In the presence of strong magnetic fields, protons in the body align with the main field and can be in spin-up or spin-down states. The small difference between energy in spin-up and spin-down states gives rise to detectable signal as the protons transition between states. Radiofrequency (RF) pulses tuned to the Larmor frequency, given by the product

of the proton gyromagnetic ratio and the field strength, temporarily disrupt this alignment and impart energy to protons as they are displaced from their equilibrium state. Protons disrupted from the longitudinal axis (along the main field) precess at the Larmor frequency about this axis. A vector component of the net magnetization of these spins lies in the transverse plane, and decays as protons return to equilibrium. The precessional motion generates an electromotive force in nearby coils as the magnetization vector moves through the plane. The RF pulse strength, timing, and time-varying magnetic fields give rise to different mechanisms of imaging contrast in tissues with different properties [117].

2.0.3 MRI metrics for measuring temperature change

Several MR parameters have been used to determine temperature change in tissue. The longitudinal relaxation time (T_1), the diffusion coefficient (D), and the proton resonance frequency (PRF) shift are three commonly used metrics.

2.0.3.1 Longitudinal relaxation time

The longitudinal relaxation time (T_1) increases with temperature, and is proportional the quantity $e^{-E_a(T_1)/\kappa T}$, where $E_a(T_1)$ is the activation energy of the relaxation process, κ is the Boltzmann constant, and T is absolute temperature. Over the typical temperature range of interest, the longitudinal relaxation time of tissue changes linearly with temperature. The T_1 of tissue after heating or cooling can be computed from the T_1 at some reference temperature T_{ref} plus the temperature difference scaled by the rate of change of T_1 with respect to temperature: $T_1(T) = T_1(T_{ref}) + \frac{dT_1}{dT}(T - T_{ref})$ [71].

The longitudinal relaxation time is a measure of how quickly protons return to equilibrium after their alignment with the main magnetic field has been perturbed. This process results primarily from interactions between protons and the surrounding environment [118, 119]. As a result, T_1 relaxation and its temperature dependence vary across tissues of different composition. Furthermore, T_1 also varies as tissue structure is altered, e.g., in the

case of coagulation [11]. The change in T_1 with temperature has been shown to be linear over a 30-40°C range [118, 120, 121], but has been noted to be nonlinear when coagulation occurs [11]. Animal studies have reported correspondence of a 1°C change to a T_1 change of 1.4% in muscle [120], 1-2% in liver [122], and 0.97% and 1.27% in fat depending on the acoustic power [121].

The tissue-dependence of both the longitudinal relaxation time and its variation with temperature are important considerations when using this method for thermometry. The tissue composition within a voxel also impacts temperature maps, because relaxation properties differ between lipid and water protons. An inhomogeneous tissue profile can lead to artifacts in the calculated temperature values. Additionally, the temperature-dependent change in the proton resonance frequency causes dephasing and reduced signal. To reduce this effect, gradient echo sequences with short echo times can be used. Spin echo sequences are preferable to refocus effects from PRF shift spin dephasing, but generally lead to increase in scan time relative to gradient echo acquisitions.

2.0.3.2 Diffusion coefficient

The diffusion coefficient is a function of temperature, and is proportional to the quantity $e^{-E_a(D)/\kappa \mathrm{T}}$, where $E_a(D)$ is the activation energy of the molecular diffusion of water, κ is the Boltzmann constant, and T is absolute temperature. Diffusion changes about 2%/°C, and can be used to determine temperature change using the relation $\Delta T = T - T_{ref} = (\kappa T_{ref}^2 / E_a(D))(D - D_{ref})/D_{ref}$, where D and D_{ref} are the respective diffusion coefficients at temperatures T and T_{ref}.

Reconstruction of temperature changes based on the diffusion coefficient requires additional computational cost and acquisition time. The mobility of water molecules is constrained by tissue architecture and is anisotropic. Because of the directional nature of the diffusion, tensor estimation is typically used to determine the diffusion coefficient. This requires several diffusion-weighted acquisitions to adequately characterize the motion of

water across different directions.

The movement of water molecules in tissue is dependent on factors such as membrane permeability, which change nonlinearly with temperature. The diffusion process therefore is not directly proportional to temperature variation. This property makes calculation of temperature change from diffusion measurements less straightforward. Another complication arises from the increased motion sensitivity in diffusion-weighted imaging that results from long acquisition times. At high temperature, increased diffusion may be difficult to detect if water motion is also restricted by structural changes such as tissue coagulation.

Fat has a low diffusion coefficient, and has a different change in diffusion coefficient with temperature as compared to water. This can cause measurement errors in imaging samples that are composed of a mixture of water and fat components. The shift in proton resonance frequency as a function of temperature is a source of signal loss and can be confounded with diffusion-based signal change. Spin echo sequences can be used to rephase these effects, and are therefore preferred over gradient echo sequences for this application [71].

2.0.3.3 PRF shift

As temperature increases, hydrogen bonds shared between water molecules weaken. Consequently, the amount of proton shielding by electrons increases. The resonance frequency of a proton is the product of the proton gyromagnetic ratio γ and the magnetic field strength B: $\omega = \gamma B$. The net field observed by a proton is equal to the main magnetic field adjusted for local field inhomogeneity, $\Delta B_0(T)$. This local inhomogeneity results from nonuniformity of the main field, δB_0, and the temperature-dependent chemical shift field, $B_c(T)$, induced by the magnetic shielding effects: $\Delta B_0(T) = \delta B_0 + B_c(T)$ [96].

The PRF shift varies approximately linearly with temperature, with a scaling coefficient α of -0.01 ppm/°C for most aqueous tissues [97, 98]. The chemical shift can be described by intrinsic and temperature-dependent factors as $\sigma(T) = \sigma_0 + \sigma_T(T)$, and contributes to

the image phase as $\theta(T) = \gamma\sigma(T)T_E B_0$, where T_E is the echo time, and B_0 is the main field strength. A phase difference image can be obtained from signal acquired at a reference temperature T_{ref} and another temperature T. In the absence of other introduced phase changes, the phase difference is only sensitive to the temperature-induced change. Local field inhomogeneity effects from B_0 nonuniformity are removed by the subtraction of the reference data. The temperature change can be measured from the change in image phase as $\Delta T = \Delta\theta/(\gamma B_0 \alpha T_E) = (\theta(T) - \theta(T_{ref}))/(\gamma B_0 \alpha T_E)$.

The approximately constant sensitivity over aqueous tissue can provide a uniform measurement of temperature change across a range of non-adipose tissue. In water, changes of hydrogen bond properties with temperature lead to the observed PRF shift. However, because adipose tissue has little hydrogen bonding, the resonance frequency of lipid protons has small variation with temperature. This affects the measured phase difference and causes errors in tissue containing both water and fat. MR-derived temperature measurements agree with thermometer readings in homogenous tissue. However, with heterogenous compositions containing muscle, fat, and connective tissue, MR thermometry estimates deviate from the actual temperature value as heating is applied. Suppression of lipids is therefore important for obtaining reliable results, especially in tissues with nonuniform composition [99].

Because chemical shift effects induced by temperature would be refocused by spin echo sequences, gradient echo sequences are used for measurement of the PRF shift. RF spoiling is also incorporated to reduce stimulated echo effects [11].

2.0.4 Heating and monitoring in adipose tissue

PRF thermometry provides good measurements for aqueous tissue, but cannot be used to determine temperature changes in adipose tissue because of the lack of hydrogen bonding. Instead, changes in the T_1 relaxation time have been used to infer changes in temperature in adipose tissue [121].

Though lipid heating is not measurable by the PRF shift, it induces changes in magnetic susceptibility in the tissue. This leads to errors and a decrease in the temperature measurement accuracy of aqueous tissue [101, 84, 99, 26]. As a result, most thermometry protocols use selective excitation or saturation techniques to suppress signal from lipids in the tissue. Although this reduces measurement error, it ignores the change in temperature within adipose tissue. Algorithms incorporating fat image signal to improve thermometry measures have been developed which allow for mixed water and fat composition within a voxel [123, 124, 125]. Hybrid PRF and T_1 measurement techniques for simultaneous water and fat temperature monitoring are also an area of active research [126, 74, 127]. As noted earlier, neglecting to monitor treatment effects increases the concern that injuries can arise and worsen, undetected. Therefore, care must be taken to ensure patient safety during MRgFUS interventions.

2.0.5 PRF-shift thermometry methods

With a gradient echo sequence, the PRF temperature shift can be measured by a phase difference of complex images aquired before and during heating [96]. The optimal phase difference is obtained when the echo time is close to the T_2^* relaxation time of the tissue, the repetition time is relatively long, and the flip angle is equal to the Ernst angle [83]. This phase difference is calculated from the phase of an image formed by multiplying one image by the complex conjugate of another image acquired at a different temperature. The corresponding change in temperature can then be determined directly from the phase difference image by applying a scaling factor [96, 128, 83]. This is the complex phase difference or baseline subtraction estimate of the temperature change.

Multibaseline thermometry is more robust to motion changes than single baseline subtraction, as it incorporates a series of baseline images sampled at different positions within a physiological cycle rather than relying on one pre-treatment image alone. Based on the tissue position at the time of heating, a baseline image acquired at a similar position can

be selected in oirder to compute the PRF shift. Since the baseline images cover a range of tissue motion, they can also be combined to form a composite image to more closely match the position of the treatment image [129].

Referenceless thermometry, in contrast, does not rely on pre-treatment baseline images to estimate the PRF shift. Instead, the background phase is estimated from each treatment image in a region away from heating, which avoids errors from mismatched tissue position between baseline and treatment images. A polynomial fit is used after phase unwrapping to capture the background phase variations, and incorporates pixel-wise weighting based on the standard deviation in the image. However, the polynomial fitting approach may be limited in regions where there are complex phase changes, such as near interfaces between different tissues. The method also cannot distinguish between heating and non-heating-related phase changes [130].

Hybrid multibaseline and referenceless thermometry methods combine the two approaches, producing temperature estimates with lower error than either method on its own [131, 106, 82]. While multibaseline thermometry has an advantage over referenceless methods in areas with highly variable phase changes, it does not estimate a background phase drift that can occur over the course of scanning. Referenceless thermometry is not inherently limited by tissue position and is more adaptable to spontaneous motion. However, referenceless temperature estimates depend on selection of the heating region within the image, and its proximity to other areas of phase variation [131]. The use of high-order polynomial fitting to characterize background phase in heterogenous tissue also increases the risk of lowered sensitivity to phase shifts caused by heating. Combining multibaseline and referenceless approaches results in temperature estimates more robust to both motion changes during treatment and inherent phase variations in the body [106].

2.0.6 Accelerated imaging techniques for PRF-shift thermometry

The goal of accerated temperature imaging for MRgFUS monitoring is to increase spatial coverage during scans without suffering a loss in temporal resolution. In addition to ensuring sufficient monitoring of tissue heating during therapy, high temporal resolution is desirable for reducing motion-related artifacts. Fast acquisition strategies such as echo-planar imaging (EPI), echo-shifting, and combinations such as multi-shot echo-shifted EPI are useful for accelerating scan time [132, 133, 59, 134]. Spiral sampling can also be used to reduce acquisition time and, because the center of k-space is sampled during each spiral acquisition, can be used for navigator-based corrections [135, 136, 137, 138].

To further decrease scan time, partial datasets can be collected and combined with previously acquired, fully-sampled data. Using a keyhole approach, missing data is substituted with corresponding samples from the baseline image, which improves image reconstruction compared to assigning a value of zero to unsampled data points [139]. A reduced-encoding imaging by generalized-series reconstruction (RIGR) approach builds on a fully-sampled baseline image by updating partial segments of k-space at each time point, which may impose a signal-to-noise ratio penalty but preserves in-plane spatial resolution in reconstructed images [140, 141]. At high acceleration factors, added image reconstruction constraints are required to suppress artifacts.

In addition to pulse sequence modifications, MR thermometry can be accelerated through a combination of acquiring undersampled data and reconstructing images by methods that correct artifacts caused by undersampling. Parallel imaging methods can be leveraged where multiple receive coils are available [85]. However the acceleration factor they can achieve depends on having many coils placed in close proximity with the body, which is often limited by the focused ultrasound transducer. Compressed sensing methods exploit sparsity in the magnitude images to suppress aliasing artifacts [86, 87, 142], which can lead to errors if phase variations due to heating are not captured. Methods incorporating phase change have been proposed in a highly-regularized referenceless context and with diffuse

radiofrequency heating [143, 93].

Filtering-based methods use prior temperature changes to inform reconstructions at each time point. Alternating k-space sampling between dynamics creates varying artifact patterns that can be filtered out. However, the inter-image regularization inherently introduces blurring of temperature changes in the time domain. Temporally-constrained reconstruction (TCR), which relies on temporal smoothing to suppress artifacts, can be combined with EPI subsampling strategies [144, 145]. Model-based filtering methods require good characterization of temperature evolution to constrain reconstructions at each dynamic, such as the Pennes bioheat equation [76, 92]. Imperfections in the model can introduce a source of error, or cause true temperature changes from unexpected heating patterns to be removed as artifacts. Selective excitation and reduced field of view imaging have been combined with temporal filtering and parallel imaging can improve temporal resolution within a pre-defined subset of image space, but do not monitor temperature changes across the entire image plane [79].

2.0.7 Summary

Invasive temperature measurements are not always practical or sufficient for use in thermal therapy procedures. MRI can be used to noninvasively determine temperature change in tissue, and several methods have been developed. T_1 relaxation time and diffusion coefficient measurements are sensitive to the specific tissue environment of water protons. Additionally, tissue coagulation in thermal ablation and microstructural changes in the tissue that may result from heating procedures will directly impact T_1 and diffusion coefficient properties. The proton resonance frequency shift is widely used as a metric for calculation of temperature. The change in temperature is linearly proportional to the change in phase in a gradient echo image. By subtracting the temperature-invariant component of this shift, the temperature-specific change can be isolated. The PRF shift approach has nearly constant sensitivity for water proton measurements. However, lipid protons have substantially

different properties and do not exhibit the same degree of variation in the presence of temperature change. In each of the MR temperature mapping methods mentioned above, lipid suppression through the use of saturation pulses or selective excitation is incorporated to reduce measurement error.

Use of the PRF shift for thermometry requires gradient echo imaging sequences for measurement of phase changes induced by temperature-dependent chemical shift. In order to avoid confounds from the PRF shift in T_1 and diffusion coefficient methods for mapping temperature, spin echo sequences are employed in these cases to rephase the chemical shift. The PRF shift approach to temperature mapping can be faster that T_1 and diffusion coefficient approaches because of this difference in pulse sequences. Fast imaging methods and accelerated reconstruction techniques are often used to image temperature changes in real-time during thermal treatments.

Chapter 3

Accelerated MRI thermometry by direct estimation of temperature from undersampled k-space data

3.1 Abstract

Purpose: Acceleration of MR thermometry is desirable for several applications of MR-guided focused ultrasound, such as those requiring greater volume coverage, higher spatial resolution, or higher frame rates.

Theory and Methods: We propose and validate a constrained reconstruction method that estimates focal temperature changes directly from k-space without spatial or temporal regularization. A model comprising fully-sampled baseline images is fit to undersampled k-space data, which removes aliased temperature maps from the solution space. Reconstructed temperature maps are compared to maps reconstructed using parallel imaging (SPIRiT) and conventional hybrid thermometry, and temporally-constrained reconstruction (TCR) thermometry.

Results: Temporal step response simulations demonstrate finer temporal resolution and lower error in $4\times$-undersampled radial k-space reconstructions compared to TCR. Simulations show that the k-space method can achieve higher accelerations with multiple receive coils. Phantom heating experiments further demonstrate the algorithm's advantage over reconstructions relying on parallel imaging alone to overcome undersampling artifacts. In vivo model error comparisons show the algorithm achieves low temperature error at higher acceleration factors (up to $32\times$ with a radial trajectory) than compared reconstructions.

Conclusion: High acceleration factors can be achieved using the proposed temperature reconstruction algorithm, without sacrificing temporal resolution or accuracy.

3.2 Introduction

Recent technological developments have combined thermal therapies with MRI for targeting, temperature monitoring and assessment of thermal dose in the brain and body [12]. In particular, MRI-guided focused ultrasound (MRgFUS) is increasingly being applied to treat uterine fibroids and cancer [1, 2, 3, 4], relieve pain from bone metastases [5, 6], and stimulate deep brain tissue to treat neurological conditions [7, 44]. Additionally, animal studies have demonstrated that MRgFUS can induce gene expression [9] and also facilitate drug delivery [146], even across the blood-brain barrier [147, 148].

In MRgFUS, ultrasound energy is generated outside the body and delivered noninvasively to a specific location within the tissue, ideally without affecting any tissues outside the targeted volume. The primary role of MRI in the procedures is to provide images with soft tissue contrast for targeting, and to provide real-time temperature measurements to monitor thermal dose to the targeted tissue, where temperature measurements are conventionally based on the proton resonance frequency shift with temperature. While acoustic energy is nominally focused to a single point in the body, there is an ever-present risk that dangerous heating may occur in other regions in the near- and far-fields of the transducer, so it is desirable to measure temperature rises with as high a frame rate as possible throughout the tissue to ensure patient safety. However, MRgFUS procedures are currently limited to 2D temperature imaging of a handful of slices in real-time. For example, typical thermometry protocols for closed-loop ablation of uterine fibroids use spoiled gradient echo or multishot echo-planar imaging (EPI) to image up to six slices [59, 72] approximately every three seconds. However, due to their limited volume coverage those scans can miss dangerous heating that can occur outside the target volume, particularly near tissue interfaces and bones [20]. Some form of scan acceleration is required to simultaneously achieve large volume coverage and a high frame rate in thermometry, using either pulse sequences that acquire k-space data faster [149] or temperature reconstructions that do not require full k-space data.

Temperature reconstruction-based approaches to accelerating MR thermometry can be loosely grouped into three categories: parallel imaging, compressed sensing, and temporal regularization-based approaches. Parallel imaging with multiple receive coils is commonly used to accelerate anatomical and functional MR imaging [85, 150], and has been applied to thermometry [151, 152, 153, 154, 79]. However, to achieve high accelerations, parallel imaging requires many coils in close proximity with the body, which is often impossible in MRgFUS since the FUS apparatus is large and must be in direct contact with the body. Because of these limitations, the development of MRgFUS-compatible coil arrays is an active area of research, and state-of-the-art arrays still comprise many fewer coils than are typically used in conventional parallel imaging [88, 89, 90].

Compressed sensing [86] has also been applied to MR thermometry [87, 142]. However, these techniques rely on compressibility of image magnitude to constrain the solution space, and errors can arise when the phase component of the image contains high spatial frequency variations such as those caused by heating [143]. Furthermore, compressed sensing must typically be combined with parallel imaging to achieve high accelerations. Compressed sensing reconstructions that incorporate phase regularization have been proposed for thermometry [93, 143], but to date no such method has been described that robustly enables high acceleration factors in a wide variety of acquisition scenarios.

Temporal regularization-based approaches [91, 79, 76, 77] assume that images or temperature change slowly during treatment. For example, the temporally constrained reconstruction (TCR) method [91] jointly reconstructs treatment images using a temporal roughness penalty. This enables acceleration when the k-space undersampling pattern is alternated in time so that aliasing artifacts move between consecutive images and are filtered out by the penalty. Other temporal regularization-based approaches have leveraged the bioheat equation and/or Kalman filtering, either to similarly suppress rapidly-changing aliasing artifacts while preserving slower temperature changes, or to interpolate between fully-sampled temperature images acquired at a lower frame rate [76, 77]. While all these

approaches are capable of producing temperature maps at any desired frame rate, due to regularization their true temporal resolution lies somewhere between the accelerated and fully-sampled frame rates. Furthermore, the alternating k-space sampling patterns required by some methods may lead to increased eddy current distortions, and generally limit pulse sequence design.

This work introduces an approach to accelerated temperature imaging that is based on fitting a constrained treatment image model directly to undersampled k-space data. Because the treatment image model comprises fully-sampled pretreatment/baseline images, aliased temperature maps are removed from the solution space, without temporal regularization. The method is compatible with parallel imaging and can be used with any readout trajectory. Simulations will demonstrate improvements in temporal resolution compared to TCR, that the method is compatible with and benefits from multicoil receive, and that it is robust to motion and rapidly-varying background anatomical phase. Experiments will investigate in vivo model error as a function of acceleration, and compare the method to conventional parallel imaging reconstructions. Aspects of this work have been previously reported elsewhere [155, 156].

3.3 Theory

3.3.1 Signal Model and Problem Formulation

The proposed method estimates temperature maps from undersampled k-space data by fitting a constrained image model directly to the data, without an explicit image reconstruction step. The hybrid multibaseline and referenceless treatment image model is used [106], which comprises a weighted combination of fully-sampled baseline images acquired prior to heating, a polynomial phase shift to model center frequency drift and other bulk phase shifts unrelated to heating, and a spatially-sparse heating-induced phase shift. When applied to estimate temperature maps from fully-sampled images, hybrid thermometry has

been shown to produce accurate temperature measurements in the human brain and porcine liver with FUS heating [82, 157], and in the human heart and liver with motion [106].

The k-space signal model is the discrete Fourier transform (DFT) of the hybrid image model:

$$y_i = \sum_{j=1}^{N_s} e^{\imath \vec{k}_i \cdot \vec{x}_j} \left(\sum_{l=1}^{N_b} b_{l,j} w_l \right) e^{\imath \left(\{\boldsymbol{A}\boldsymbol{c}\}_j + \theta_j \right)} + \varepsilon_i, \tag{3.1}$$

where y_i is one k-space data sample, $i = 1, \ldots, N_k$ indexes the N_k acquired samples, N_s is the number of image voxels, $\vec{k}_i$ is the k-space location of sample i, the $\{\boldsymbol{b}_l\}_{l=1}^{N_b}$ are complex baseline library images reconstructed from fully-sampled k-space data acquired prior to treatment, the w_l are baseline image weights, $\boldsymbol{A}$ is a matrix of smooth (e.g., low-order polynomial) basis functions, $\boldsymbol{c}$ is a polynomial coefficient vector, $\boldsymbol{\theta}$ is a heating-induced phase shift, which is negative for a temperature increase [71] and is assumed to contain mostly zero entries, and ε is complex Gaussian noise. The role of the baseline library images $\{\boldsymbol{b}_l\}_{l=1}^{N_b}$ is to capture physiological and anatomical amplitude and phase variations across respiratory and cardiac cycles. The role of the polynomial phase shift $\boldsymbol{A}\boldsymbol{c}$ is to model phase changes induced by smooth magnetic field shifts, such as center frequency drift and those caused by respiration and bowel filling. The phase shift $\boldsymbol{\theta}$ that results from targeted heating is modeled as a focal shift separate from these other phase components. Sparsity of $\boldsymbol{\theta}$ is exploited by the algorithm to separate it from the polynomial phase shift, and reflects the fact that in a targeted thermal therapy like MRgFUS, temperature rises will occur in a minority of image voxels. To estimate $\boldsymbol{\theta}$, the signal model in Eq. 5.1 is fit to acquired k-space data $\tilde{\boldsymbol{y}}$ by solving the constrained minimization problem:

$$\begin{aligned} \text{minimize} \quad & \tfrac{1}{2} \left\| \tilde{\boldsymbol{y}} - \boldsymbol{y}(\boldsymbol{w}, \boldsymbol{c}, \boldsymbol{\theta}) \right\|^2 + \lambda \left\| \boldsymbol{\theta} \right\|_1, \\ \text{subject to} \quad & \boldsymbol{\theta} \preceq 0 \\ & \textstyle\sum_{l=1}^{N_b} w_l = 1 \\ & \boldsymbol{w} \succeq 0, \end{aligned} \tag{3.2}$$

where the first term in the objective function is proportional to the negative log-likelihood of the data (when neglecting noise in the baseline images), $\|\boldsymbol{\theta}\|_1$ is the ℓ_1 norm of $\boldsymbol{\theta}$, and λ is a regularization parameter that controls the sparsity of $\boldsymbol{\theta}$.

This method can reconstruct artifact-free temperature maps from undersampled k-space data because the fully-sampled baseline image component of the model removes images (and corresponding temperature maps) from the solution space that contain aliasing artifacts in their magnitude. Solutions containing aliasing artifacts in their phase that cannot be modeled by some combination of the baseline images, a polynomial phase shift and a sparse phase shift are also eliminated from the solution space.

3.3.2 Algorithm

A solution to the problem in Eq. 3.2 is found using the following alternating minimization algorithm, given initial estimates of $\boldsymbol{w}$, $\boldsymbol{c}$, and $\boldsymbol{\theta}$:

1: **repeat**

2: Update $\boldsymbol{w}$: A quadratic programming problem,

$$\begin{array}{ll} \text{minimize} & \frac{1}{2}\left\|\tilde{\boldsymbol{y}} - \boldsymbol{G}\text{diag}\left\{e^{\imath\left(\{\boldsymbol{A}\boldsymbol{c}\}_j + \theta_j\right)}\right\}\boldsymbol{B}\boldsymbol{w}\right\|^2 \\ \text{subject to} & \sum_{l=1}^{N_b} w_l = 1 \\ & \boldsymbol{w} \succeq 0, \end{array} \tag{3.3}$$

is solved, where $\boldsymbol{G}$ is a (possibly non-uniform) DFT matrix, and $\boldsymbol{B}$ is a matrix whose columns are the baseline images.

3: Update $\boldsymbol{\theta}$: The following constrained minimization problem is solved using the nonlinear conjugate gradient (NLCG) algorithm described in the Appendix (J A Fessler, *Image reconstruction: Algorithms and Analysis*, to be published.):

$$\begin{array}{ll} \text{minimize} & \frac{1}{2}\left\|\tilde{\boldsymbol{y}} - \boldsymbol{G}\text{diag}\left\{e^{\imath\theta_j}\right\}\boldsymbol{f}\right\|^2 - \lambda\sum_{j=1}^{N_s}\theta_j \\ \text{subject to} & \boldsymbol{\theta} \preceq 0, \end{array} \tag{3.4}$$

where $f_j \triangleq e^{\imath\{\boldsymbol{A}\boldsymbol{c}\}_j}\{\boldsymbol{B}\boldsymbol{w}\}_j$.

4: Update $\boldsymbol{c}$: The update for $\boldsymbol{c}$ is similar to the $\boldsymbol{\theta}$ update, except that the gradient, and consequently the NLCG search direction, incorporate the basis matrix $\boldsymbol{A}$,

$$\nabla_{\boldsymbol{c}}\Psi = \boldsymbol{A}'\nabla_{\boldsymbol{\theta}}\Psi, \tag{3.5}$$

and there are no nonpositivity constraints.

5: **until** Stopping criterion met

6: To eliminate temperature bias due to the ℓ_1 norm, steps 1-5 are repeated with $\lambda = 0$, and $\boldsymbol{\theta}$ is only updated in voxel locations that were more negative than a threshold value after Step 5.

3.3.3 Parallel Imaging

When imaging with more than one receive coil, $(\boldsymbol{w}, \boldsymbol{c}, \boldsymbol{\theta})$ are simultaneously fit to all coils' data. Because the baseline images are weighted by the coil sensitivities, the algorithm implicitly performs a SENSE reconstruction [85, 158], without requiring a separate sensitivity map measurement. It will be demonstrated in simulations that the algorithm is able to exploit multiple receive coils to improve temperature map accuracy at higher accelerations, compared to a single receive coil.

3.4 Methods

3.4.1 Algorithm Implementation

The proposed algorithm was implemented in MATLAB R2013a (Mathworks, Natick, MA, USA) on a workstation with a 3.4 GHz E31270 Intel Xeon CPU (Intel Corporation, Santa Clara, CA, USA) and 16 GB of RAM[1]. The DFT matrix $\boldsymbol{G}$ was evaluated using non-

[1]Example MATLAB files for temperature reconstruction of phantom heating data using the algorithm are available at http://www.vuiis.vanderbilt.edu/~grissowa/.

uniform fast Fourier transforms [159]. Baseline images were reconstructed from fully-sampled k-space data using a conjugate gradient algorithm [160]. When more than one baseline image was used, the baseline image weights $\boldsymbol{w}$ were solved for using MATLAB's `quadprog` function. The polynomial phase coefficient vector $\boldsymbol{c}$ and temperature phase shift vector $\boldsymbol{\theta}$ were initialized to zeros. Updates for $\boldsymbol{c}$ and $\boldsymbol{\theta}$ used 5 iterations. Voxels where $\boldsymbol{\theta}$ was more negative than -0.01 radians were corrected for temperature bias due to the ℓ_1 norm as described in Step 6 of the algorithm. In this stage, $\boldsymbol{c}$ and $\boldsymbol{\theta}$ updates contained 5 and 10 iterations, respectively. The algorithm stopped when the relative change in the objective function was less than 0.1% between consecutive iterations.

In the following simulations and experiments, the k-space thermometry algorithm is compared with TCR [91] and temperature maps estimated after image reconstruction by either conjugate gradient (CG) or SPIRiT [161], using a hybrid thermometry image model. SPIRiT kernels were calibrated using the (fully-sampled) baseline image and reconstructions used a 5×5 kernel and a 30×30 calibration region, and the SPIRiT regularization parameter was set to the median of the absolute value of the k-space data. Given a reconstructed image $\boldsymbol{m}$ from CG or SPIRiT, temperature phase shifts were estimated as:

$$\theta_j = \angle(m_j f_j^*), \tag{3.6}$$

for each voxel j, where $\boldsymbol{f}$ is the baseline image with polynomial phase shift estimated by the k-space algorithm.

3.4.2 Temporal step response simulation

To investigate the temporal step response of reconstructed temperature maps and compare it to TCR, k-space data of a simulated circular phantom and an instantaneous on-off Gaussian-shaped (FWHM of 0.8 pixels) heat-induced phase shift were generated for a golden angle (GA) radial trajectory with FOV = 20 cm, matrix size = 64×64, TE = 16 ms,

and 101 radial lines for full sampling. The peak phase shift of 1.7 radians corresponded to 13°C heating at 3 T. The median absolute value of the k-space data was 4.37. Temperature change maps were reconstructed at 4× acceleration (25 lines, 91 samples per line) using TCR and the k-space method. TCR reconstructions used a weighting factor $\alpha = 100$ and 100 iterations. The k-space method used $\lambda = 10^{-4}$, one baseline image, and a zeroth-order polynomial fit.

3.4.3 Multicoil receive simulation

The same circular object and Gaussian-shaped phase shift were generated with the same settings as the temporal step response simulation for a single receive coil with uniform sensitivity, and for a simulated 8-channel 3 T receive coil array [162]. k-Space data were synthesized using GA radial and 2DFT readout trajectories. Temperature maps were reconstructed by the k-space method and by Eq. 3.6 from images reconstructed by SPIRiT from the 8-channel data. Reconstructions were performed across a range of acceleration factors, with 64 (2DFT) and 91 (GA radial) k-space samples per line. The k-space method again used $\lambda = 10^{-4}$, one baseline image, and a zeroth-order polynomial fit.

3.4.4 Motion simulation

A simulation was performed to validate the algorithm's robustness to motion and its ability to regress rapidly-varying background anatomical phase, in the same manner as was done in Ref. [106] for the image domain hybrid algorithm. 64×64 images of a rectangular object were generated with background phase comprising a weighted sum of low frequency Fourier components. A library of 50 baseline images were generated across a range of vertical organ positions, representative of motion that could be observed in the liver as part of a normal breathing cycle. 100 uniformly-distributed random positions within this range were chosen and used to synthesize treatment images with Gaussian-shaped phase shifts to simulate focal heating (peak magnitude corresponding to a 23°C heat rise at 3

T) and sixth-order random polynomial phase shifts. k-Space data were generated from the treatment images using an 8×-accelerated radial trajectory (12 lines, 91 samples per line) with one receive coil and FOV = 20 cm, matrix size = 64×64, and TE = 16 ms. The k-space temperature reconstruction algorithm was applied using the generated baseline library, a sixth-order polynomial fit, and $\lambda = 0.2$. A second order finite differencing spatial roughness penalty (with regularization parameter $\beta = 1$) was added to the $\boldsymbol{\theta}$ cost function following the method described in Ref. [163]. The median k-space data amplitude was 0.75.

3.4.5 Phantom heating experiments

To evaluate the method model experimentally, a tissue-mimicking gel phantom was sonicated using a Philips Sonalleve MR-HIFU system (Philips Healthcare, Vantaa, Finland) operated at 1.2 MHz and 100 Watts for 36 seconds, and targeting a 12 mm diameter treatment cell. The system was installed on a 3 T scanner (Philips Achieva, Philips Healthcare, Best, Netherlands). Gradient echo imaging was performed for temperature monitoring with 2DFT and GA radial readout trajectories and five receive coils. Parameters for the 2DFT and GA radial sequences were: FOV = 40 cm; matrix size = 192×192; slice thickness = 7 mm; TR = 32 ms; TE = 16 ms. The multicoil data were compressed to three coils by thresholding the singular values of the data matrix at five percent of the largest singular value. The median k-space data amplitude was 8.58 for 2DFT and 15.65 for GA radial scans. In addition to the k-space domain reconstructions, temperature maps were estimated using Eq. 3.6 and images reconstructed by CG and SPIRiT. Temperature maps were reconstructed to a 96×96 matrix with 20 cm FOV. Reconstructions used one baseline image, a zeroth-order polynomial fit, $\lambda = 0.016$ (2DFT) and 0.0075 (GA radial), and $\beta = 2^{-11}$ (2DFT) and 2^{-12} (GA radial). 2DFT reconstructions were performed after taking every fifth line of the original 192×192 matrix in either the x- or y-direction, corresponding to 2.5× acceleration relative to the 20 cm reconstructed FOV (39 lines; 96 samples per line

after averaging adjacent samples in the original matrix). GA radial data were undersampled by 16× relative to the 20 cm reconstructed FOV (9 lines; 192 samples per line).

3.4.6 In vivo model validation

To validate the k-space signal model in vivo in the absence of heat, sagittal brain images were collected in a healthy volunteer using an 8-channel receive array and GA radial readout trajectory at 3 T (Philips Achieva, Philips Healthcare, Best, Netherlands) under approval of the Institutional Review Board at Vanderbilt University with: FOV = 25.6 cm; matrix size = 128×128; slice thickness = 3 mm; TR = 100 ms; TE = 10 ms; 256 k-space samples per line. Multicoil data were compressed to four coils using singular value thresholding as in the phantom heating experiments. Temperature maps were estimated using k-space reconstructions and Eq. 3.6 with CG- and SPIRiT-reconstructed images. To evaluate temperature errors that could arise in the k-space reconstructions, the algorithm was executed without the $\boldsymbol{\theta}$ updates (Step 3 was skipped and $\boldsymbol{\theta}$ was fixed at 0) so that only the baseline image weights and background phase shift were estimated, using seven baseline images and a first order polynomial matrix. Then, keeping those baseline image and polynomial phase estimates fixed by skipping Steps 2 and 4, the algorithm was repeated to fit $\boldsymbol{\theta}$ with $\lambda = 0$. Temperature maps were reconstructed with no acceleration (256 lines; 97 maps), 2× acceleration (128 lines; 109 maps), 4× acceleration (64 lines; 116 maps), 8× acceleration (32 lines; 119 maps), 16× acceleration (16 lines; 121 maps), and 32× acceleration (8 lines; 121 maps). Errors were averaged over dynamic frames to determine the mean errors for each acceleration factor. The median k-space data amplitude was 85.04.

3.5 Results

3.5.1 Temporal step response simulation

The fully-sampled and undersampled k-space trajectories and corresponding magnitude image and baseline subtraction temperature map reconstructions of the simulated data are shown in Fig. 3.1a. Undersampling results in a noisy appearance of the magnitude image, and coherent streaking artifacts in the temperature maps. The temperature in the center voxel is plotted for the true and reconstructed maps in Fig. 3.1b. The k-space method better tracks the instantaneous temperature changes, achieving finer temporal resolution than TCR. Figure 3.1c shows temperature maps at 5 seconds, immediately after a transition. The k-space reconstruction has small truncation errors around the hot spot, but overall much lower error and no visible aliasing artifacts. With TCR, aliasing artifacts could be reduced by increasing temporal regularization, but this would further degrade temporal resolution.

3.5.2 Multicoil receive simulation

Multicoil receive simulation results are shown in Fig. 3.2. Root-mean-square error within the object, maximum error within the object excluding the temperature hotspot, and error in the center voxel of the reconstructed temperature maps were calculated for the 2DFT and GA radial reconstructions. The changing interference of coherent aliases at different acceleration factors results in oscillation in the 2DFT SPIRiT errors. Similar patterns are observed to a lesser degree in the single-coil k-space reconstructions at higher acceleration factors. However, the multicoil k-space reconstructions are free from these artifacts and produce temperature estimates with low error using as few as four readout lines, indicating that the accuracy of the k-space method's reconstructions improves with multiple receive coils. GA radial reconstructions using the k-space-based method do not exhibit significant aliasing artifacts in either single- or multi-coil cases. Error remains low for single-coil k-space estimates even when only two radial lines are used for tempera-

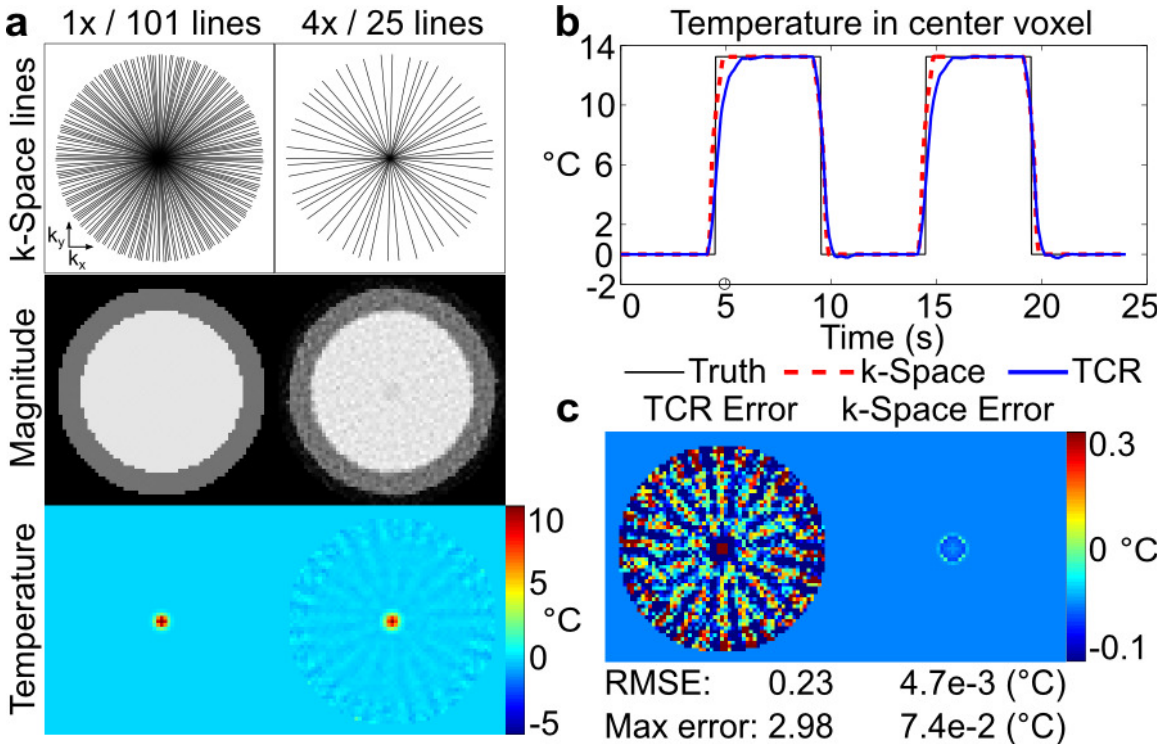

Figure 3.1: Temporal step response simulation. (a) Illustration of fully-sampled and 4×-undersampled radial trajectories and corresponding image and baseline subtraction temperature map reconstructions. Undersampling results in noisy-looking magnitude images and streaking in temperature maps. (b) Temperature in the center of the hot spot versus time. The proposed k-space-based reconstruction achieves finer temporal resolution than TCR since it does not depend on temporal regularization to suppress aliasing artifacts. (c) Just after the step temperature rise at 5 seconds (circle on x-axis in (b)), aliasing artifacts are visible in the TCR estimate, but not in the k-space method's estimate.

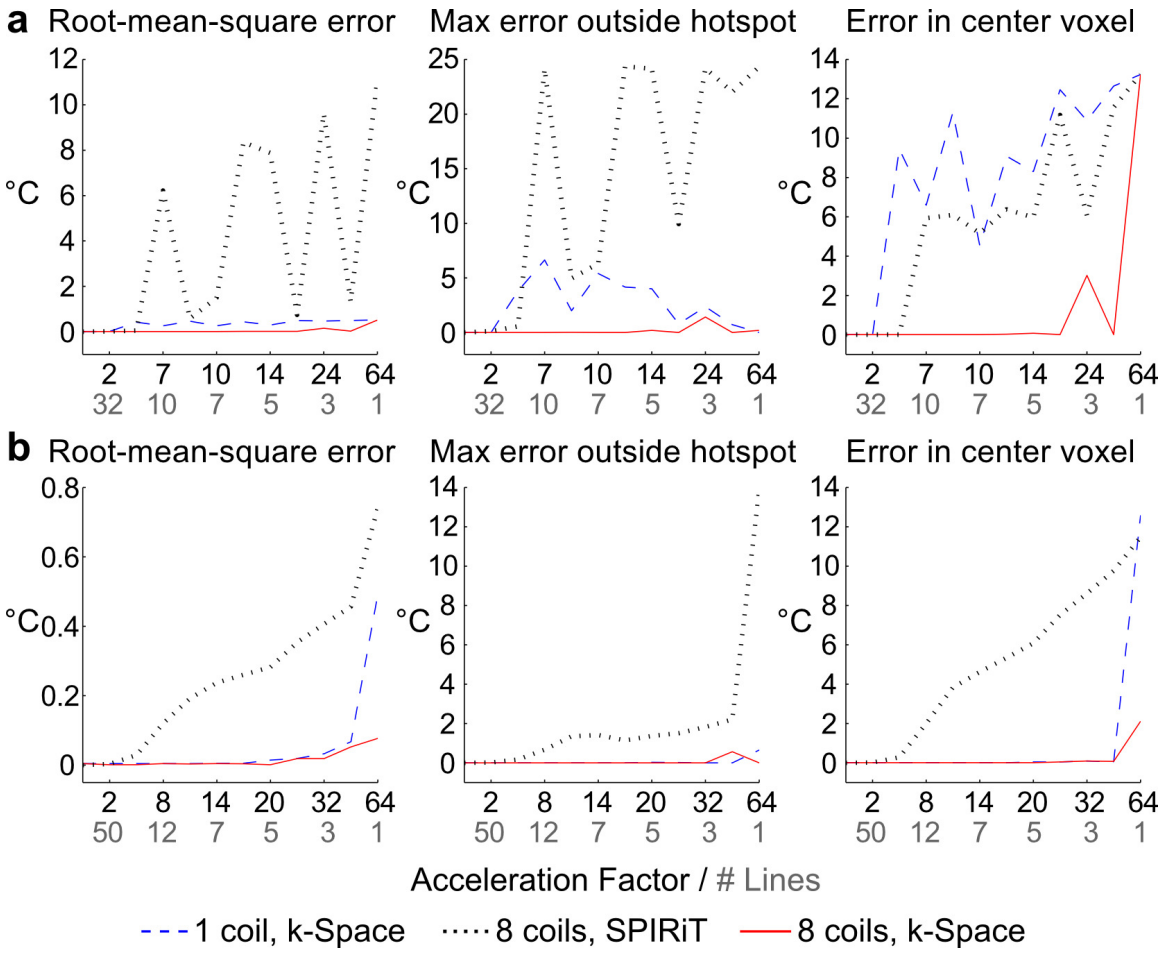

Figure 3.2: Multicoil receive simulation. Root-mean-square error, maximum error outside the hotspot, and error in the center voxel are plotted for (a) 2DFT and (b) GA radial trajectories. Black labels along the x-axis indicate acceleration factor, and gray labels indicate the corresponding number of readout lines used in the reconstruction. k-Space reconstruction errors are generally lower than SPIRiT errors, and multi-coil k-space estimates have lower error than single-coil estimates.

ture reconstruction. In contrast, the SPIRiT reconstructions are increasingly affected by undersampling artifacts with increasing acceleration factor.

3.5.3 Motion simulation

Results from one of the object positions are shown in Fig. 3.3. Figure 3.3f shows the residual phase after k-space thermometry, which was calculated by subtracting the fitted hybrid image model phase from the synthesized treatment image phase. No large resid-

ual phase errors are present within the object. The RMS and maximum temperature errors corresponding to the residual phase errors across all the random positions were 0.16 and 1.19 °C, respectively. The temperature maps were also accurately estimated (Figs. 3.3(g,h)). The RMS and maximum temperature map errors were 0.10 and 1.47 °C, respectively. These results indicate that the hybrid signal model was able to account for all sources of phase, and that the k-space thermometry algorithm was able to determine the parameters of that model.

3.5.4 Phantom heating experiments

Figure 3.4 shows the 2DFT phantom experiment results. Image-domain temperature reconstructions were highly sensitive to the relative orientation of the coil array (which encoded primarily along x) and the undersampled dimension, and aliasing artifacts in the images were lower when data was undersampled along the x-direction. Compared to the CG reconstruction, the SPIRiT algorithm was able to reduce but not fully remove artifacts from undersampling, likely due to the low number of receive channels (three, after coil compression) relative to the acceleration factor ($2.5\times$). The k-space temperature reconstructions were free from artifacts, regardless of the undersampled dimension. Figure 3.4c shows that the k-space temperature maps were free from artifacts over the entire course of the experiment, and closely matched the fully-sampled reconstructions. Temperature changes were overestimated in the SPIRiT temperature maps throughout the experiment.

Results from the GA radial scan are shown in Fig. 3.5. As in the 2DFT case, large aliasing artifacts are present in CG and SPIRiT reconstructions, but not in k-space-based reconstructions. At $16\times$ acceleration, SPIRiT-based temperature estimates are consistently lower than the heating estimated from fully-sampled data. The k-space temperature reconstruction algorithm produces heating estimates that closely match the fully-sampled results throughout the experiment.

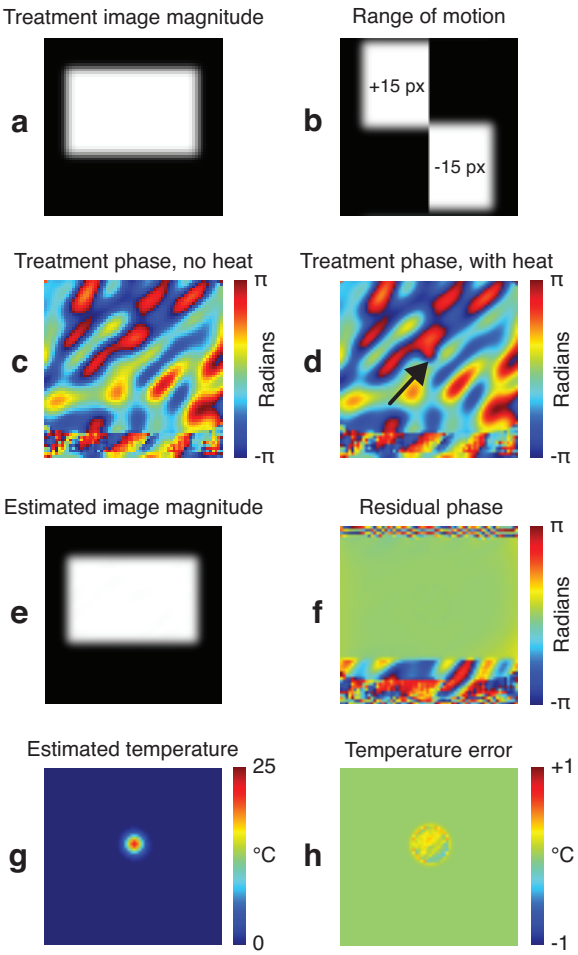

Figure 3.3: Motion simulation. (a) The treatment magnitude image, containing the moving rectangular object. (b) The first and last images in the baseline library, indicating the range of object motion. (c) A treatment image phase, with no heat present, contains polynomial and low frequency Fourier components. (d) The same phase in (c), with the Gaussian hot spot. (e) The estimated image magnitude, derived from the weighted baseline images. (f) Residual phase difference between the images in (e) and (a). (g) The estimated Gaussian-shaped temperature shift. (h) Temperature map error.

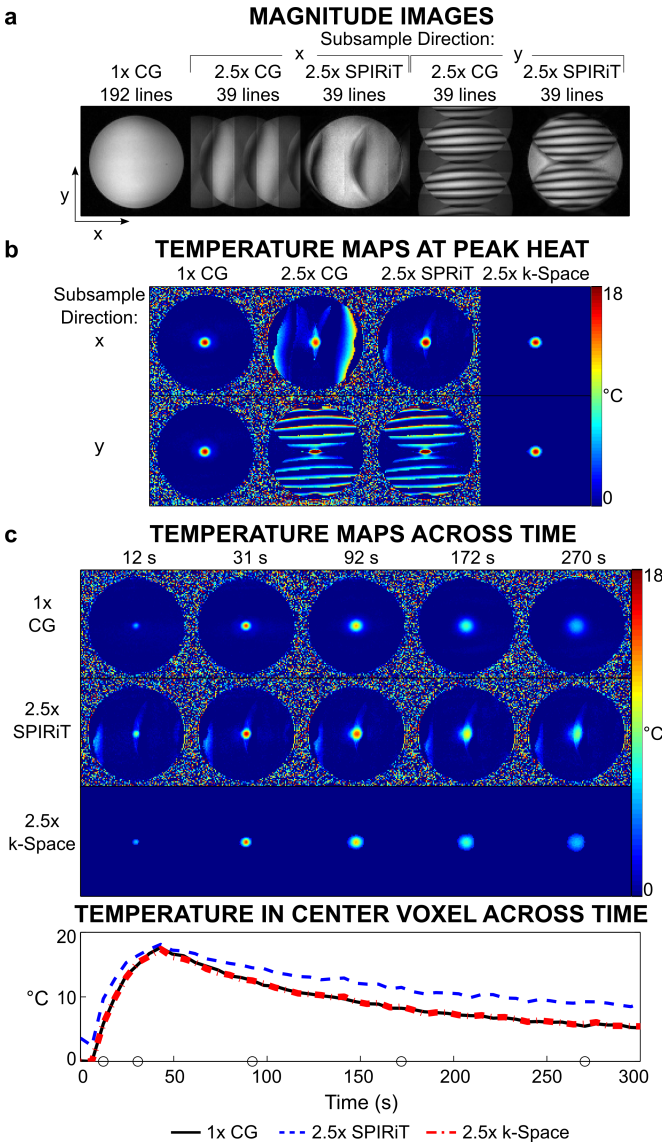

Figure 3.4: 2DFT experiment. (a) Magnitude images reconstructed with full sampling (left) and 2.5× undersampling in the *x*- or *y*-dimensions. (b) Temperature maps reconstructed at peak from data undersampled in either the *x* or *y* dimensions using CG, SPIRiT, and k-space-based methods. (c) Temperature maps reconstructed along the timecourse of the heating experiment using CG and full sampling (top), SPIRiT-reconstructed images and 2.5× undersampling along the *x*-direction (middle), and the k-space method and 2.5× undersampling along the *x*-direction (bottom). Plot of temperature evolution in the central voxel as a function of time for fully-sampled (CG) and 2.5×-undersampled (SPIRiT and k-space-domain) temperature maps. Circles along the *x*-axis indicate times of the displayed temperature maps.

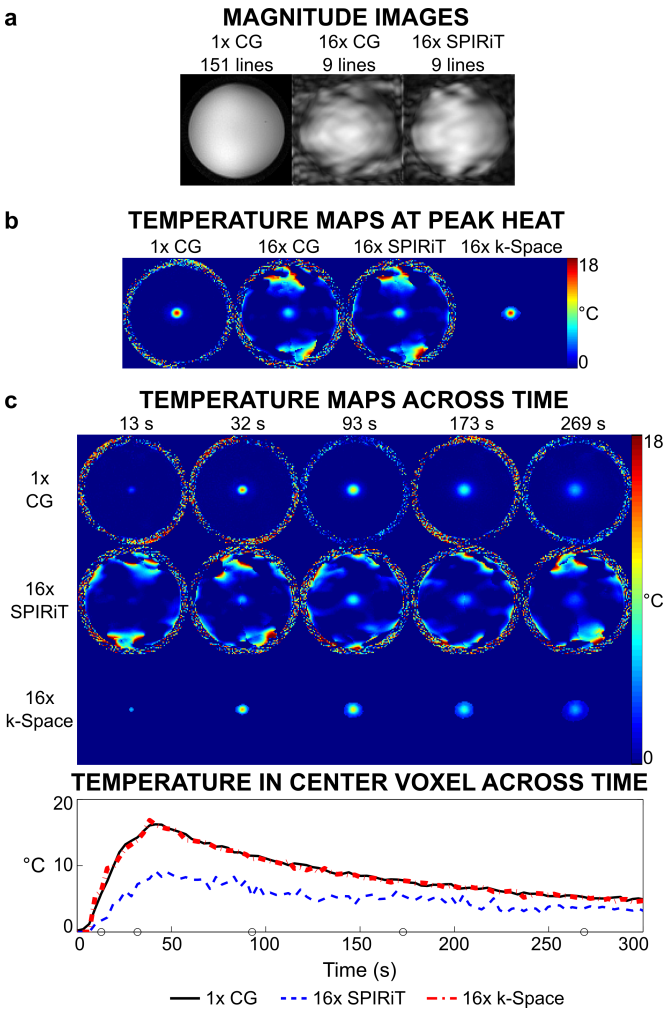

Figure 3.5: Golden angle radial experiment. (a) Magnitude images reconstructed with full sampling (left) and 16× undersampling with CG (middle) and SPIRiT reconstructions (right). (b) Temperature maps reconstructed at peak heat using fully-sampled CG and 16×-undersampled CG, SPIRiT, and k-space-based models. (c) Top: Temperature maps reconstructed along the timecourse of the heating experiment with full sampling using CG (top), 16×-undersampling using SPIRiT-reconstructed images (middle), and 16×-undersampling using k-space reconstruction (bottom). Bottom: Plot of temperature evolution in the central voxel as a function of time for fully-sampled (CG) and 16×-undersampled (SPIRiT and k-space-domain) temperature maps. Circles along the x-axis indicate times of the displayed temperature maps.

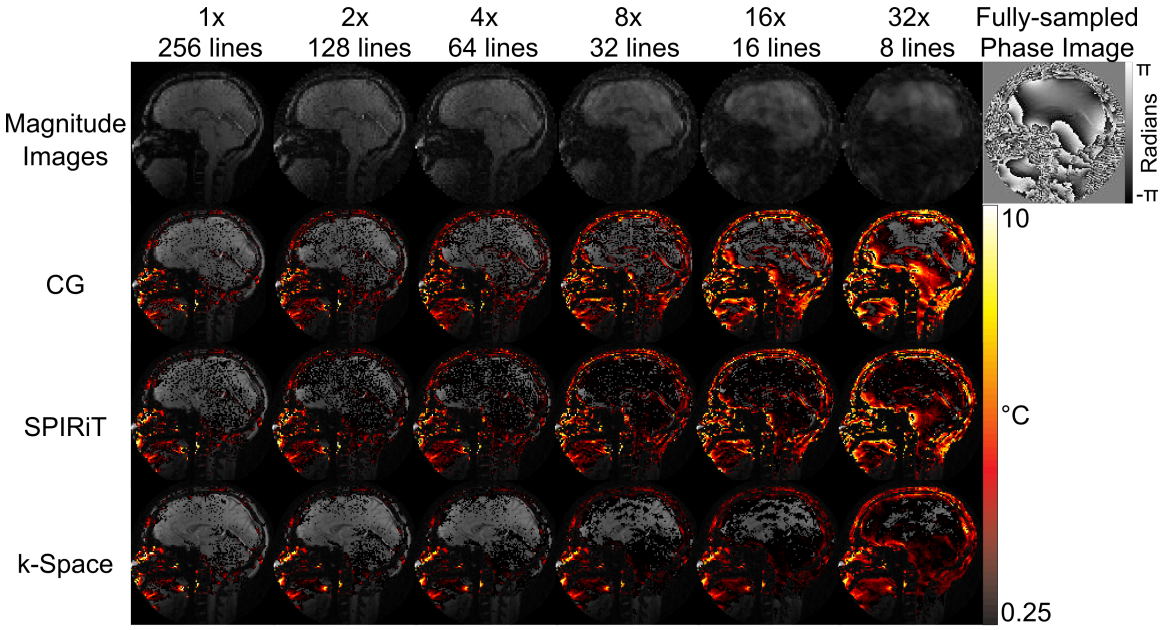

Figure 3.6: In vivo model validation (no heating). Top Row: Magnitude images reconstructed at different acceleration factors. The phase of one fully sampled image is shown at the top right. Bottom Three Rows: Comparison of mean positive temperature errors over 0.25°C for CG, SPIRiT, and k-space temperature reconstructions. Moderate acceleration leads to large temperature errors in the CG and SPIRiT reconstructions, but the k-space reconstructions suffer only an apparent loss in SNR in the brain up to 32× acceleration.

3.5.5 In vivo model validation

Figure 3.6 shows the in vivo model validation results. As expected, temperature errors increased with acceleration factor for all reconstruction methods. At high acceleration factors, the CG-reconstructed temperature maps have large errors, which are reduced but not removed by using SPIRiT. The k-space method's maps reflect a globally increased temperature uncertainty resulting from lower SNR, but no significant aliasing artifacts within the brain up to 32× acceleration.

3.5.6 Computation time

Table 5.1 shows the computation times for the proposed algorithm, averaged over 10 repeated reconstructions, for one temperature map from simulated and phantom heating

Table 3.1: Computation Time and Iteration Count

Dataset, acceleration factor	Time (s)	Number of iterations
Simulated phantom, 4×	74.1	Steps 1-5: 6; Step 6: 3
2DFT gel phantom, 2.5×	14.6	Steps 1-5: 3; Step 6: 3
GA radial gel phantom, 16×	8.2	Steps 1-5: 3; Step 6: 3

data. 2DFT reconstructions used approximately twice as many k-space samples per map as GA radial reconstructions, and required almost twice as much time (15 seconds vs 8 seconds for the same number of iterations).

3.6 Discussion

The proposed k-space-based temperature reconstruction approach was demonstrated in simulations and experiments to produce accurate temperature maps from undersampled k-space data. Temporal step response function simulations demonstrated that the method reconstructs 4×-undersampled temperature maps with finer temporal resolution than the TCR method, which uses temporal regularization to suppress undersampling artifacts. Small errors were observed around the edges of the hotspot due to thresholding (RMS error: 0.0047 °C; max error: 0.074 °C), but undersampling artifacts were not present in the k-space-based temperature reconstructions. Due to their broader temporal point spread function, TCR maps had large errors during rapid temperature changes, with a streaking pattern typical of radial undersampling (RMS error: 0.23 °C; max error: 2.98 °C). Although increased temporal regularization could have reduced TCR aliasing artifacts, this would have further decreased its effective temporal resolution. We note that this simulation was designed to compare the response of the two algorithms to large instantaneous temperature rises, which do not occur in practice. However, frame rates of one volume every few seconds are common in thermometry, especially with the desire to increase volumetric coverage. This leads to the possibility that large temperature changes can occur within one to two time frames,

and in such cases it is preferable that the reconstructed temperature maps have a temporal resolution that is no more coarse than the data frame rate. Future work will apply the proposed algorithm to enable expanded volumetric coverage in MR thermometry, without sacrificing temporal resolution.

Multicoil receive simulations demonstrated that the k-space algorithm benefits from multicoil reception. For 2DFT and GA radial trajectories, k-space temperature estimates from multicoil data had lower error within and outside the hotspot using as few as four (2DFT) and two (GA radial) readout lines. The results suggest that using multiple receive coils may be more advantageous for Cartesian trajectories, although additional experiments will be needed to evaluate this. In both Cartesian and non-Cartesian simulations, low-error temperature reconstructions were achieved at higher levels of acceleration using the k-space method compared to using parallel imaging alone.

A similar pattern was observed in phantom heating experiments. 2DFT and GA radial data were undersampled at $2.5\times$ and $16\times$, respectively. Results showed that undersampled k-space temperature reconstructions closely matched the fully-sampled temperature maps, and in both experiments the k-space reconstructions were free from aliasing artifacts. In comparison, SPIRiT-based temperature maps suffered from aliasing artifacts and degraded accuracy across the timecourse of the experiments. Unlike the SPIRiT-based temperature reconstructions, the accuracy of the k-space reconstructions was not significantly affected by the relative orientation of the undersampling and coil array dimensions, though it may be more sensitive to relative orientation at higher acceleration factors.

To validate the hybrid k-space signal model and investigate possible temperature errors that could arise in the method, data from a healthy volunteer were collected without heating. Above moderate acceleration factors, large errors became apparent in CG temperature reconstructions. SPIRiT maps also had high error at these factors, although they appeared diminished compared to CG results. Error maps from k-space reconstructions were affected by decreasing SNR, but no significant artifacts appeared until the data was acceler-

ated at 32×. These results suggest that the hybrid k-space signal model accurately captures anatomic phase variations and smooth phase shifts, over a wide range of acceleration factors in vivo. The results of the motion simulation further demonstrated the algorithm's ability to regress background anatomical phase in the presence of motion.

Compared to temporal regularization-based approaches such as TCR, the k-space-based algorithm makes no assumptions on the temporal dynamics of temperature, and was shown in simulations to provide superior temporal resolution to TCR. The k-space algorithm also does not require k-space undersampling patterns to change between consecutive acquisitions, as was demonstrated by the 2DFT phantom reconstructions, where the accelerated sampling pattern was held fixed for the entire duration of the experiment. However, higher accelerations may be possible with the proposed method if temporal regularization is added to the objective function in Eq. 3.2 and an alternating k-space sampling pattern is used.

While the proposed algorithm expands on the capabilities of hybrid multibaseline and referenceless thermometry [106], it also inherits some of its limitations. One is that the algorithm requires the assumption of focal heating to separate heat-induced phase shift from the polynomial phase shifts. Thus, in its current form the algorithm may not be suitable for imaging more diffuse heating patterns such as heating caused by RF electric fields generated by the MRI scanner (SAR), which may be well-modeled by polynomials. An extension to those cases would require development of new approaches to the background and heating phase separation problem, which could then be incorporated with the algorithm. If tissue motion occurs in a direction not captured by the baseline library, the method will also become inaccurate. However, if registration information is available to track this motion, it may be possible to reuse previously-acquired baseline images in the new orientation, since smooth phase shifts caused by reorientation of the tissue in the magnet could be captured by the polynomial phase shift. Finally, like the original hybrid thermometry method the proposed algorithm does not account for the presence of fat in heated voxels. Because fat experiences a negligible frequency shift with temperature, its signal degrades the accuracy

of temperature estimates when it is present in a voxel but not accounted for. While it is common to suppress fat in PRF-shift thermometry acquisitions using spectral-spatial excitations [164], its signal can be used for thermometry based on changes in longitudinal or transverse relaxation rates, or as a temperature-independent phase or frequency reference for PRF-shift thermometry. In those scenarios multi-echo acquisitions can enable separation of water and fat signals. To apply the proposed k-space algorithm to such acquisitions, a multi-echo signal model would need to be developed that comprises both water and fat components, and that solves for a heat-induced frequency shift (rather than a phase shift) in water. Such a model would incorporate previously-acquired and separated water and fat baseline images. Extensions of the original hybrid method have been developed that estimate heat-induced frequency changes from multi-echo acquisitions [165], and that use fat images as a phase reference for PRF thermometry [124].

For the current implementation of the algorithm, the measured compute times for one frame were on the order of 8-15 seconds. While not compatible with real-time clinical use, these times are feasible for retrospective reconstructions that would be useful for preclinical studies [166]. Furthermore, the current implementation used only one CPU core, and a multi-threaded or GPU-based implementation of the algorithm may yield compute times compatible with real-time use [144]. The presented reconstructions also used a non-uniform Fast Fourier Transform algorithm to evaluate multiplications with the $\boldsymbol{G}$ matrix, which includes a computationally-expensive gridding step [159]. This step could be eliminated for Cartesian-sampled data (2DFT and EPI), which are the most commonly-used k-space trajectories in thermometry. Finally, initializing the algorithm with a previous solution for the temperature map, baseline weights and polynomial coefficients could help accelerate convergence, particularly when little or no motion is present. As for any reconstruction approach, multi-slice temperature reconstructions could be parallelized across slices, so the in-plane acceleration enabled by a real-time-compatible extension of the proposed algorithm could be leveraged to increase the number of acquired slices, without

sacrificing temporal resolution. Further development of the algorithm to achieve real-time compute times will be the focus of future research efforts.

3.7 Conclusions

Accelerated temperature imaging is important to support current and enable future MRI-guided thermal interventions. We have presented an algorithm for temperature reconstruction by fitting a constrained model directly to k-space data. The proposed algorithm is capable of estimating focal temperature changes from k-space data with high temporal resolution and accuracy, even at high acceleration factors.

3.8 Acknowledgements

The authors would like to thank Ryan Robison and David Smith for help with golden angle radial acquisitions. This work was supported by NIH grant NCI 1R25CA136440-01 and the Howard Hughes Medical Institute / Vanderbilt University Medical Center Certificate Program in Molecular Medicine.

3.9 Appendix

3.9.1 NLCG algorithm for $\boldsymbol{\theta}$ updates

The steps of the nonlinear conjugate gradient algorithm (J A Fessler, *Image reconstruction: Algorithms and Analysis*, to be published.) used to update the heating-induced phase shift $\boldsymbol{\theta}$ in Step 3 of the algorithm are:

1: **repeat**

2: Calculate search direction $\boldsymbol{p}$: A column vector $\boldsymbol{g} = \nabla_{\boldsymbol{\theta}}\Psi$ of the first derivatives of the objective function $\Psi(\boldsymbol{\theta})$ in Eq. 3.4 with respect to the elements of $\boldsymbol{\theta}$ is first

calculated as:

$$\boldsymbol{g}^n = \nabla_{\boldsymbol{\theta}}\Psi = \Re\left\{\iota \text{diag}\left\{f_j^* e^{-\iota\theta_j^n}\right\}\boldsymbol{G}'\left(\tilde{\boldsymbol{y}} - \boldsymbol{G}\text{diag}\left\{e^{\iota\theta_j^n}\right\}\boldsymbol{f}\right)\right\}, \tag{3.7}$$

where $\boldsymbol{G}$ is a (non-uniform) DFT matrix. Using the Polack-Ribière conjugate gradient formula, the search direction at iteration n is given by:

$$\boldsymbol{p}^n = \begin{cases} -\boldsymbol{g}^n, & n = 0 \\ -\boldsymbol{g}^n + \frac{\langle \boldsymbol{g}^n - \boldsymbol{g}^{n-1}, \boldsymbol{g}^n \rangle}{\|\boldsymbol{g}^{n-1}\|^2}\boldsymbol{p}^{n-1}, & n \geq 1 \end{cases} \tag{3.8}$$

3: Calculate step size α: α is evaluated subject to non-positivity constraints as follows: If $\theta_j^n > \varepsilon$ for some threshold ε ($\varepsilon = \pi/1000$ was used in the present work) and $p_j^n > 0$, then set $p_j^n = 0$ since the search direction will lead to violation of the non-positivity constraint at that location, for any α. Then solve

$$\alpha_n = \underset{\alpha}{\text{argmin}}\,\Psi(\boldsymbol{\theta^n} + \alpha\boldsymbol{p}^n) \tag{3.9}$$

using a backtracking line search. Next, determine if the α returned by the line search causes violation of the non-positivity constraint. Let $\boldsymbol{z}^n = \boldsymbol{\theta}^n + \alpha_n\boldsymbol{p}^n$. If $[\boldsymbol{z}^n]_- \neq \boldsymbol{z}^n$, then set

$$\boldsymbol{p}^n = [\boldsymbol{z}^n]_- - \boldsymbol{\theta}^n \tag{3.10}$$

and perform another backtracking line search with the updated $\boldsymbol{p}^n$:

$$\alpha_n = \underset{\alpha\in[0,1]}{\text{argmin}}\,\Psi(\boldsymbol{\theta^n} + \alpha\boldsymbol{p}^n) \tag{3.11}$$

4: Update $\boldsymbol{\theta}$: $\boldsymbol{\theta}^{n+1} = \boldsymbol{\theta}^n + \alpha\boldsymbol{p}^n$

5: **until** The desired number of iterations is reached.

Chapter 4

Spatially-segmented undersampled temperature map reconstruction for transcranial MR-guided focused ultrasound

4.1 Abstract

MR-guided focused ultrasound (MRgFUS) brain systems deliver targeted thermal energy into the brain using a hemispheric transducer array that surrounds the head with an intervening water bath. Physical constraints imposed by the transducer limit the placement of MRI receive coils, precluding the use of parallel imaging for accelerated scanning. However, accelerated temperature imaging is desirable to improve spatiotemporal coverage during MRgFUS procedures in the brain, and can be achieved by undersampling k-space. While circulating water in the bath prevents skull overheating, it also creates signal variations that disrupt correlations between images collected before and during treatment (which are relied on to overcome undersampling artifacts), leading to errors in temperature measurements. We propose a spatially-segmented iterative reconstruction method, which applies the k-space hybrid model to reconstruct temperature changes in the brain and a nonlinear conjugate gradient method to reconstruct the image in the water bath. We evaluate the method using 2DFT Cartesian and golden angle (GA) radial data of gel phantom heating, and 2DFT data of in vivo thermal ablation treatment in a patient. Results show that separately reconstructing brain and water bath signal results in lower temperature error when undersampling k-space using single and multiple receive coils.

4.2 Introduction

Within the past ten years, MRgFUS has emerged as a viable treatment modality for several conditions in the brain. Preliminary studies are investigating the efficacy of targeted thermal heating delivered by MRgFUS for treating conditions such as essential tremor

[44, 50, 45], chronic neuropathic pain [7], parkinson's disease [51, 52], obsessive compulsive disorder [53], and brain tumors [4, 49]. In cases where it is applicable, primarily those targeting central structures of the brain such as the thalamus, the potential benefits of MRgFUS therapy are promising. With no incisions, the risk of damage to surrounding brain structures and cortical tissue is dramatically lower than with invasive procedures. For this reason, MRgFUS may be the only treatment option in otherwise inoperable situations [4, 58].

Transcranial MRgFUS systems comprise a hemispheric 1024-element ultrasound phased array transducer spanning 30 cm in diameter. The patient's head is positioned in the device and immobilized by a stereotactic frame. Degassed water fills the space between the transducer and the head, and is contained by a rubber membrane that allows direct contact between the water and scalp [58]. The water bath couples ultrasound energy between the transducer and the body, and is chilled to 15-20°C in order to dissipate heat from the head. Heat absorption in the skull is 30-60 times higher than in tissue, and therefore poses a risk of overheating if it is not cooled [4]. Figure 4.1a illustrates a cross sectional view of the transducer and water bath positioned around the patient's head.

Accelerated temperature mapping is desirable to increase spatial coverage during transcranial MRgFUS treatment, in which monitoring is currently limited to only one 2D image slice. However, the use of parallel imaging methods to increase scan efficiency is limited because MRI coils must be placed outside the transducer, far away from the head. Specialized coils that can be integrated with the transducer are under development, and will be able to offer valuable signal-to-noise improvements as compared to the body coil [89, 55]. Multiple groups have developed accelerated temperature mapping methods from undersampled k-space data that exploit temporal correlations between baseline (pre-treatment) and dynamic (during treatment) images to overcome undersampling artifacts [91, 145, 167].

While the water bath enables transcranial applications of MRgFUS, it presents unique challenges in the reconstruction of temperature maps, particularly from undersampled MRI

data. Specifically, circulating water in the bath between focused ultrasound sonications prevents thermal damage from skull heating, but also causes dynamic signal changes that are not captured by baseline images (Fig 4.1b). This breaks correlations between images collected during a single focused ultrasound sonication, and results in temperature map artifacts. Even with fully-sampled images, motion of water in the bath causes artifacts in the brain image. A larger field of view is also required to include the water bath in the image without incurring foldover artifacts in the brain. The water bath volume can be estimated to be roughly 6 liters based on the hemispheric transducer volume, and by approximating the head displacement to be on the order of the average brain volume (about 1200 cm^3 [168]).

A possible solution to reduce complications associated with the water bath is to alter the water to have low MR signal. An acceptable contrast agent would need to be both biologically safe and acoustically transparent. Although deuterated water (^2H_2O, or D_2O) has low MR signal, it has been shown to have negative effects on cell function and structure. It impairs mitosis, metabolism, and DNA synthesis, and has been shown to be an effective treatment against multiple human pancreatic cancer cell lines because of its toxicity [169, 170, 171]. Exposure of biological tissue to D_2O leads to substitution of hydrogen with deuterium in molecules, which forms stronger bonds. Deuterium-carbon bonds are roughly ten times stronger than hydrogen-carbon bonds, and do not readily revert back to the hydrogen-carbon form. Bonds with oxygen, nitrogen, and sulfur are also stronger with deuterium than with hydrogen, but do undergo exchange between deuterium and hydrogen when immersed in water [172]. As MRgFUS procedures often last a few hours, patients are in direct contact with the water for extended periods. This suggests some method of neutralizing the potential safety risks would be required before introducing deuterated water in the bath.

Another approach to reduce water bath signal is to add gadolinium (Gd) to the water. While also toxic, chelated forms of Gd, such as Gd-DTPA, have been used safely in patients without renal complications to enhance MR signal by decreasing T_1 relaxation times. At

concentrations of 20 mM or more, Gd-DTPA causes signal loss resulting from shortened T_2 relaxation times [173]. The relaxation rate $1/T_2^*$ in the presence of Gd-DTPA can be described using the relation $1/T_2^* = 1/T_{2_0}^* + r_2^*[\text{Gd-DTPA}]$, where $1/T_{2_0}^*$ is the intrinsic relaxation, r_2^* is the relaxivity constant of Gd-DTPA, and [Gd-DTPA] is the concentration of contrast agent [174]. The relaxivity of Gd-DTPA in cool water (24.5°C) has been measured as 5.09 $mM^{-1}s^{-1}$ at 3T. T_2 of the water without Gd-DTPA was measured as 1.72 s [175]. Substituting these values for r_2^* and as an approximation for $T_{2_0}^*$, respectively, results in a relation between [Gd-DTPA] and the desired value of $1/T_2^*$. The value of $1/T_2^*$ required to reduce image intensity in the water bath by a given factor can be obtained from the signal equation for gradient echo MRI: $S = \frac{M_0 sin\phi(1-e^{-T_R/T_1})}{1-cos\phi e^{-T_R/T_1}} e^{-T_E/T_2^*}$, where M_0 is the initial magnetization signal, ϕ is the flip angle, T_R is the repetition time, and T_E is the echo time [95]. In an in vivo MRgFUS thermal ablation treatment (with 13 ms T_E, 28 ms T_R, and 30° flip angle), the peak signal in the water bath was 3.4× higher than in the brain. To reduce the peak water bath signal to 10% of the peak brain signal would require a 53 mM concentration of Gd-DTPA, whereas 88 mM of Gd-DTPA would be needed to reduce it to 1% of the peak brain signal. However, one consequence of high Gd-DTPA concentrations is an increased susceptibility effect, which causes signal loss in nearby pixels because of increased local field inhomogeneity at echo times longer than 1 ms [174, 173]. While this could be ignored in the water bath itself, its effect on pixels near the skull surface, where the risk of overheating is greatest, should be considered. Additionally, an investigation into whether high concentrations of Gd-DTPA in the water bath would affect ultrasound wave propagation would be needed. Concerns that the chelate structure could be damaged by focused ultrasound, leading to the release of free Gd, have been noted [176]. Although Gd-based microbubbles have been developed [177], their echogeneity would interfere with ultrasound coupling into the body, and reflections arising from the bubbles may potentially damage the transducer. Additional investigation is also needed to assess whether high Gd-DTPA concentrations in the water bath will affect radiofrequency (RF) signal conduction.

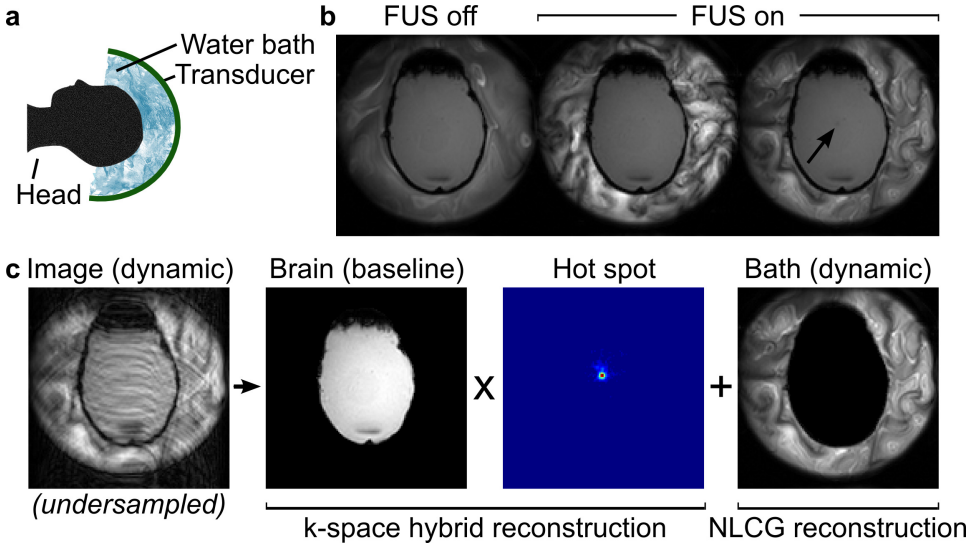

Figure 4.1: Spatially-segmented reconstruction model. (a) During MRgFUS treatment, the patient's head is immobilized in the transducer and circulating water bath. (b) The water bath signal varies significantly during a single focused ultrasound (FUS) sonication, which can obscure correlations between images (arrow indicates sonication target in gel phantom). (c) In the proposed method, undersampled dynamic data are reconstructed using the k-space hybrid method in the brain and NLCG in the water bath.

Instead of altering the water bath, we propose a spatially-segmented approach for reconstructing temperature maps in brain MRgFUS, in which we separately estimate a water bath image without a baseline, and a temperature map in the brain with a baseline (Fig 4.1c). The method can estimate temperature maps from undersampled data during brain MRgFUS treatments with low artifacts from single and multiple receive coil data, and can be combined with parallel imaging methods when multiple receive coils are available.

4.3 Methods

Figure 4.1c illustrates the overall undersampled dynamic image model. Our iterative approach alternates between updating the parameters of a k-space hybrid signal model which is fit in the brain region of the image (Fig 1.4) [167], and a baseline-free estimate of the water bath image. Fitting the k-space hybrid brain model results in a phase drift-corrected brain image without the temperature phase shift and a sparse temperature

phase shift map [167]. The water bath is reconstructed using a non-linear conjugate gradient (NLCG) algorithm that incorporates a sparsity penalty using Wavelet ℓ_1 regularization [167, 86].

4.3.1 Experimental Data

A gel-filled human skull phantom was sonicated by an Insightec ExAblate Neuro 4000 transcranial MRgFUS system (Insightec Ltd, Haifa, Israel) and imaged at 3T using the body coil (MR750, GE Healthcare, Waukeshaw, WI). A patient received MRgFUS thermal ablation treatment at 3T (Signa Excite, GE Healthcare, Milwaukee, WI; ExAblate Neuro, Insightec Ltd., Haifa, Israel) with 8 receive coils.

2DFT gradient echo images were collected with 13 ms TE, 28 ms TR, $28\times28\times0.3$ cm^3 field of view, 256×128 acquisition matrix, and 30° flip angle. In vivo SENSE maps were estimated by reconstructing the average k-space data across dynamics and dividing by the sum-of-squares image [85]. To test the method with non-Cartesian acquisitons, k-space data from the phantom heating experiment were resampled onto a golden angle (GA) radial trajectory. Images and maps were reconstructed to a 128×128 matrix and retrospectively undersampled as illustrated in Fig 4.2.

Temperature change maps of phantom heating were reconstructed by fitting the k-space hybrid model to the entire image, or to the brain only with keyhole (2DFT) or NLCG methods used to reconstruct the water bath image [139]. In vivo MRgFUS treatment maps were calculated by phase difference of SENSE-reconstructed images, and by k-space hybrid in the brain and NLCG + SENSE in the water bath.

4.4 Results

Figure 4.3 shows phantom heating results. When the k-space hybrid model is fit to the entire image, phase artifacts obscure the hot spot in the reconstructed temperature map and lead to an overestimation of the temperature rise in the sonicated region across image dy-

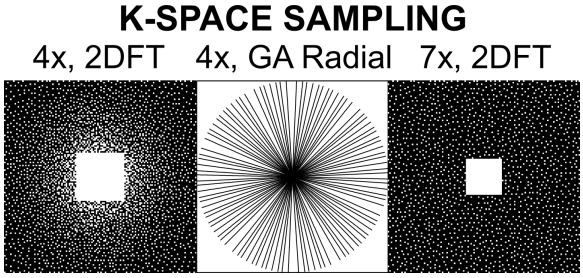

Figure 4.2: Retrospective k-space sampling for phantom heating (4× undersampled) and in vivo MRgFUS treatment (7× undersampled) reconstructions.

namics. Applying k-space hybrid only within the brain, and using a keyhole reconstruction of the water bath image, results in lower temperature errors in the hot spot but still large errors outside. The proposed k-space brain/NLCG bath approach produces temperature estimates with much lower in-brain artifacts.

Figure 4.4 shows reconstructions from in vivo MRgFUS treatment. Temperature estimates from SENSE reconstructed images are similar on average to fully sampled maps in the hot spot, but contain large errors within the brain. These errors are reduced using the proposed k-space brain/NLCG bath method. Reconstructed magnitude images appear noisier and have higher error throughout using SENSE.

4.5 Discussion

Unpredictable water bath motion confounds model-based approaches to accelerated MR temperature mapping, resulting in large temperature artifacts due to aliased water bath signal. We demonstrated that applying a model-based reconstruction in the brain and an NLCG reconstruction in the water bath can reconstruct 4×-undersampled temperature maps with low error using a single receive coil. In vivo MRgFUS treatment data further demonstrated that the spatially-segmented approach achieved low temperature error at 7× acceleration as compared with SENSE image temperature maps. Magnitude images estimated by the k-space hybrid method in the brain (derived from the input baseline images

and corrected for phase drifts) and NLCG in the water bath had lower error than SENSE reconstructions of the dynamic images. Future work will include integrating the approach with other accelerated temperature mapping methods [91] and evaluating it with spiral trajectories [137]. Other potential appilcations of spatially-segmented reconstruction from undersampled data will also be investigated, including effects from bowel displacement in uterine fibroid treatment, which can be limiting, and other physiological motion in cardiac and abdominal treatments.

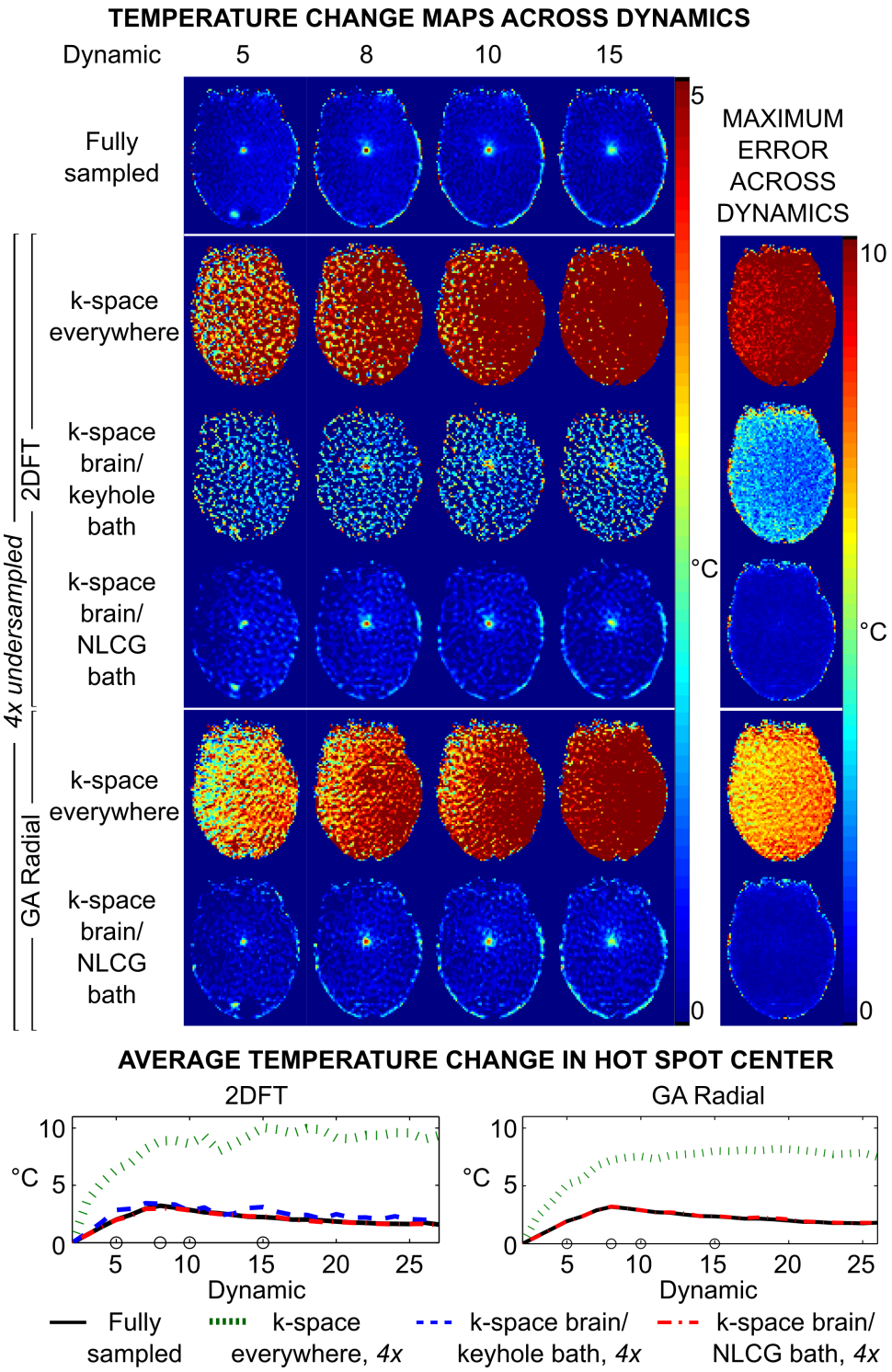

Figure 4.3: Reconstructed temperature changes and maximum temperature errors in the phantom with 4× undersampling using 2DFT and golden angle (GA) radial trajectories. Temperature change averaged over the hot spot center is plotted at the bottom for each reconstruction (circles on x-axis indicate dynamics of displayed maps).

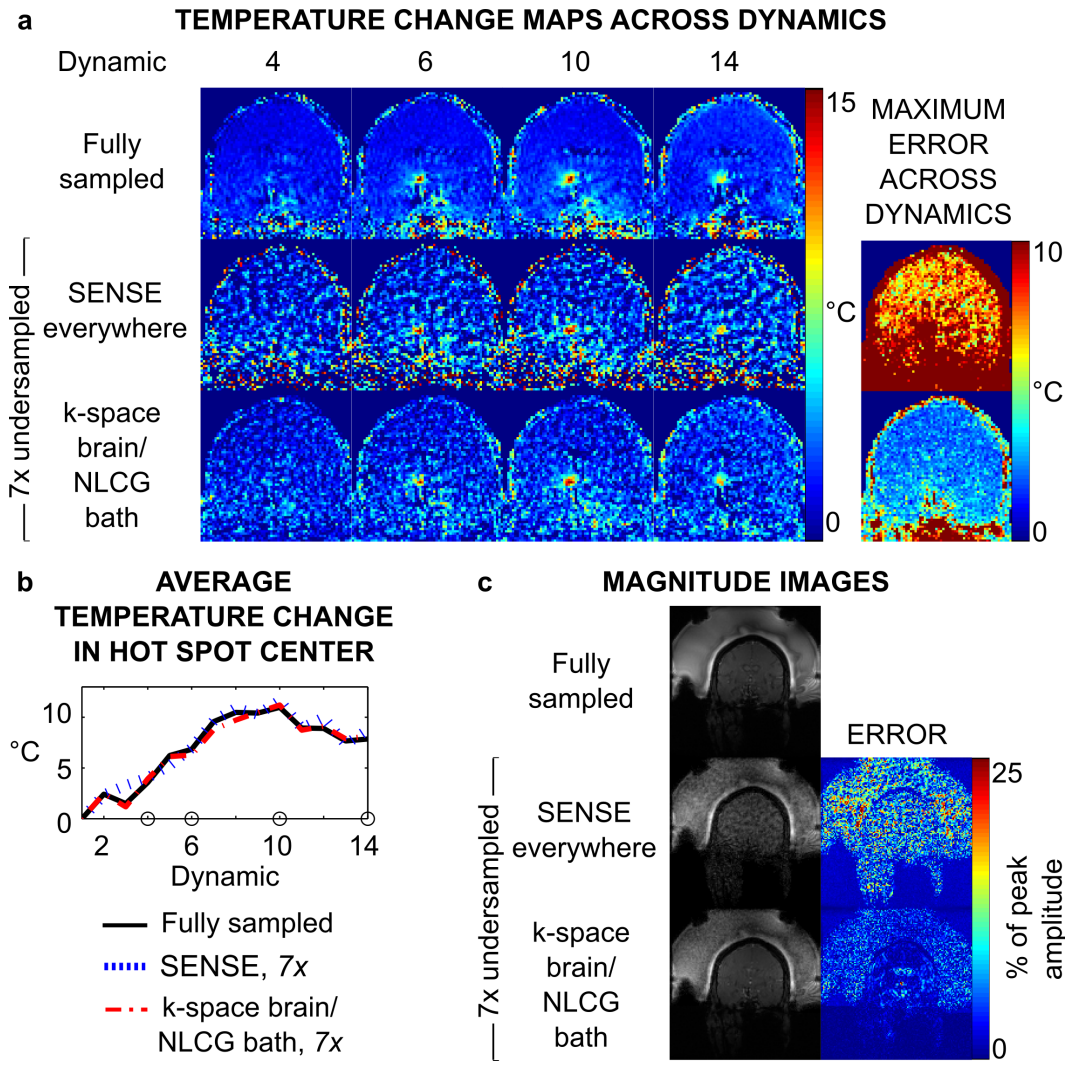

Figure 4.4: In vivo MRgFUS treatment results. (a) Temperature change maps and maximum error across dynamics. (b) Average temperature change in the hot spot is plotted for each reconstruction (circles on x-axis indicate dynamics of displayed maps). (c) Reconstructed magnitude images and errors are shown for each method.

Chapter 5

Correcting heat-induced chemical shift distortions in proton resonance frequency-shift thermometry

5.1 Abstract

Purpose: To reconstruct proton resonance frequency (PRF)-shift temperature maps free of chemical shift (CS) distortions.

Theory and Methods: Tissue heating created by thermal therapies such as focused ultrasound surgery (FUS) results in a change in PRF that causes geometric distortions in the image and calculated temperature maps, in the same manner as other CS and off-resonance distortions if left uncorrected. We propose an online-compatible algorithm to correct these distortions in 2DFT and EPI acquisitions, which is based on a k-space signal model that accounts for PRF change-induced phase shifts both up to and during the readout. The method was evaluated with simulations, gel phantoms, and in vivo temperature maps from brain, soft tissue tumor, and uterine fibroid FUS treatments.

Results: Without CS correction, peak temperature and thermal dose measurements were spatially offset by approximately 1 mm in vivo. Spatial shifts increased as readout bandwidth decreased, as shown by up to 4-fold greater temperature hot spot asymmetry in uncorrected temperature maps. In most cases the computation times to correct maps at peak heat were less than 10 ms, without parallelization.

Conclusion: Heat-induced PRF changes create CS distortions in temperature maps resulting from MR-guided FUS ablations, but the distortions can be corrected using an online-compatible algorithm.

5.2 Introduction

MR-guided focused ultrasound (MRgFUS) is a non-invasive therapeutic modality that uses ultrasound energy to selectively heat soft tissue, and concurrent MR temperature imaging for monitoring and dosimetry [71]. Most MRgFUS procedures rely on proton resonance frequency (PRF) shift-based thermometry. There are many potential sources of error in PRF-shift thermometry, including some that result from the heating itself [178, 11, 100]. For example, errors arising from temperature-induced susceptibility and conductivity changes in aqueous and fatty tissue have been characterized along with methods to correct them [101, 103, 102, 179].

In tissues sufficiently removed from fat such as the brain and uterine fibroids, the primary intrinsic source of error in PRF temperature maps is the same heat-induced chemical shift (CS) on which PRF-shift thermometry is based. The problem is that the PRF shift with heat results in off-resonance phase accrual across the signal readout window that blurs the reconstructed temperature map in and around the hot spot [104]. This is especially problematic when imaging is performed with a low pixel bandwidth (BW). For example, pixel BWs as low as 29 Hz are common in the 2DFT PRF sequences that guide MRgFUS brain ablations [4, 82], and are chosen to compensate the signal-to-noise ratio (SNR) penalty that results from moving receive coils away from the body to accommodate FUS transducers. At 3 Tesla, the proton resonance frequency changes 1.27 Hz/°C, so with a 29 Hz pixel BW the hot spot will shift by one pixel with a 22.7°C temperature rise; temperature increases in MRgFUS ablations are typically 20–30°C. Temperature magnitude errors also arise as hotter pixels blur into cooler pixels. Low pixel BWs in the phase-encoded dimension are also common in echo-planar imaging (EPI) sequences used to accelerate volumetric temperature scans [72, 145, 166, 59]. Multi-shot acquisition schemes can reduce these errors to some degree, but do not eliminate them entirely [104, 105]. Errors in temperature maps translate to errors in the thermal dose maps and maximum temperature measurements that are used to determine treatment endpoints [180, 43], and may thereby contribute to variabil-

ity in treatment outcomes. Finally, as MRgFUS procedures with tighter treatment margins are developed in the brain and other regions, even small spatial shifts and magnitude errors in temperature maps may impact safety and efficacy. Therefore, accurate temperature measurements are critical for effective treatment administration [75].

In this work, we present an algorithm to correct CS distortions in PRF-shift temperature maps. The algorithm is based on a k-space signal model [167] that accounts for PRF shift-induced phase accumulation up to and during the MR signal readout, and reduced image intensity that accompanies the PRF phase shift and is primarily caused by increasing T_1 with heat [71]. The method leverages computational efficiencies possible with Cartesian 2DFT and EPI trajectories to achieve online-compatible computation times. Simulations and phantom studies show that heat-induced CS distortions degrade the accuracy of temperature estimations, but that they can be corrected by the proposed method to produce accurate temperature maps. Improvements are shown to be more prominent at low readout bandwidths. Temperature hot spots in phantom heating experiments become progressively less symmetric as BW decreases, reflecting a temperature-dependent shift of heated pixels in one direction. CS-compensated thermometry is further demonstrated using patient data from brain, soft tissue tumor, and uterine fibroid MRgFUS treatments. Aspects of this work have been previously reported in Ref. [165].

5.3 Theory

5.3.1 Signal Model

The algorithm is developed as a post-processing step applied to an input heat-induced phase shift map $\theta(\vec{x})$ that is expected to suffer from CS distortions. It is compatible with any thermometry method that provides both an estimate of $\theta(\vec{x})$ and a baseline/pretreatment image $f(\vec{x})$, including baseline subtraction [128], multibaseline/atlas-based subtraction [129, 181, 182], and hybrid referenceless and multibaseline subtraction thermometry

[106]. $\theta(\vec{x})$ is corrected by fitting a model containing it and $f(\vec{x})$ to the k-space data of the image with heat. The model is given by:

$$y_i = \sum_{j=1}^{N_s} f_j e^{-\alpha_j} e^{-\iota\theta_j(1+t_i/T_E)} e^{-\iota\vec{k}_i\cdot\vec{x}_j} + \varepsilon_i, \tag{5.1}$$

where y_i is one k-space sample acquired at k-space location $\vec{k}_i$ at time t_i, N_s is the number of spatial locations $\vec{x}_j = (x_j, y_j, z_j)$, the $f_j \triangleq f(\vec{x}_j)$ are samples of the baseline image, the α_j are samples of a heat-induced image magnitude attenuation map, $\iota = \sqrt{-1}$, the $\theta_j \triangleq \theta(\vec{x}_j)$ are samples of the heat-induced phase shift map which is converted to a frequency shift map by dividing it by the echo time T_E, and the ε_i are i.i.d. complex Gaussian noise samples. The time points t_i are centered/zero at T_E. Phase shifts due to B_0 field drift are assumed to have been previously estimated and applied to $f(\vec{x})$ [128]. Of key importance for CS distortion correction is that this signal model accounts for phase shifts that evolve over the signal readout period due to the PRF shift; CS distortions appear in conventional temperature maps as a result of neglecting this term.

5.3.2 Problem Formulation

A corrected temperature map can be obtained by fitting the signal model in Eq. 5.1 to acquired k-space data samples d_i. Here, the model fitting objective is formulated as a constrained least-squares/maximum likelihood problem, given by

$$\begin{aligned} \text{minimize} \quad & \tfrac{1}{2}\textstyle\sum_{i=1}^{N_k} \left| d_i - \sum_{j=1}^{N_s} f_j e^{-\alpha_j} e^{-\iota\theta_j(1+t_i/T_E)} e^{-\iota\vec{k}_i\cdot\vec{x}_j} \right|^2 \\ \text{subject to} \quad & \theta_j \leq 0, j = 1,\ldots,N_s \\ & \alpha_j \geq 0, j = 1,\ldots,N_s, \end{aligned} \tag{5.2}$$

with respect to the θ_j and α_j. N_k is the total number of k-space samples. Since MRgFUS is a focal heating technique, it is expected that only a minority of image voxels will contain significant heating and require correction. Thus, the size of the problem can be reduced by

only updating $\theta(\vec{x})$ and $\alpha(\vec{x})$ in voxels in and around the peak of the hotspot. Given a set of heated image voxel indices $\mathbb{H}$, the objective in Eq. 5.2 can be equivalently written as:

$$\frac{1}{2}\sum_{i=1}^{N_k}\left|d_i-\sum_{j\in\mathbb{H}}f_j e^{-\alpha_j}e^{-\iota\theta_j(1+t_i/T_E)}e^{-\iota\vec{k}_i\cdot\vec{x}_j}-\sum_{j\notin\mathbb{H}}f_j e^{-\iota\vec{k}_i\cdot\vec{x}_j}\right|^2, \tag{5.3}$$

where $\theta_j=\alpha_j=0$ is assumed for $j\notin\mathbb{H}$. Defining $d_i^{\mathbb{H}}\triangleq d_i-\sum_{j\notin\mathbb{H}}f_j e^{\iota\vec{k}_i\cdot\vec{x}_j}$ as the k-space signal from voxels in the hot spot, Eq. 5.2 can be written as:

$$\begin{aligned}\text{minimize}\quad & \tfrac{1}{2}\textstyle\sum_{i=1}^{N_k}\left|d_i^{\mathbb{H}}-\sum_{j\in\mathbb{H}}f_j e^{-\alpha_j}e^{-\iota\theta_j(1+t_i/T_E)}e^{-\iota\vec{k}_i\cdot\vec{x}_j}\right|^2\\ \text{subject to}\quad & \theta_j\le 0, j\in\mathbb{H}\\ & \alpha_j\ge 0, j\in\mathbb{H}.\end{aligned} \tag{5.4}$$

Reducing the problem size in this way is key to enabling online implementation. The problem statement in Eq. 5.4 makes no assumptions about the number of image dimensions or the k-space trajectory used for the acquisition. An approach to efficiently solve it in one dimension for 2DFT and EPI acquisitions is detailed next.

5.3.3 Algorithm

Figure 5.1 illustrates the proposed CS distortion correction algorithm for 2D Cartesian (2DFT and EPI) acquisitions. It corrects distortions in one dimension, since off-resonance phase accrual occurs only in one dimension in these acquisitions (the frequency-encode dimension for 2DFT and the phase-encode dimension for EPI). Thus, the corrections can be performed independently (in parallel, if desired) for each index in the undistorted image dimension.

First, the discrete Fourier transform of the 2D k-space data of the image with heat is computed in the undistorted dimension (depicted in Fig. 5.1 as the row dimension), leaving the data in k-space in the distorted (column) dimension, and the set $\mathbb{H}$ of voxels with significant heating is identified by thresholding the input CS-distorted $\theta(\vec{x})$. Subsequent

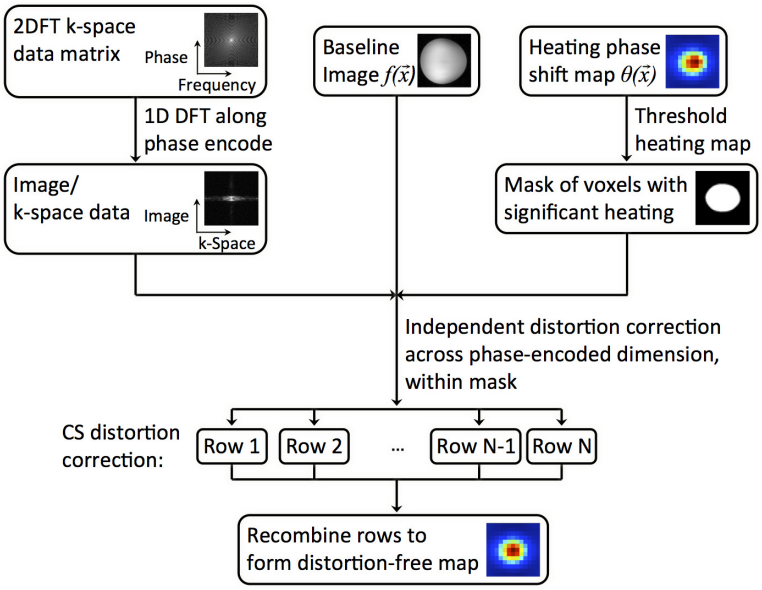

Figure 5.1: Proposed CS distortion correction algorithm for 2DFT data. Because distortion only occurs in the frequency-encoded dimension, the algorithm operates independently on each row of the image in the phase-encoded dimension. First, the the 2D k-space data of the image with heat is Fourier-transformed in the phase-encoded dimension, leaving the data in k-space in the frequency-encoded dimension, and the set of voxels with significant heating is identified by thresholding the input distorted heating phase shift map $\theta(\vec{x})$. CS Distortion correction is then performed on a row-by-row basis within the mask by solving the optimization problem in Eq. 4 (which requires the baseline image $f(\vec{x})$ as input), and the corrected rows are recombined to form the final CS distortion-corrected temperature map. To correct an EPI temperature map, the phase- and frequency-encoded dimensions of the input k-space data, images and maps would be swapped in the Figure.

calculations are performed on a row-by-row basis. For each image row the hot spot k-space signal samples $d_i^{\mathbb{H}}$ are computed from that row's k-space data and baseline image samples f_j for $j \notin \mathbb{H}$, and an iterative gradient descent algorithm is used to update the θ_j and α_j for $j \in \mathbb{H}$, until the differences between the modeled and acquired data are minimized. In each iteration, the derivatives of the objective function in Eq. 5.4 with respect to those variables are calculated as:

$$g_j^{\theta} = \Re\left\{\sum_{i=1}^{N_k} -\imath\,(1+t_i/T_E)\, f_j^* e^{-\alpha_j} e^{\imath\theta_j(1+t_i/T_E)} e^{\imath k_i x_j} r_i\right\} \tag{5.5}$$

$$g_j^{\alpha} = \Re\left\{\sum_{i=1}^{N_k} f_j^* e^{-\alpha_j} e^{\imath\theta_j(1+t_i/T_E)} e^{\imath k_i x_j} r_i\right\}, \tag{5.6}$$

where

$$r_i = d_i^{\mathbb{H}} - \sum_{j\in\mathbb{H}} f_j e^{-\alpha_j} e^{-\imath\theta_j(1+t_i/T_E)} e^{-\imath k_i x_j} \tag{5.7}$$

is the residual k-space error between the model and data. Given g_j^{θ} and g_j^{α}, the maps are updated as:

$$\theta_j \leftarrow \min\left(\theta_j - c g_j^{\theta}, 0\right) \tag{5.8}$$

$$\alpha_j \leftarrow \max\left(\alpha_j - c g_j^{\alpha}, 0\right), \tag{5.9}$$

where c is a fixed step size. Multiple receive coils can be accommodated by calculating g_j^{θ} and g_j^{α} separately for each coil (since the baseline image and k-space data will be coil-specific) and then summing them across coils prior to the updates. Once the iterations converge, the rows of the θ matrix are recombined to form the final CS distortion-corrected temperature map.

5.4 Methods

5.4.1 Algorithm Implementation

The algorithm was implemented as a MATLAB script (Mathworks, Natick, MA, USA), a C-based MATLAB MEX function, and in Python[1]. In all cases that follow, the image domain hybrid algorithm was used to calculate initial temperature phase shift maps $\theta(\vec{x})$ [106]. In addition to calculating the initial $\theta(\vec{x})$ maps, the algorithm estimated zeroth-order polynomial background phase shifts to compensate B_0 drift. Those phase shifts were then applied to the baseline images to form the drift-compensated baseline images $f(\vec{x})$ used in the CS correction algorithm.

5.4.2 Simulations

Simulations were performed to model 2DFT gradient-recalled echo (GRE) temperature mapping scans at 3T. A circular phantom was simulated, and $\theta(\vec{x})$ maps were Gaussian-shaped with FWHM of 0.8 pixels and peak amplitudes between 0 and π. The same Gaussian hot spots were scaled to obtain exponential image intensity attenuation (α) maps with peaks of 0, 0.4 and 0.8, to reflect a range of T_1 and T_2^* dependence on temperature. With a factor of 0.8, at peak heat the image intensity is reduced by 55%. The phase shifts and image magnitude attenuations were applied to the phantom and k-space data were generated using 78, 156, 313, and 625 Hz pixel BWs. The simulations used a 64×64 matrix size, 20×20 cm^2 field-of-view (FOV), and a 16 ms echo time (TE), corresponding to a peak temperature rise of 24.5°C for a π phase shift. The phantom and hot spot are illustrated in Figure 5.2a. Images were normalized by their median absolute value prior to processing. The temperature phase shift maps returned by the hybrid algorithm were CS-corrected

[1]Those codes are available at https://bitbucket.org/wgrissom/prf-cs-corr/downloads. The algorithm is also available as an online plugin for both the Philips SonAlleve MR-HIFU system (Philips Healthcare, Vantaa, Finland) and the RTHawk 2.0 Research Platform (Heart Vista, Menlo Park, CA, USA); the authors can provide those plugins upon request.

using the proposed algorithm, with and without joint image magnitude attenuation ($\alpha(\vec{x})$) estimation in order to separately investigate the effects of image magnitude attenuation on the quality of CS distortion correction. Image magnitude attenuation estimates were excluded from the algorithm by skipping the $\alpha(\vec{x})$ update (Eq. 5.9). The uncorrected heat-induced phase change maps were thresholded at 0.01 radians (0.1°C) to identify voxels with significant heating (Fig 5.1), and temperature root-mean-square-error (RMSE) was calculated for each map within those significant voxels. A step size of $c = 10^{-4}$ was used in the gradient descent algorithm (Eqs. 5.8 and 5.9).

5.4.3 Phantom heating experiments

A gel phantom was heated using a Sonalleve V2 MR-HIFU system (Philips Healthcare, Vantaa, Finland) with a focus trajectory that treated a 4 mm-diameter ablation cell at 110 W at 1.2 MHz for 41 s. Coil-combined images were acquired at 3T (Achieva, Philips Healthcare, Best, Netherlands) with 5 receive coils, 16 ms TE, and 7 mm slice thickness. 2DFT data were collected with 32 ms TR, 20×20 cm^2 FOV, 96×96 matrix, and 44.4, 88.8, 177.5, 500.1, and 1001.6 Hz pixel BW. EPI data were collected with 34 ms TR, 20×20 cm^2 FOV, 112×112 matrix, and EPI factor/pixel BW (Hz) of: 3/353.9, 7/186.2, 11/120.6, 15/89.4, 19/71.0, 23/59.0, and 27/50.5. Images were normalized by their median absolute value prior to temperature map processing. The uncorrected heat-induced phase change maps were thresholded at a level of 0.5 radians (3.9°C) to identify voxels with significant heating. Step sizes were empirically tuned to $c = 10^{-4}$ (2DFT) and 10^{-5} (EPI) (Eqs. 5.8 and 5.9). To measure hot spot asymmetry before and after CS corrections, the temperature maps were interpolated to a 10× finer grid, and then flipped in the CS-distorted dimension and aligned to the unflipped maps by maximizing correlation. Asymmetry was then calculated as the root-mean-square difference between the maps within a region of interest (ROI) around the hot spot, which had a 40 pixel radius from the voxel with peak heat. Baseline temperature map asymmetry due to noise was also measured in the same

ROI in an image frame collected before the start of sonication.

5.4.4 In vivo MRgFUS ablations

Brain 2DFT data were acquired during brain sonications at 3T (Signa Excite, GE Healthcare, Milwaukee, WI, USA; ExAblate Neuro, Insightec Ltd., Haifa, Israel) with 8 receive coils, 28 ms TR, 12 ms TE, 28×28 cm^2 FOV, 256×256 matrix, 3 mm slice thickness, and 44 Hz pixel BW. Informed written consent was obtained for patients enrolled in the treatment study. Data from 2 brain sonications (axial and sagittal image orientations; 14 image frames each) targeting the same focal region were processed, using joint estimation across coils for CS correction. Images were normalized by their median absolute value prior to processing. Initial temperature maps were reconstructed in a 128×128 submatrix of the images that covered the anatomy of interest. The uncorrected heat-induced phase change maps were thresholded at a level of 0.5 radians (5.2 °C) to identify voxels with significant heating. To exclude phase variations unrelated to the treatment from the CS correction algorithm, an ROI mask centered around the sonication region was applied to the thresholded mask. An empirically-tuned step size of $c = 10^{-5}$ was used in the gradient descent algorithm.

Leg Soft Tissue Tumor 2DFT data were acquired during leg sonications at 3T (Signa, GE Healthcare, Milwaukee, WI, USA; ExAblate 2000, Insightec Ltd., Haifa, Israel) 25 ms TR, 12 ms TE, 28×28 cm^2 FOV, 256×256 matrix, 5 mm slice thickness, and 44 Hz pixel BW. The treatment was performed with informed consent and approval from the Institutional Review Board at Stanford University. Data from 94 sonications of a soft tissue tumor in the leg (10 image frames each) over many adjacent focal targets were processed. Images were normalized by their median absolute value prior to processing. Initial temperature maps were reconstructed in a 192×192 matrix subset of the images, covering the anatomy of interest. The uncorrected heat-induced phase change maps were thresholded at a level of 0.25 radians (2.6 °C) to identify voxels with significant heating. Whenever possible,

an ROI mask manually drawn around the sonication region was also applied to the thresholded temperature map mask, to exclude erroneous temperature spikes arising from blood pulsation. An empirically-tuned step size of $c = 10^{-4}$ was used in the gradient descent algorithm.

Uterine Fibroid EPI data were acquired during a patient uterine fibroid ablation procedure at 3T (Achieva, Philips Healthcare, Best, Netherlands; Sonalleve V2, Philips Healthcare, Vantaa, Finland) with 5 receive coils, 26 ms TR, 16 ms TE, 40×30 cm^2 FOV, 192×192 matrix, 7 mm slice thickness, 13 shots, and 79 Hz pixel BW in the phase-encode direction. The treatment was performed with informed consent and approval from the Institutional Review Board at Vanderbilt University. Coil-combined images from 25 sonications over multiple focal targets in the fibroid were collected (ranging from 1 to 28 frames, with median 27 image frames per sonication). Images were normalized by their median absolute value prior to processing. Initial temperature maps were reconstructed in a 96×96 matrix subset of the images, covering the anatomy of interest. The uncorrected heat-induced phase change maps were thresholded to be within 0.5 and 4 radians to identify voxels with heat-related phase changes within an ROI centered around the sonication region. The upper threshold was used to exclude large phase variations arising from the tissue-air interface. An empirically-tuned step size of $c = 10^{-5}$ was used in the gradient descent algorithm.

5.5 Results

5.5.1 Simulations

Figures 5.2 and 5.3 show the simulation results. Figure 5.2b shows estimated temperature maps compared to the true map at the lowest pixel bandwidth of 78 Hz, at peak heat and peak image magnitude attenuation. The uncorrected hot spot is blurred in the frequency-encoded dimension. CS correction without joint image magnitude attenuation estimation mostly corrected the map, but errors of approximately ±1°C remained. CS correction with

joint image magnitude attenuation estimation achieved the lowest error. Figure 5.3 plots of temperature RMSE in the hot spots, as a function of pixel bandwidth, temperature, and maximum image magnitude attenuation factor. Maximum temperature RMSE across all cases for uncorrected, CS-only corrected, and joint CS and attenuation corrected maps was 0.73°C, 0.18°C, and 0.09°C, respectively. The uncorrected maps' errors are largest at low bandwidths and at high peak temperatures. CS correction with joint image magnitude attenuation results in the lowest error for each pixel BW, maximum temperature and image magnitude attenuation.

Figure 5.4 illustrates algorithm performance as a function of the step size c used in the CS correction algorithm, for the largest temperature rise, lowest pixel BW, and largest peak attenuation. Too large a step size causes the algorithm to diverge immediately and stop prematurely, while too small a step size causes the algorithm to use a large number of iterations and stop prematurely. However, the temperature RMSE and number of iterations remains small between approximately $c = 10^{-3}$ to $c = 10^{-5}$. The stepsize of $c = 10^{-4}$ used here minimized both the temperature RMSE and the number of algorithm iterations for this peak temperature, pixel BW and attenuation.

5.5.2 Phantom heating experiments

Figures 5.5-5.6 show the 2DFT and EPI phantom experiment results. Figures 5.5a and 5.6a show reconstructed temperature maps using no correction and CS correction without and with joint image magnitude estimation, and the image magnitude attenuation estimate (α), all at peak heat. The maximum temperature differed by up to 1°C between uncorrected and corrected maps. The peaks of the hot spots are shifted to the left by about one pixel in the CS distortion-corrected maps with joint attenuation estimation, and have a more symmetric appearance than the uncorrected maps. In the 2DFT case the map corrected with joint image magnitude attenuation estimation is visibly more symmetric than the map corrected without it. The peak image magnitude attenuation estimates were 0.91 for 2DFT

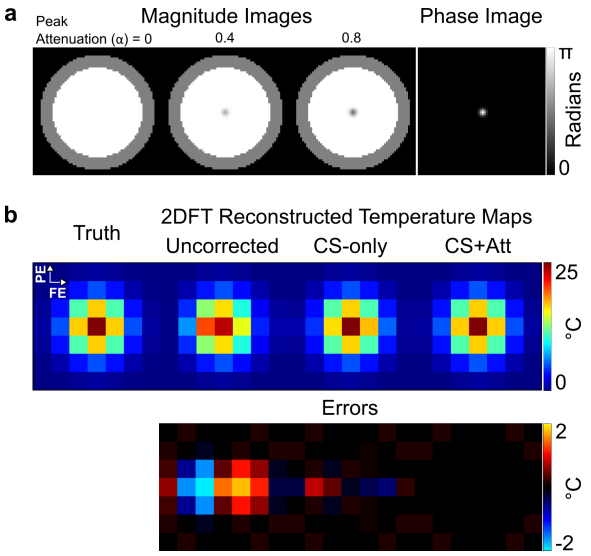

Figure 5.2: 2DFT Simulation setup (a) and reconstructed temperature maps (b). (a) Magnitude images with peak image magnitude attenuation and hot spot phase image. (b) Zoomed-in comparison between the true hot spot at peak heat (24.5°C, peak image magnitude attenuation of 0.8, 78 Hz per-pixel bandwidth), and temperature maps reconstructed without and with CS distortion correction, and without and with image magnitude attenuation estimation.

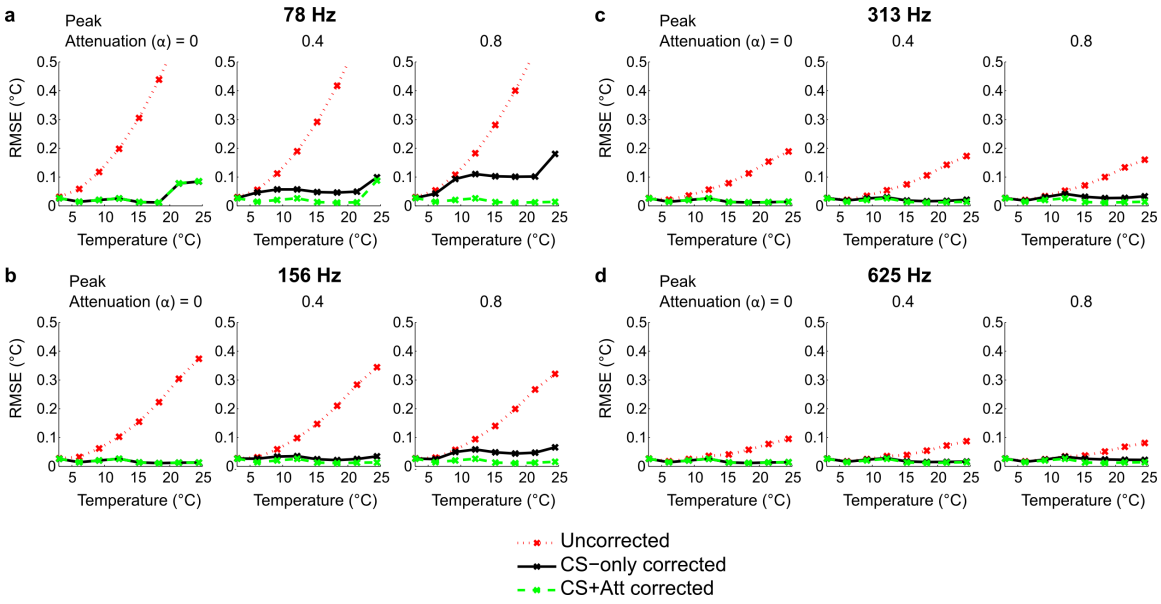

Figure 5.3: 2DFT simulation results. Temperature root-mean-square-error (RMSE) over hot spots of different peak temperatures at three attenuation factors with (a) 78 Hz, (b) 156 Hz, (c) 313 Hz, and (d) 625 Hz pixel BW. Compared to uncorrected temperature reconstructions, errors are lowest when CS and attenuation are accounted for in the reconstruction.

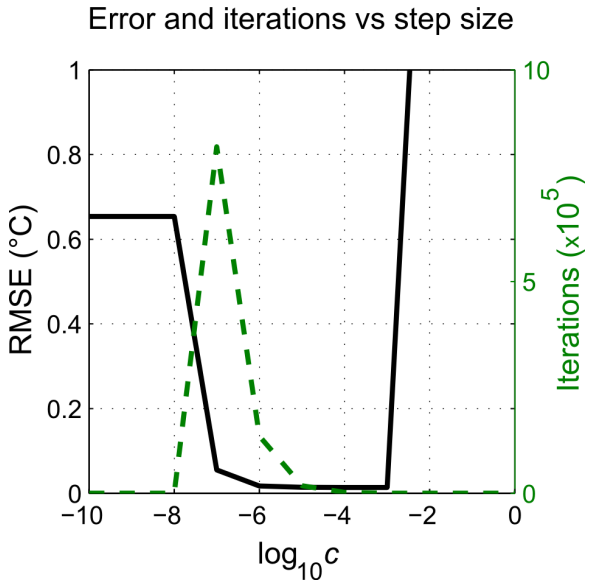

Figure 5.4: Temperature RMSE and number of algorithm iterations as a function of the algorithm's step size (c). Results are shown for simulated 2DFT data with peak heating of 25°C and peak attenuation of 0.8, at 78 Hz pixel bandwidth. c can be tuned to balance temperature reconstruction error with the number of algorithm iterations, but the algorithm is robust to its tuning between approximately $c = 10^{-3}$ to $c = 10^{-5}$.

and 0.89 for EPI. Figures 5.5b and 5.6b show magnitude images that were reconstructed using the CS-corrected PRF-shift maps only, and the CS-corrected PRF-shift maps and attenuation estimates. The images are zoomed in to a region around the hot spot. Percent standard deviation of the reconstructed magnitude images without correction, with CS-only correction and with joint CS and attenuation correction in a region around the hotspot was 14.16%, 13.22%, and 2.65% for 2DFT and 13.51%, 11.52%, and 4.67% for EPI scans, respectively. Reconstructing the images with both the PRF-shift maps and the estimated magnitude attenuation maps deblurred the images and filled in the signal hole, resulting in a flat magnitude image as expected if there were no heating.

CS distortions become more severe as pixel bandwidth decreases, as reflected in temperature profiles across the hot spot in Figs 5.5c and 5.6c, and in the higher measurements of hot spot asymmetry shown in Figs 5.5d and 5.6d. CS correction mostly eliminates this asymmetry, resulting in measurements that are approximately constant across bandwidths.

CS-corrected temperature maps had lower asymmetry than uncorrected maps at each bandwidth, with a factor of 3 (EPI) to 4 (2DFT) times lower asymmetry at the lowest bandwidth. To illustrate how much of the measured asymmetries can be attributed to noise, the bar charts in Figs 5.5d and 5.6d also show asymmetry in the same regions prior to heating, which increases with increasing bandwidth due to decreasing SNR. The differences between the noise and CS-corrected asymmetries may be due to unaccounted-for background static field inhomogeneities.

5.5.3 In vivo MRgFUS ablations

In vivo results are shown in Figs 5.7-5.9. Uncorrected and CS-corrected temperature maps had similar temperature amplitudes but the uncorrected hot spots were shifted to the right by approximately 1 mm along the distortion dimension in brain (Fig 5.7), leg (Fig 5.8), and uterine fibroid (Fig 5.9). This shift is apparent in the displayed maps of voxel-wise differences in maximum temperature for each temperature time series with and without CS correction. Leg and uterine fibroid temperature maps and differences are shown for representative sonications with high heat. Across voxels, differences in maximum temperature between uncorrected and CS-corrected maps ranged from: -1.4°C to 2.8°C (brain, axial); -1.8°C to 3.0°C (brain, sagittal); -4.0°C to 5.6°C (leg, one sonication); and -3.4°C to 2.4°C (fibroid, one sonication). Peak image magnitude attenuation estimates were: 0.31 (brain, axial); 0.40 (brain, sagittal); 1.75 (leg, one sonication); and 0.46 (fibroid, one sonication). Thermal dose maps over the entire treatment from leg soft tissue tumor and uterine fibroid ablations show that both methods identified a common core of heat with differences along the hot spot boundaries, similar to difference patterns observed in the temperature maps.

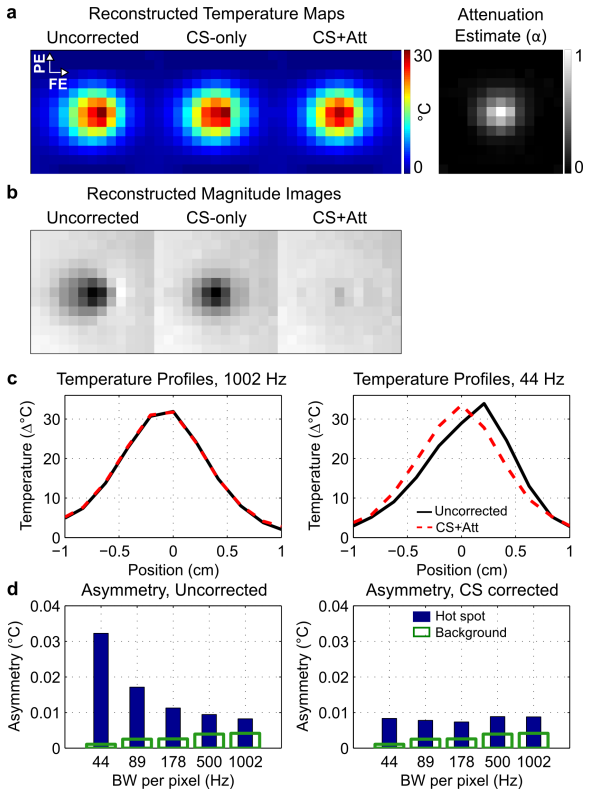

Figure 5.5: 2DFT Phantom experiment results. 44 Hz pixel BW results are shown in (a)–(b). (a) Temperature elevation and attenuation map (α) estimates at peak heat. (b) Magnitude images at peak heat reconstructed with no distortion correction, CS distortion correction only, and both attenuation and CS distortion correction. (c) Temperature elevation profiles at peak heat for highest (1002 Hz, left) and lowest (44 Hz, right) pixel BW scans. (d) Hot spot asymmetry of uncorrected (left) and CS distortion-corrected (right) temperature maps interpolated to a 10$\times$ finer grid, as a function of readout bandwidth. At low bandwidths, uncorrected temperature maps have distorted profiles through the hot spot and higher asymmetry, while corrected profiles have more uniform asymmetry. Background asymmetry due to noise is also shown for each bandwidth.

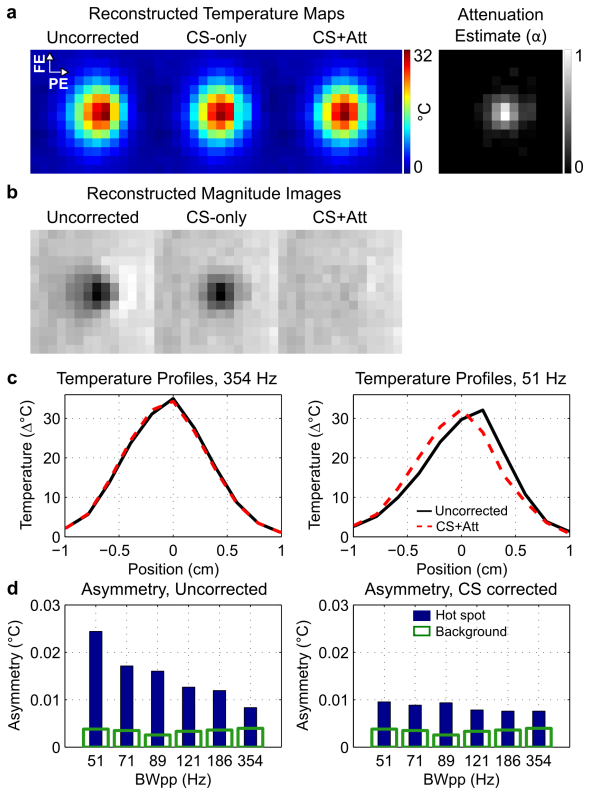

Figure 5.6: EPI Phantom experiment results. 51 Hz pixel BW results are shown in (a)-(b). (a) Temperature elevation and attenuation map (α) estimates at peak heat. (b) Magnitude images at peak heat reconstructed with no distortion correction, CS distortion correction only, and both attenuation and CS distortion correction. (c) Temperature elevation profiles at peak heat for highest (354 Hz, left) and lowest (51 Hz, right) pixel BW scans. (d) Hot spot asymmetry of uncorrected (left) and CS distortion-corrected (right) temperature maps interpolated to a 10$\times$ finer grid, as a function of readout bandwidth. At low bandwidths, uncorrected temperature maps have distorted profiles through the hot spot and higher asymmetry, while corrected profiles have more uniform asymmetry. Background asymmetry due to noise is also shown for each bandwidth.

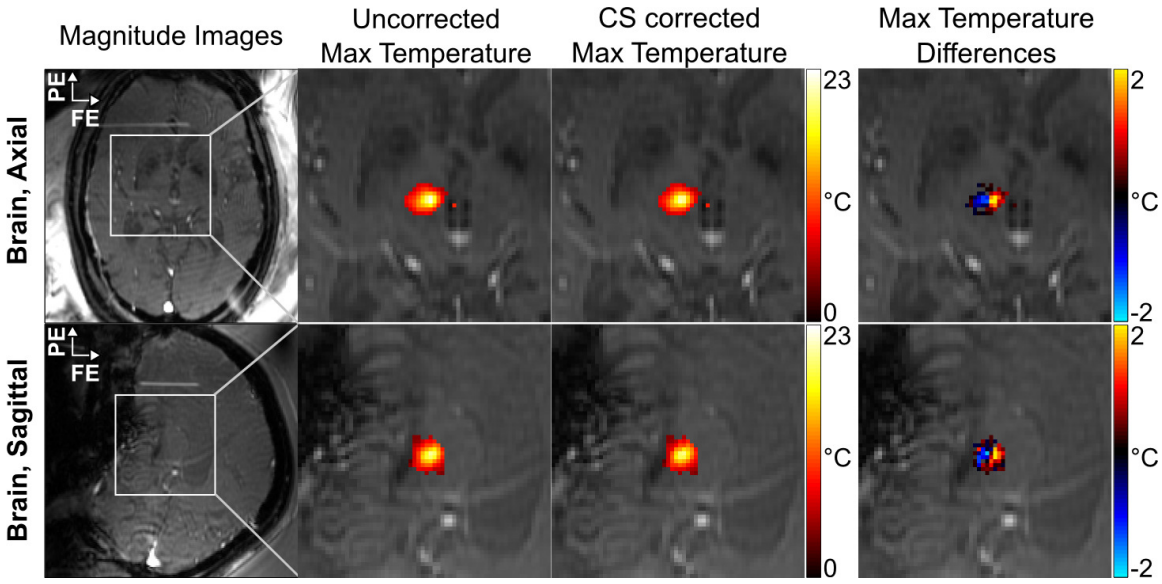

Figure 5.7: Brain sonication results in axial (top row) and sagittal (bottom row) slice orientations. Magnitude images are shown on the left with boxes around the focal region. Maximum temperature elevation map overlays are shown in the middle two columns before and after CS distortion correction. The maximum temperature map differences above 0.1°C between uncorrected and corrected maps in heated voxels are shown on the right.

5.5.4 Computation times

For each dataset, Table 5.1 lists computation times for the C-based MEX implementation of the algorithm without parallelization, averaged over 10 repetitions for a single temperature map at peak heat. Times were measured using MATLAB's `tic` and `toc` functions, on a MacBook Pro computer (Apple Computer, Cupertino, CA, USA) with a 3 GHz Intel Core i7 CPU and 16 GB RAM. For the phantom data, processing times were measured at the lowest readout bandwidth where CS distortions were the largest. The CS correction algorithm required the most time (370 ms) for leg soft tissue tumor temperature maps, in which the temperature elevation and the total number of voxels processed and algorithm iterations were greatest. The sagittal brain map had the next-highest computation time of 9.0 ms. Averaged across datasets, the compute time per voxel was 0.83 ms.

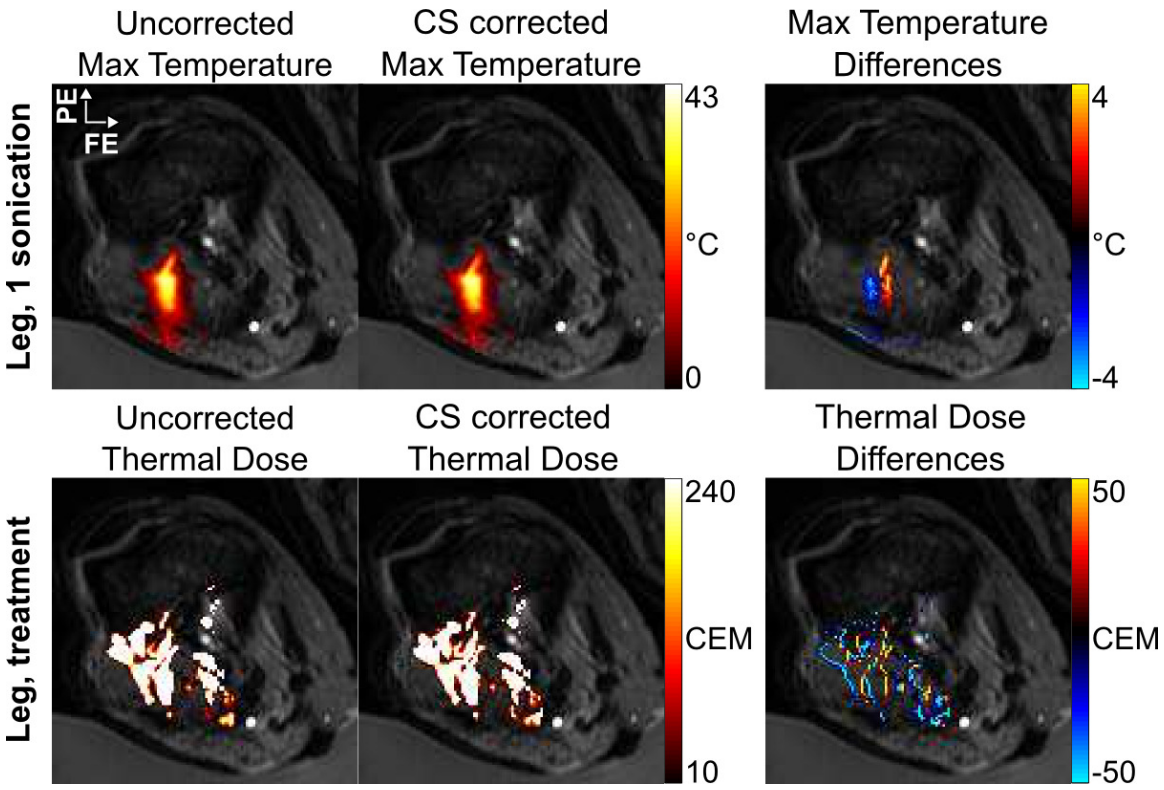

Figure 5.8: Results from leg soft tissue tumor sonications. Top row: Maximum temperature elevation maps from one sonication before (left) and after CS correction (middle) and differences of 1°C and greater between corrected and uncorrected maps in heated voxels (right). Bottom row: Thermal dose maps over entire treatment calculated from uncorrected (left) and CS corrected temperature maps (middle) and thermal dose differences greater than 2 CEM between corrected and uncorrected estimates (right).

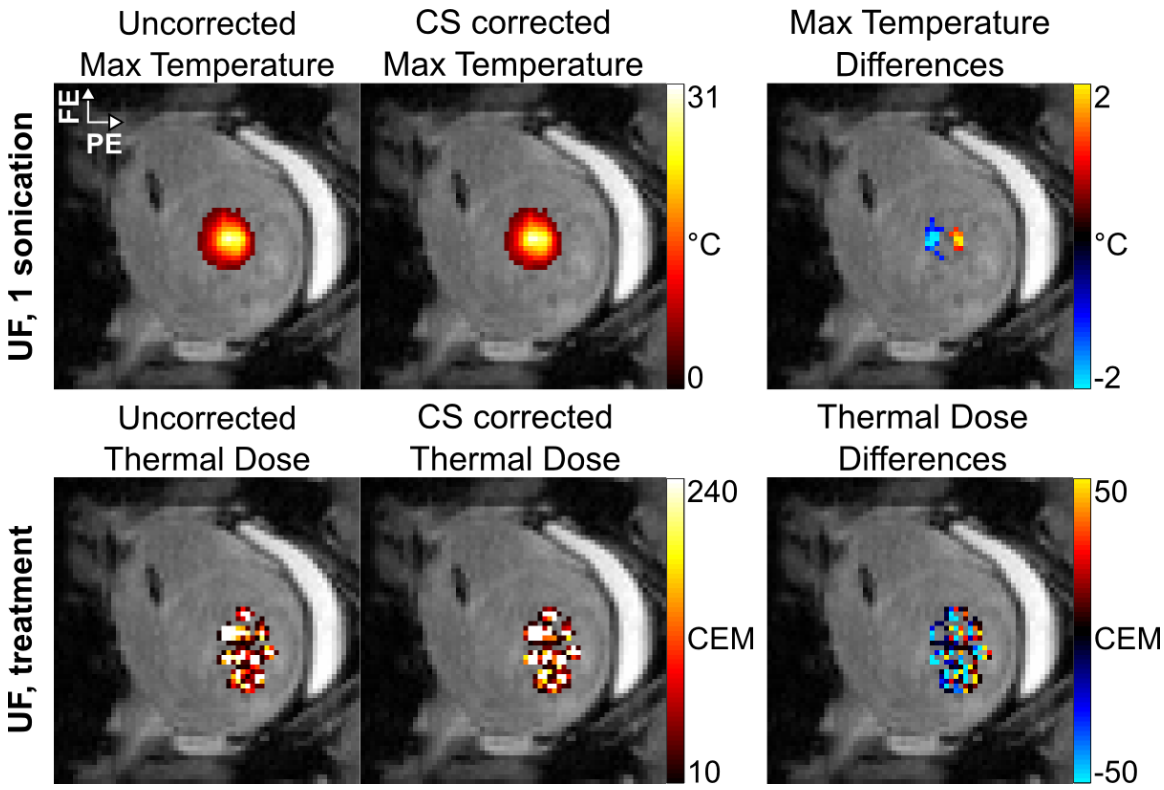

Figure 5.9: Results from uterine fibroid (UF) sonications. Top row: Maximum temperature elevation maps from one sonication before (left) and after CS correction (middle) and differences of 1°C and greater between corrected and uncorrected maps in heated voxels (right). Bottom row: Thermal dose maps over entire treatment calculated from uncorrected (left) and CS corrected temperature maps (middle) and thermal dose differences greater than 2 CEM between corrected and uncorrected estimates (right).

Dataset	Voxels Corrected	Total Iterations	Compute Time
Phantom, 2DFT	132	166	7.1 ms
Phantom, EPI	159	138	6.6 ms
Brain, Axial	91	86	8.2 ms
Brain, Sagittal	101	125	9.0 ms
Leg	724	2018	370 ms
Uterine Fibroid	92	111	3.9 ms

Table 5.1: For each data set, the total number of voxels, total iterations, and total compute time to process a temperature map at peak heat are listed. Compute times were measured using the C-based MEX version of the algorithm, on a MacBook Pro computer with a 3 GHz Intel Core i7 CPU and 16 GB RAM. No parallelization was used.

5.6 Discussion

5.6.1 Summary of main results

Simulation and experimental results demonstrated that chemical shift distortions in PRF temperature maps can be corrected using an algorithm that updates the maps to maximize correspondence between collected k-space data and a model for that data that accounts for heat-induced off-resonance phase accrual during the readout. In in vivo applications using pixel BWs of 44 and 79 Hz, the locations of peak heating shifted by approximately 1 mm after CS correction, and differences between uncorrected and corrected temperature maps were on the order of a few degrees Celsius. Uncorrected and corrected thermal dose maps mostly differed at the hot spot boundaries. Phantom and simulation results showed that corrections were most complete when the algorithm simultaneously estimated heating-induced frequency shifts and an image magnitude attenuation map, since this enabled it to tease apart the potentially confounding effects of changing T_1 and T_2^* and PRF with heat, both of which result in image magnitude variations. The phantom and simulation results also showed that correcting CS distortions is most important for long 2DFT and EPI readouts with low frequency bandwidths in one dimension, where more cycles of phase

accrue across k-space due to off-resonance, resulting in larger signal displacements in the reconstructed image and temperature map.

5.6.2 Implications for clinical treatments

Small errors in temperature can result in under- or over-treatment, and thereby adversely impact safety and efficacy, particularly in brain treatments where a narrow range of maximum temperatures is desired (typically 55–60°C) [43, 44]. Positioning errors of the hot spot can also be harmful in many in vivo applications, particularly when it is desirable to avoid exposure to nearby structures such as critical areas in the brain, the bowel, peripheral nerves, or blood vessels. These errors can be corrected by the algorithm, and its short compute times further support that it could be widely implemented to obtain the most accurate possible temperature maps in real-time. Overall, the ability to correct CS distortions will improve dosimetry, potentially resulting in more consistent procedure outcomes, and will contribute to enabling MRgFUS procedures that demand narrow treatment margins or temperature monitoring with fine spatial resolution and/or large volume coverage.

This work also demonstrated that CS distortions are negligible if the pixel BW is sufficiently high. While a number of factors including image matrix size, sequence timing, and required temperature SNR dictate the pixel BWs that are used for temperature monitoring of ablations, based on our results we can make some statement about what pixel bandwidth will result in negligible chemical shift artifact at high heat. Specifically, our 2DFT and EPI phantom experiment results suggest that heat-induced errors may be considered negligible for a hot spot asymmetry of 0.01°C, which in our 3T experiments was reached at a pixel BW of approximately 400 Hz for a hot spot with a 30°C peak temperature rise.

5.6.3 Practical considerations

Since the method is implemented as a post-processing step, it is compatible with temperature reconstruction methods that output an estimate of the drift-compensated baseline

image, along with the initial temperature map. Compatible thermometry approaches include baseline subtraction [128], as well as multibaseline/atlas-based subtraction [129, 181, 182], and hybrid referenceless and multibaseline subtraction [106] which can compensate motion. The method is not compatible with referenceless thermometry alone, since it does not produce a baseline image estimate [130]. Further work is needed to characterize the method's sensitivity to degraded baseline image estimates resulting from motion.

In its current embodiment, the CS correction algorithm requires the user to select the gradient descent step size (c). c should be chosen small enough to not overshoot the optimal solution, but large enough to achieve rapid improvement between iterations. The results of Fig. 4 showed that for the simulations, the algorithm reached a low error with relatively few iterations for step sizes varying over more than an order of magnitude. The phantom and in vivo results further demonstrated that the step size could be tuned in relatively coarse increments of powers of 10, and that the same step size could be used for all temperature map corrections in a given application. However, more advanced techniques that adapt the effective step size over iterations such as the Levenberg-Marquardt method may provide still more robust performance, and will be a focus of future development.

Another user-defined algorithm parameter is the phase threshold used to define the mask of voxels with significant heating. In practice, this threshold could be set intuitively based on the maximum pixel shift the user deems acceptable in the hot spot for a given target temperature rise, or based on the intended sonication region identified in the treatment planning stage.

5.6.4 Future developments and extensions

The proposed method corrects an intrinsic source of error in PRF temperature mapping that results from the heating itself. In addition to intrinsic sources of error it is well known that EPI temperature acquisitions suffer off-resonance distortions that are not related to heating from sources such as static field inhomogeneities, tissue magnetic susceptibil-

ity variations, and eddy currents. Much development has focused on correcting EPI images for these sources of error, including some methods specific to interventional imaging [183]. Those methods are related to but separate from the heat-induced distortion correction presented here. For example, our algorithm is related to methods for field map-based EPI image corrections [184], but in the present application the field map is replaced by the heating-induced frequency change map, and is estimated from the image itself, rather than from a pre-scan. Future development may focus on the integration of heat-induced CS distortion correction with corrections for other EPI distortions.

Since the proposed algorithm is implemented as a post-processing step, it could also be combined with corrections for other intrinsic sources of temperature error related to heating itself. For example, changes in tissue magnetic susceptibility with heating also cause resonance frequency offsets in and around the hot spot. Thus, a reasonable strategy to reconstruct temperature maps that are corrected for both CS distortions and susceptibility change-induced errors would be to first perform CS distortion correction, which would compensate temperature map distortions due to both effects, and then perform a susceptibility correction using a method such as Ref. [179].

To correct a large number of heated voxels within real-time constraints, such as for a multi-slice sequence or when significant near-field heating appears, CS correction can be computationally parallelized across both k-space lines and slices. Although, in the case of monitoring near-field heating, fine temperature accuracy may not be required since this information is typically used not for dosimetry but to determine whether or not to stop treatment, and to monitor the tissue as it cools back down to a safe level. The best approach to accounting for near-field heating may instead be to exclude voxels outside the planned treatment zone from CS correction and adjust the maximum safe near-field heating threshold downward to account for possible additional errors due to chemical shift. We have previously shown that CS distortion correction can also be developed for non-Cartesian PRF acquisitions such as spiral, though the computation times for those corrections are currently

on the order of minutes, making them incompatible with online use [165]. Finally, we note that the attenuation maps estimated by the proposed algorithm may be useful for hybrid T_1/PRF-based temperature acquisitions [74].

5.7 Conclusions

An algorithm to correct CS distortions in PRF temperature maps was presented and validated in simulations, gel phantom MRgFUS experiments, and brain, soft tissue tumor and uterine fibroid MRgFUS patient treatment data. The algorithm is compatible with the Cartesian 2DFT and EPI acquisitions that are currently in widespread use for PRF acquisitions during MRgFUS procedures. Simulations and phantom experiments showed that the algorithm produced temperature maps that were more accurate and symmetric, while patient results showed that the algorithm produced temperature maps that were shifted on the order of 1 mm in the low-bandwidth dimension, and differed from the uncorrected maps by up to 5.6°C. Small errors in temperature were also found to propagate into thermal dose inaccuracies. Therefore, compensating for these errors can have a positive impact on clinical outcomes due to more accurate dosimetry. Computation times indicated compatibility with online use.

5.8 Acknowledgements

This work was supported by NCI 1R25CA136440-01, NIBIB T32EB014841, the Focused Ultrasound Foundation, the Howard Hughes Medical Institute / Vanderbilt University Medical Center Certificate Program in Molecular Medicine, and P01 CA159992. The authors would like to thank Xue Feng, Sam Fielden, and Craig Meyer for help implementing the algorithm in RTHawk.

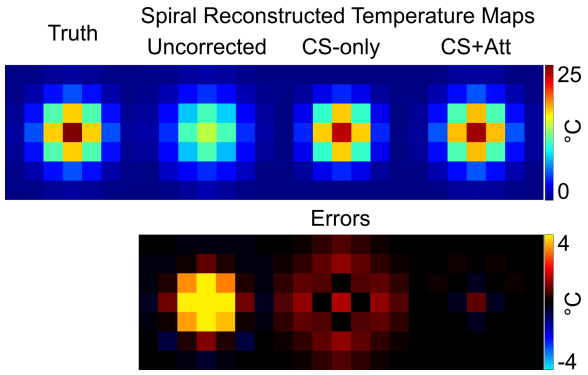

Figure 5.10: Spiral simulation temperature map reconstruction. Zoomed-in comparison between the true hot spot at peak heat (24.5°C, peak image magnitude attenuation of 0.8, 1-shot), and reconstructed temperature maps. Difference images show error for maps reconstructed without and with CS distortion correction, and without and with image magnitude attenuation estimation.

5.9 Appendix

5.9.1 Application to non-Cartesian data

The k-space signal model with heat given in Eq. 5.1 can be fit to data acquired on any k-space trajectory using the algorithm described in Ch. 3. The same phantom simulation with focal heating and heat-induced image magnitude attenuation as described in Section 5.4.2 and illustrated in Fig 5.2a was performed. Reconstructed temperature maps for the single-shot spiral simulation with peak heat and peak image attenuation are shown in Fig 5.10. Without CS correction, temperature reconstructions underestimate the true heating map. Temperature RMSE is shown in Fig 5.11. CS-only reconstructions may be improved with increased regularization. However, these reconstructions have highest error in simulations with low heating and high peak attenuation, which are unlikely situations to occur in practice since the T_1-induced signal loss is a function of temperature increase. Simulation results show that temperature maps can be reconstructed from spiral data with low error by accounting for heat-induced CS and image magnitude attenuation effects.

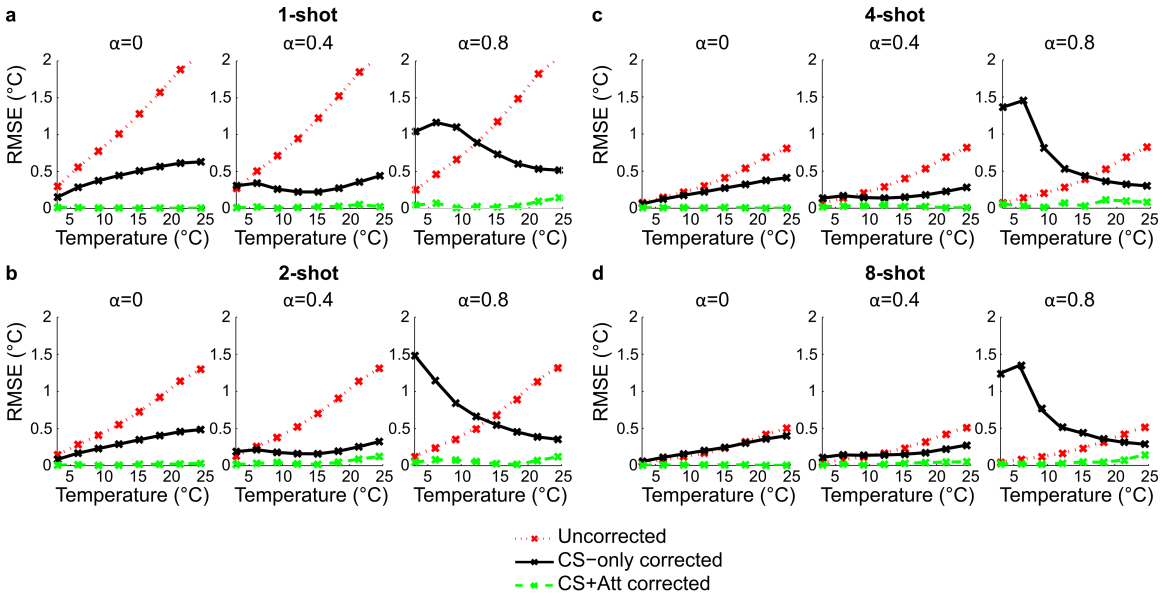

Figure 5.11: Spiral simulation results. Temperature root-mean-square-error (RMSE) over hot spots of different peak temperatures at three peak attenuation factors (α) with (a) 1, (b) 2, (c) 4, and (d) 8 shot spiral readouts. Accounting for CS and image attenuation in the reconstruction results in the lowest temperature error.

Chapter 6

Conclusions

6.1 Contributions of this work

Improvements in MR temperature map reconstruction have been presented for accelerated imaging during MRgFUS (Chapter 3) and transcranial MRgFUS using a spatially-segmented reconstruction (Chapter 4), as well as an online-compatible correction for heat-induced distortion (Chapter 5). Temperature reconstruction directly from undersampled k-space enabled high acceleration factors without loss of temporal resolution. The spatially-segmented reconstruction translated this method to transcranial applications of MRgFUS, where data undersampling otherwise results in artifacts caused by unpredictable water bath signal changes. A fast correction method for intrinsic off-resonance distortions in thermal applications improved accuracy in temperature maps and reconstructed images, and is compatible with online reconstruction on multiple vendor software platforms. These developments are compatible with Cartesian and non-Cartesian k-space sampling trajectories, with parallel imaging methods, and may be combined with other methods such as temporal regularization approaches. They are also applicable to the reconstruction of temperature changes from sources of focal heating other than MRgFUS.

6.2 Future work

6.2.1 Undersampled baseline image reconstruction

We have demonstrated temperature map reconstruction with low error from undersampled k-space data using a model which incorporates fully sampled baseline images. To extend current temperature monitoring from single slice to volumetric scans in the brain, baseline images across the volume should be sampled at sufficiently high temporal resolu-

tion so as not to be corrupted by physiological artifacts such as pulsatile motion [185, 186]. Blood pulsation results in propagating motion across the brain as well as uniform bulk motion, and causes varying and location-dependent signal intensity changes across the cardiac cycle [187, 82]. However, with limited receive coils for parallel imaging acceleration, full image sampling will not be fast enough to resolve physiologically-induced signal changes.

A potential solution is to estimate fully-sampled baseline images from a series of undersampled scans which sample locations in k-space out of sync with physiological cycles. Then, rather than using a weighted combination of acquired fully-sampled baseline images as described in Ch. 3, a matrix of k-space samples across time could be used to estimate the baseline at given snapshot in time. A low rank and sparse matrix formulation has been proposed for reconstructing undersampled time series data [188]. This approach determines low rank and sparse components of the data matrix across time. Incoherent k-space sampling of each component over time, and incoherence between components, allows reconstruction of dynamic data in a compressed sensing framework. The method has been demonstrated in cardiac data, where the low-rank component captures slowly changing but correlated background features between image frames and the sparse component captures dynamically changing features from heart motion. Undersampled k-space data of the brain may also be resolvable using this technique, with fast enough data sampling to overcome inherent motion artifacts in volumetric baseline acquisitions.

6.2.2 Dictionary learning methods for modeling signal in the water bath

Water motion in the bath between the patient's head and the transducer in transcranial MRgFUS causes large and unpredictable signal changes in dynamic images that are difficult to model mathematically. However, it may be possible to use a learning algorithm to train a dictionary based on previous data to improve reconstruction of undersampled dynamic water bath images [189]. In this approach, the dictionary would be used to create a specific sparsifying transform for the water bath signal. With enough training data, the

dictionary can be used to create a sparse representation of the water bath signal. A customized sparsity representation may improve characterization of the water bath signal, and potentially enable undersampled image reconstruction with higher acceleration factors in the water bath. Low temperature error in the brain has been demonstrated using the k-space hybrid model (Fig 3.6), suggesting that high acceleration may be achieved in the segmented brain and water bath reconstruction model as long as the water bath image reconstruction error remains low.

6.2.3 Temperature monitoring in adipose tissue

Heating in adipose tissue is usually ignored in MRgFUS thermometry, leading to only partial measurement of treatment effects in the body. Combined PRF and T_1-based temperature mapping has been proposed for concurrent monitoring of aqueous and adipose tissue heating [120, 190, 74, 127]. In these approaches, both PRF and T_1-sensitive measurements are collected during the pulse sequence. However, data undersampling methods for image acceleration have not been applied to PRF/T_1 thermometry and can potentially increase the volumetric coverage that can be achieved.

An extension of the current work is to formulate a k-space signal model to characterize temperature changes across both water and fat tissues. This could be achieved by incorporating water and fat image separation, accounting for susceptibility changes from lipid heating, and expanding temperature map reconstruction into two stages. Fully-sampled baseline images are important for constraining temperature map reconstruction from highly undersampled k-space data. Correct assessment of voxel composition will also be important, and can be achieved by leveraging advanced algorithms for separating images into water and fat components on a voxel-by-voxel basis [191, 192, 193, 194, 195, 196, 197, 198]. Reduced temperature erros have been demonstrated in hybrid multibaseline and referenceless temperature reconstruction when background phase and PRF shift parameters were estimated jointly from water and fat signals [124, 125].

Recently, hybrid PRF- and T_1-sensitive sequences with multiple echoes and flip angles have been proposed for simultaneous water and fat temperature imaging [126, 74] A spatial segmentation approach could be applied to the temperature change map reconstruction such that the PRF shift model is fit in water voxels and the T_1 model is fit in fat voxels. Since voxels will contain a mixture of both water and fat, temperature estimates in mixed voxels could be weighted by the fraction of water or fat composition. T_1 temperature change measurements can be converted to phase change by a linear scaling factor, and combined with PRF phase shift maps to generate a complete heat-induced phase map across the image.

6.2.4 MR Fingerprinting

MR fingerprinting is another technique that could be applied to classify tissue heating [199]. Because MR parameters are temperature sensitive, variations in tissue relaxation rates could be used to separate heated from non-heated tissue. Imaging over a range of TR, TE, and flip angle acquisition parameters to capture signal variations due to heating, in comparision with expected signal evolution profiles in tissue, could provide a fast treatment monitoring technique. Fingerprinting could also be applicable to joint water-fat thermometry in tissues with mixed composition.

BIBLIOGRAPHY

[1] Huber PE, Jenne JW, Rastert R, Simiantonakis I, Sinn HP, Strittmatter HJ, von Fournier D, Wannenmacher MF, Debus J. A new noninvasive approach in breast cancer therapy using magnetic resonance imaging-guided focused ultrasound surgery. Cancer Res 2001;61:8441–8447.

[2] Hynynen K, Pomeroy O, Smith DN, Huber PE, McDannold NJ, Kettenbach J, Baum J, Singer S, Jolesz FA. MR Imaging-guided focused ultrasound surgery of fibroadenomas in the breast: A feasibility study1. Radiology 2001;219:176–185.

[3] Tempany CMC, Stewart EA, McDannold N, Quade BJ, Jolesz F, Hynynen K. MR Imaging-guided Focused Ultrasound Surgery of Uterine Leiomyomas: A Feasibility Study. Radiology 2003;226:897–905.

[4] McDannold NJ, Clement GT, Black P, Jolesz FA, Hynynen K. Transcranial magnetic resonance imaging-guided focused ultrasound surgery of brain tumors: Initial findings in 3 patients. Neurosurgery 2010;66:323–332.

[5] Catane R, Beck A, Inbar Y, Rabin T, Shabshin N, Hengst S, Pfeffer RM, Hanannel A, Dogadkin O, Liberman B. MR-guided focused ultrasound surgery (MRgFUS) for the palliation of pain in patients with bone metastases—preliminary clinical experience. Ann Oncol 2007;18:163–167.

[6] Liberman B, Gianfelice D, Inbar Y, Beck A, Rabin T, Shabshin N, Chander G, Hengst S, Pfeffer R, Chechick A. Pain palliation in patients with bone metastases using MR-guided focused ultrasound surgery: a multicenter study. Ann Surg Oncol 2009;16:140–146.

[7] Martin E, Jeanmonod D, Morel A, Zadicario E, Werner B. High-intensity focused ultrasound for noninvasive functional neurosurgery. Ann Neurol 2009;66:858–861.

[8] Sunnybrook Health Sciences Centre. World first: Blood brain barrier opened non-invasively to deliver chemotherapy. http://sunnybrook.ca/media/item.asp?i=1351, 2015.

[9] Madio DP, Van Gelderen P, DesPres D, Olson AW, De Zwart JA, Fawcett TW, Holbrook NJ, Mandel M, Moonen CTW. On the Feasibility of MRI-Guided Focused Ultrasound for Local Induction of Gene Expression. J Magn Reson Imaging 1998; 8:101–104.

[10] Jolesz FA, McDannold N. Current status and future potential of MRI-guided focused ultrasound surgery. Journal of Magnetic Resonance Imaging 2008;27:391–399.

[11] Quesson B, de Zwart J, Moonen CTW. Magnetic resonance temperature imaging for guidance of thermotherapy. Journal of Magnetic Resonance Imaging 2000;12:525–533.

[12] Kennedy JE, Ter Haar GR, Cranston D. High intensity focused ultrasound: surgery of the future? Br J Radiol 2003;76:590–599.

[13] Lynn JG, Zwemer RL, Chick AJ, Miller AE. A new method for the generation and use of focused ultrasound in experimental biology. The journal of general physiology 1942;26:179–193.

[14] Fan X, Hynynen K. Control of the necrosed tissue volume during noninvasive ultrasound surgery using a 16-element phased array. Medical Physics 1995;22:297–306.

[15] Wan H, VanBaren P, Ebbini ES, Cain CA. Ultrasound surgery: comparison of strategies using phased array systems. IEEE Transactions on Ultrasonics, Ferroelectrics and Frequency Control 1996;43:1085–1098.

[16] Hynynen K, Colucci V, Chung AH, Jolesz FA. Noninvasive arterial occlusion us-

ing MRI-guided focused ultrasound. Ultrasound in Medicine and Biology 1996; 22:1071–1077.

[17] Daum DR, Smith NB, King R, Hynynen K. In vivo demonstration of noninvasive thermal surgery of the liver and kidney using an ultrasonic phased array. Ultrasound in Medicine and Biology 1999;25:1087–1098.

[18] Wu F, Chen WZ, Bai J, Zou JZ, Wang ZL, Zhu H, Wang ZB. Pathological changes in human malignant carcinoma treated with high-intensity focused ultrasound. Ultrasound in Medicine and Biology 2001;27:1099–1106.

[19] Lynn JG, Putnam TJ. Histology of cerebral lesions produced by focused ultrasound. The American journal of pathology 1944;20:637–649.

[20] Moonen CT, Quesson B, Salomir R, Vimeux FC, de Zwart J, Van Vaals JJ, Grenier N, Palussiere J. Thermal therapies in interventional MR imaging. Focused ultrasound. Neuroimaging Clin N Am 2001;11:737–747.

[21] Jolesz FA. MRI-Guided Focused Ultrasound Surgery. Annual Review of Medicine 2009;60:417–430.

[22] Al-Bataineh O, Jenne J, Huber P. Clinical and future applications of high intensity focused ultrasound in cancer. Cancer Treatment Reviews 2012;38:346–353.

[23] Fry WJ, Mosberg WH Jr, Barnard JW, Fry FJ. Production of focal destructive lesions in the central nervous system with ultrasound. Journal of neurosurgery 1954;11:471–478.

[24] Fry WJ, Fry FJ. Fundamental neurological research and human neurosurgery using intense ultrasound. Medical Electronics, IRE Transactions on 1960;pp. 166–181.

[25] Jagannathan J, Sanghvi NT, Crum LA, Yen CP, Medel R, Dumont AS, Sheehan JP, Steiner L, Jolesz F, Kassell NF. High-intensity focused ultrasound surgery of

the brain: Part 1–A historical perspective with modern applications. Neurosurgery 2009;64:201–211.

[26] Denis de Senneville B, Quesson B, Moonen CT. Magnetic resonance temperature imaging. International Journal of Hyperthermia 2005;21:515–531.

[27] Hynynen K, Freund WR, Cline HE, Chung AH, Watkins RD, Vetro JP, Jolesz FA. A clinical, noninvasive, MR imaging-monitored ultrasound surgery method. Radiographics 1996;16:185–195.

[28] Hynynen K, Vykhodtseva NI, Chung AH, Sorrentino V, Colucci V, Jolesz FA. Thermal effects of focused ultrasound on the brain: determination with MR imaging. Radiology 1997;204:247–253.

[29] Fry WJ, Barnard JW, Fry FJ, Brennan JF. Ultrasonically produced localized selective lesions in the central nervous system. American Journal of Physical Medicine & Rehabilitation 1955;34:413–423.

[30] Fry F, Ades H, Fry W. Production of reversible changes in the central nervous system by ultrasound. Science 1958;127:83–84.

[31] Ballantine Jr H, Bell E, Manlapaz J. Progress and problems in the neurological applications of focused ultrasound*. Journal of neurosurgery 1960;17:858–876.

[32] FRY FJ. Precision high intensity focusing ultrasonic machines for surgery. American Journal of Physical Medicine & Rehabilitation 1958;37:152–156.

[33] Fry W, Fry F. Fundamental neurological research and human neurosurgery using intense ultrasound. Medical Electronics, IRE Transactions on 1960;pp. 166–181.

[34] Fry F, Kossoff G, Eggleton R, Dunn F. Threshold ultrasonic dosages for structural changes in the mammalian brain. the Journal of the Acoustical Society of America 1970;48:1413–1417.

[35] Fry W, Meyers R. Ultrasonic method of modifying brain structures. Stereotactic and Functional Neurosurgery 1962;22:315–327.

[36] Jolesz FA, Jakab PD. Acoustic pressure wave generation within an MR imaging system: potential medical applications. Journal of Magnetic Resonance Imaging 1991;1:609–613.

[37] Cline HE, Schenck JF, Hynynen K, Watkins RD, Souza SP, Jolesz FA. MR-guided focused ultrasound surgery. Journal of computer assisted tomography 1992;16:956–965.

[38] Hynynen K, Darkazanli A, Unger E, Schenck J. MRI-guided noninvasive ultrasound surgery. Medical physics 1993;20:107–115.

[39] Alongi F, Russo G, Spinelli A, Borasi G, Scorsetti M, Gilardi MC, Messa C. Can magnetic resonance image-guided focused ultrasound surgery replace local oncology treatments? a review. Tumori 2010;97:259–264.

[40] Furusawa H, Namba K, Thomsen S, Akiyama F, Bendet A, Tanaka C, Yasuda Y, Nakahara H. Magnetic resonance–guided focused ultrasound surgery of breast cancer: reliability and effectiveness. Journal of the American College of Surgeons 2006;203:54–63.

[41] Stewart EA, Gostout B, Rabinovici J, Kim HS, Regan L, Tempany CM, et al. Sustained relief of leiomyoma symptoms by using focused ultrasound surgery. Obstetrics & Gynecology 2007;110:279–287.

[42] Wang TR, Dallapiazza R, Elias WJ. Neurological applications of transcranial high intensity focused ultrasound. International Journal of Hyperthermia 2015;31:285–291.

[43] Jeanmonod D, Werner B, Morel A, Michels L, Zadicario E, Schiff G, Martin E. Transcranial magnetic resonance imaging–guided focused ultrasound: Noninvasive central lateral thalamotomy for chronic neuropathic pain. Neurosurg Foc 2012;32:E1.

[44] Elias WJ, Huss D, Voss T, Loomba J, Khaled M, Zadicario E, Frysinger RC, Sperling SA, Wylie S, Monteith SJ, Druzgal J, Shah BB, Harrison M, Wintermark M. A Pilot Study of Focused Ultrasound Thalamotomy for Essential Tremor. New Engl J Med 2013;369:640–648.

[45] Chang WS, Jung HH, Kweon EJ, Zadicario E, Rachmilevitch I, Chang JW. Unilateral magnetic resonance guided focused ultrasound thalamotomy for essential tremor: practices and clinicoradiological outcomes. Journal of Neurology, Neurosurgery & Psychiatry 2014;pp. jnnp–2014.

[46] Odéen H, de Bever J, Almquist S, Farrer A, Todd N, Payne A, Snell JW, Christensen DA, Parker DL. Treatment envelope evaluation in transcranial magnetic resonance-guided focused ultrasound utilizing 3D MR thermometry. Journal of therapeutic ultrasound 2014;2:19.

[47] Ghanouni P, Pauly KB, Elias WJ, Henderson J, Sheehan J, Monteith S, Wintermark M. Transcranial MRI-guided focused ultrasound: A review of the technologic and neurologic applications. American Journal of Roentgenology 2015;205:150–159.

[48] Hynynen K, McDannold N, Clement G, Jolesz FA, Zadicario E, Killiany R, Moore T, Rosen D. Pre-clinical testing of a phased array ultrasound system for MRI-guided noninvasive surgery of the brain—a primate study. European journal of radiology 2006;59:149–156.

[49] Coluccia D, Fandino J, Schwyzer L, O'Gorman R, Remonda L, Anon J, Martin E, Werner B. First noninvasive thermal ablation of a brain tumor with MR-guided focused ultrasound. J Neurol Surg A Cent Eur Neurosurg 2014;75:50.

[50] Lipsman N, Schwartz ML, Huang Y, Lee L, Sankar T, Chapman M, Hynynen K, Lozano AM. MR-guided focused ultrasound thalamotomy for essential tremor: a proof-of-concept study. The Lancet Neurology 2013;12:462–468.

[51] Magara A, Bühler R, Moser D, Kowalski M, Pourtehrani P, Jeanmonod D. First experience with MR-guided focused ultrasound in the treatment of parkinson's disease. J Therapeut Ultrasound 2014;2:b74.

[52] Schlesinger I, Eran A, Sinai A, Erikh I, Nassar M, Goldsher D, Zaaroor M. MRI guided focused ultrasound thalamotomy for moderate-to-severe tremor in parkinson's disease. Parkinson's Disease 2015;2015.

[53] Jung H, Kim S, Roh D, Chang J, Chang W, Kweon E, Kim C, Chang J. Bilateral thermal capsulotomy with mr-guided focused ultrasound for patients with treatment-refractory obsessive-compulsive disorder: a proof-of-concept study. Molecular psychiatry 2014;.

[54] Monteith SJ, Kassell NF, Goren O, Harnof S. Transcranial MR-guided focused ultrasound sonothrombolysis in the treatment of intracerebral hemorrhage. Neurosurgical focus 2013;34:E14.

[55] Watkins RD, Bitton R, Butts Pauly K. Integration of an inductive driven axially split quadrature volume coil with MRgFUS system for treatment of human brain. In Proceedings 22nd Scientific Meeting, International Society for Magnetic Resonance in Medicine, Milan. 2014; p. 2330.

[56] Fennessy FM, Tempany CM. A review of magnetic resonance imaging-guided focused ultrasound surgery of uterine fibroids. Topics in Magnetic Resonance Imaging 2006;17:173–179.

[57] Clement G, Hynynen K. Correlation of ultrasound phase with physical skull properties. Ultrasound in medicine & biology 2002;28:617–624.

[58] Martin E, Werner B. Focused ultrasound surgery of the brain. Current Radiology Reports 2013;1:126–135.

[59] Köhler MO, Mougenot C, Quesson B, Enholm J, Le Bail B, Laurent C, Moonen CTW, Ehnholm GJ. Volumetric HIFU ablation under 3D guidance of rapid MRI thermometry. Med Phys 2009;36:3521–3535.

[60] Clarke R, Ter Haar G. Temperature rise recorded during lesion formation by high-intensity focused ultrasound. Ultrasound in medicine & biology 1997;23:299–306.

[61] Heisterkamp J, van Hillegersberg R, IJzermans JN. Critical temperature and heating time for coagulation damage: implications for interstitial laser coagulation (ilc) of tumors. Lasers in surgery and medicine 1999;25:257–262.

[62] ter Haar G, Sinnett D, Rivens I. High intensity focused ultrasound-a surgical technique for the treatment of discrete liver tumours. Physics in medicine and biology 1989;34:1743.

[63] Moser D, Zadicario E, Schiff G, Jeanmonod D. MR-guided focused ultrasound technique in functional neurosurgery: targeting accuracy. J Ther Ultrasound 2013;1.

[64] Malcolm A, Ter Haar G. Ablation of tissue volumes using high intensity focused ultrasound. Ultrasound in medicine & biology 1996;22:659–669.

[65] Sapareto SA, Dewey WC. Thermal dose determination in cancer therapy. International Journal of Radiation Oncology* Biology* Physics 1984;10:787–800.

[66] Pauly KB, Diederich CJ, Rieke V, Bouley D, Chen J, Nau WH, Ross AB, Kinsey AM, Sommer G. Magnetic resonance-guided high-intensity ultrasound ablation of the prostate. Topics in Magnetic Resonance Imaging 2006;17:195–207.

[67] Hynynen K, DeYoung D. Temperature elevation at muscle-bone interface during

scanned, focused ultrasound hyperthermia. International journal of hyperthermia 1988;4:267–279.

[68] Wu F, Wang ZB, Chen WZ, Wang W, Gui Y, Zhang M, Zheng G, Zhou Y, Xu G, Li M, et al. Extracorporeal high intensity focused ultrasound ablation in the treatment of 1038 patients with solid carcinomas in china: an overview. Ultrasonics sonochemistry 2004;11:149–154.

[69] Jung SE, Cho SH, Jang JH, Han JY. High-intensity focused ultrasound ablation in hepatic and pancreatic cancer: complications. Abdominal Imaging 2011;36:185–195.

[70] Hynynen K. Mri-guided focused ultrasound treatments. Ultrasonics 2010;50:221–229.

[71] Rieke V, Pauly KB. MR thermometry. J Magn Reson Imaging 2008;27:376–390.

[72] Mougenot C, Kohler MO, Enholm J, Quesson B, Moonen C. Quantification of near-field heating during volumetric MR-HIFU ablation. Med Phys 2011;38:272–282.

[73] Hynynen K. Mrighifu: A tool for image-guided therapeutics. Journal of Magnetic Resonance Imaging 2011;34:482–493.

[74] Todd N, Diakite M, Payne A, Parker DL. Hybrid proton resonance frequency/T1 technique for simultaneous temperature monitoring in adipose and aqueous tissues. Magn Reson Med 2013;69:62–70.

[75] de Senneville BD, Mougenot C, Quesson B, Dragonu I, Grenier N, Moonen CTW. MR thermometry for monitoring tumor ablation. Eur Radiol 2007;17:2401–2410.

[76] Todd N, Payne A, Parker DL. Model predictive filtering for improved temporal resolution in MRI temperature imaging. Magn Reson Med 2010;63:1269–1279.

[77] Roujol S, Ries M, Quesson B, Moonen CTW, Denis de Senneville B. Real-time MR-thermometry and dosimetry for interventional guidance on abdominal organs. Magn Reson Med 2010;63:1080–1087.

[78] Holbrook AB, Santos JM, Kaye E, Rieke V, Pauly KB. Real-time MR thermometry for monitoring HIFU ablations of the liver. Magnetic Resonance in Medicine 2010; 63:365–373.

[79] Mei CS, Panych LP, Yuan J, McDannold NJ, Treat LH, Jing Y, Madore B. Combining two-dimensional spatially selective RF excitation, parallel imaging, and UNFOLD for accelerated MR thermometry imaging. Magn Reson Med 2011;66:112–122.

[80] Denis de Senneville B, Roujol S, Hey S, Moonen C, Ries M. Extended Kalman Filtering for Continuous Volumetric MR-Temperature Imaging. IEEE Transactions on Medical Imaging 2013;32:711–718.

[81] Chaplin VL, Gaur P, Dayton P, Arena C, Grissom WA, Caskey CF. Methods to Accelerate Thermal Ablation with MR-guided Focused Ultrasound. In 25th Annual Meeting of the Biomedical Engineering Society, Tampa, 2015.

[82] Rieke V, Instrella R, Rosenberg J, Grissom WA, Werner B, Martin E, Butts Pauly K. Comparison of temperature processing methods for monitoring focused ultrasound ablation in the brain. J Magn Reson Imaging 2013;38:1462–1471.

[83] Chung A, Hynynen K, Colucci V, Oshio K, Cline H, Jolesz F. Optimization of spoiled gradient-echo phase imaging for in vivo localization of a focused ultrasound beam. Magnetic Resonance in Medicine 1996;36:745–752.

[84] De Zwart JA, Van Gelderen P, Kelly DJ, Moonen CTW. Fast Magnetic-Resonance Temperature Imaging. Journal of Magnetic Resonance 1996;112:86–90.

[85] Pruessmann KP, Weiger M, Scheidegger MB, Boesiger P, et al. SENSE: sensitivity encoding for fast MRI. Magnetic resonance in medicine 1999;42:952–962.

[86] Lustig M, Donoho D, Pauly JM. Sparse MRI: The application of compressed sensing for rapid MR imaging. Magn Reson Med 2007;58:1182–1195.

[87] Leonard P, Chopra R, Nachman A. Compressed Sensing for Accelerated MR Thermometry in MRI-Controlled Transurethral Ultrasound Therapy. In Proceedings of the 20th Scientific Meeting of ISMRM, Melbourne. 2012; p. 2918.

[88] Kohler MO, Tillander M, Syrja A, Nakari R, Ylihautala M. Ultrasound-transparent RF coil design for improved MR thermometry of HIFU therapy. In Proceedings of the 19th Scientific Meeting of ISMRM, Montreal. 2011; p. 1728.

[89] Minalga E, Merrill R, Todd N, Parker DL, Hadley JR. A 10-channel RF coil for use in magnetic resonance guided high intensity focused ultrasound for the brain. In Proceedings of the 21st Scientific Meeting of ISMRM, Salt Lake City. 2013; p. 832.

[90] Minalga E, Payne A, Merrill R, Todd N, Vijayakumar S, Kholmovski E, Parker DL, Hadley JR. An 11-Channel Radio Frequency Phased Array Coil for Magnetic Resonance Guided High-Intensity Focused Ultrasound of the Breast. Magn Reson Med 2013;69:295–302.

[91] Todd N, Adluru G, Payne A, DiBella EVR, Parker DL. Temporally constrained reconstruction applied to MRI temperature data. Magn Reson Med 2009;62:406–419.

[92] Roujol S, De Senneville BD, Hey S, Moonen C, Ries M. Robust adaptive extended kalman filtering for real time mr-thermometry guided hifu interventions. Medical Imaging, IEEE Transactions on 2012;31:533–542.

[93] Cao Z, Oh S, Otazo R, Sica CT, Griswold MA, Collins CM. Complex difference constrained compressed sensing reconstruction for accelerated PRF thermometry with application to MRI-induced RF heating. Magn Reson Med 2015;73:1420–1431.

[94] Sampaio LR, Simões EJ, Assis AMO, Ramos LR. Validity and reliability of the sagittal abdominal diameter as a predictor of visceral abdominal fat. Arquivos Brasileiros de Endocrinologia & Metabologia 2007;51:980–986.

[95] Bernstein MA, King KF, Zhou XJ. Handbook of MRI pulse sequences. Elsevier, 2004.

[96] Ishihara Y, Calderon A, Watanabe H, Okamoto K, Suzuki Y, Kuroda K, Suzuki Y. A precise and fast temperature mapping using water proton chemical shift. Magn Reson Med 1995;34:814–823.

[97] Hindman JC. Proton resonance shift of water in the gas and liquid states. J Chem Phys 1966;44:4582.

[98] Peters RD, Hinks RS, Henkelman RM. Ex vivo tissue-type independence in proton-resonance frequency shift MR thermometry. Magn Reson Med 1998;40:454–459.

[99] Bertsch F, Mattner J, Stehling MK, Muller-Lisse U, Peller M, Loeffler R, Weber J, Mebmer K, Wilmanns W, Issels R, Reiser M. Non-invasive temperature mapping using MRI: comparison of two methods based on chemical shift and T1-relaxation. Magn Reson Imaging 1998;16:393–404.

[100] Sprinkhuizen SM, Konings MK, van der Bom MJ, Viergever MA, Bakker CJG, Bartels LW. Temperature-induced tissue susceptibility changes lead to significant temperature errors in PRFS-based MR thermometry during thermal interventions. Magn Reson Med 2010;64:1360–1372.

[101] De Poorter J. Noninvasive MRI thermometry with the proton resonance frequency method: Study of susceptibility effects. Magn Reson Med 1995;34:359–367.

[102] Peters RD, Henkelman RM. Proton-resonance frequency shift MR thermometry is affected by changes in the electrical conductivity of tissue. Magn Reson Med 2000; 43:62–71.

[103] Salomir R, de Zwart J, Vimeux F, Quesson B, Moonen C. Temperature induced changes in magnetic susceptibility in local hyperthermia: Correction of MR thermometry. In Proceedings of the 8th Annual Meeting of ISMRM, Sydney, Australia, 2000. p. 1349.

[104] Josan S, Holbrook AB, Kaye E, Law C, Butts Pauly K. Analysis of focused ultrasound hotspot appearance on EPI and spiral MR imaging. In Proceedings of the 18th Annual Meeting of ISMRM, Stockholm, Sweden, 2010. p. 1802.

[105] Grissom WA, Rieke V, Holbrook AB, Medan Y, Pauly KB, Davis C. Chemical shift-compensated hybrid referenceless and multibaseline subtraction thermometry. In Proceedings of the 8th Interventional MRI Symposium, Leipzig, Germany, 2010.

[106] Grissom WA, Rieke V, Holbrook AB, Medan Y, Lustig M, Santos J, McConnell MV, Pauly KB. Hybrid referenceless and multibaseline subtraction MR thermometry for monitoring thermal therapies in moving organs. Med Phys 2010;37:5014–5026.

[107] Ter Haar G. Harnessing the interaction of ultrasound with tissue for therapeutic benefit: high-intensity focused ultrasound. Ultrasound in Obstetrics & Gynecology 2008;32:601–604.

[108] Khokhlova TD, Hwang JH. HIFU for palliative treatment of pancreatic cancer. Journal of gastrointestinal oncology 2011;2:175–184.

[109] Arthur R, Straube W, Trobaugh J, Moros E. Non-invasive estimation of hyperthermia temperatures with ultrasound. International journal of hyperthermia 2005;21:589–600.

[110] Larina IV, Larin KV, Esenaliev RO. Real-time optoacoustic monitoring of temperature in tissues. Journal of Physics D: Applied Physics 2005;38:2633.

[111] Damianou CA, Sanghvi NT, Fry FJ, Maass-Moreno R. Dependence of ultrasonic attenuation and absorption in dog soft tissues on temperature and thermal dose. The Journal of the Acoustical Society of America 1997;102:628–634.

[112] Bamber J, Hill C. Ultrasonic attenuation and propagation speed in mammalian tissues as a function of temperature. Ultrasound in medicine & biology 1979;5:149–157.

[113] Techavipoo U, Varghese T, Chen Q, Stiles T, Zagzebski J, Frank G. Temperature dependence of ultrasonic propagation speed and attenuation in excised canine liver tissue measured using transmitted and reflected pulses. The Journal of the Acoustical Society of America 2004;115:2859–2865.

[114] Souchon R, Bouchoux G, Maciejko E, Lafon C, Cathignol D, Bertrand M, Chapelon JY. Monitoring the formation of thermal lesions with heat-induced echo-strain imaging: A feasibility study. Ultrasound in medicine & biology 2005;31:251–259.

[115] Ter Haar GR. High intensity focused ultrasound for the treatment of tumors. Echocardiography 2001;18:317–322.

[116] Christensen D. Ultrasonic bioinstrumentation. Wiley, 1988.

[117] Nishimura DG. Principles of magnetic resonance imaging. Stanford University, 1996.

[118] Parker DL, Smith V, Sheldon P, Crooks LE, Fussell L. Temperature distribution measurements in two-dimensional nmr imaging. Medical physics 1983;10:321–325.

[119] Parker DL. Applications of NMR imaging in hyperthermia: An evaluation of the potential for localized tissue heating and noninvasive temperature monitoring. Biomedical Engineering, IEEE Transactions on 1984;31:161–167.

[120] Cline HE, Hynynen K, Schneider E, Hardy CJ, Maier SE, Watkins RD, Jolesz FA. Simultaneous magnetic resonance phase and magnitude temperature maps in muscle. Magnetic resonance in medicine 1996;35:309–315.

[121] Hynynen K, McDannold N, Mulkern RV, Jolesz FA. Temperature monitoring in fat with mri. Magnetic resonance in medicine 2000;43:901–904.

[122] Matsumoto R, Oshio K, Jolesz FA. Monitoring of laser and freezinginduced ablation in the liver with T1-weighted MR imaging. Journal of Magnetic Resonance Imaging 1992;2:555–562.

[123] Soher BJ, Wyatt C, Reeder SB, MacFall JR. Noninvasive temperature mapping with mri using chemical shift water-fat separation. Magnetic Resonance in Medicine 2010;63:1238–1246.

[124] Grissom WA, Hofstetter LW, Rieke V, Medan Y, Butts Pauly K, Davis CE. Hybrid multibaseline and referenceless PRF-shift thermometry using both water and fat images. In Proceedings 19th Scientific Meeting, International Society for Magnetic Resonance in Medicine, Montreal. 2011; p. 1771.

[125] Poorman ME, Diederich CJ, Sommer G, Butts Pauly K, Grissom WA. Model-Based Multi-Echo Water/Fat-Separated MR Thermometry. In Proceedings of the 23rd Scientific Meeting of ISMRM, Toronto. 2015; p. 0043.

[126] Hey S, De Smet M, Stehning C, Grüll H, Keupp J, Moonen C, Ries M. Simultaneous T1 measurements and proton resonance frequency shift based thermometry using variable flip angles. Magnetic resonance in medicine 2012;67:457–463.

[127] Diakite M, Odéen H, Todd N, Payne A, Parker DL. Toward real-time temperature monitoring in fat and aqueous tissue during magnetic resonance–guided high-intensity focused ultrasound using a three-dimensional proton resonance frequency T1 method. Magnetic resonance in medicine 2014;72:178–187.

[128] De Poorter J, De Wagter C, De Deene Y, Thomsen C, Stahlberg F, Achten E. Noninvasive MRI thermometry with the proton resonance frequency (PRF) method: In vivo results in human muscle. Magn Reson Med 1995;33:74–81.

[129] Vigen KK, Daniel BL, Pauly JM, Pauly KB. Triggered, navigated, multi-baseline method for proton resonance frequency temperature mapping with respiratory motion. Magn Reson Med 2003;50:1003–1010.

[130] Rieke V, Vigen KK, Sommer G, Daniel BL, Pauly JM, Butts K. Referenceless PRF shift thermometry. Magn Reson Med 2004;51:1223–1231.

[131] De Senneville BD, Roujol S, Moonen C, Ries M. Motion correction in mr thermometry of abdominal organs: a comparison of the referenceless vs. the multibaseline approach. Magnetic Resonance in Medicine 2010;64:1373–1381.

[132] de Zwart JA, van Gelderen P, Kelly DJ, Moonen CT. Fast magnetic-resonance temperature imaging. Journal of Magnetic Resonance, Series B 1996;112:86–90.

[133] Stafford RJ, Price D, Roger E, Diederich CJ, Kangasniemi M, Olsson LE, Hazle JD. Interleaved echo-planar imaging for fast multiplanar magnetic resonance temperature imaging of ultrasound thermal ablation therapy. Journal of Magnetic Resonance Imaging 2004;20:706–714.

[134] Kickhefel A, Roland J, Weiss C, Schick F. Accuracy of real-time mr temperature mapping in the brain: a comparison of fast sequences. Physica Medica 2010;26:192–201.

[135] Glover GH, Lai S. Self-navigated spiral fmri: Interleaved versus single-shot. Magnetic Resonance in Medicine 1998;39:361–368.

[136] Stafford RJ, Hazle JD, Glover GH. Monitoring of high-intensity focused ultrasound-induced temperature changes in vitro using an interleaved spiral acquisition. Magnetic resonance in medicine 2000;43:909–912.

[137] Fielden S, Feng X, Miller W, Pauly KB, Meyer C. Real-time 3D spiral MR thermometry. In Proceedings of the 23rd Scientific Meeting of ISMRM, Toronto. 2015; p. 1631.

[138] Marx M, Butts Pauly K. Improved mri thermometry with multiple-echo spirals. Magnetic resonance in medicine 2015;.

[139] Van Vaals JJ, Brummer ME, Thomas Dixon W, Tuithof HH, Engels H, Nelson RC, Gerety BM, Chezmar JL, Den Boer JA. "keyhole" method for accelerating imaging of contrast agent uptake. Journal of Magnetic Resonance Imaging 1993;3:671–675.

[140] Webb AG, Liang ZP, Magin RL, Lauterbur PC. Applications of reduced-encoding mr imaging with generalized-series reconstruction (rigr). Journal of Magnetic Resonance Imaging 1993;3:925–928.

[141] Stafford RJ, Hazle JD. Fast magnetic resonance thermal imaging using dynamic updating of spiral interleaves. In Engineering in Medicine and Biology Society, 2000. Proceedings of the 22nd Annual International Conference of the IEEE. IEEE, volume 1, 2000; pp. 47–50.

[142] Marx M, Butts Pauly K. Use of Compressed Sensing for Acceleration of Volumetric MR Thermometry. In ISMRM Workshop on Data Sampling & Image Reconstruction, Sedona. 2013; .

[143] Zhao F, Noll DC, Nielsen JF, Fessler JA. Separate magnitude and phase regularization via compressed sensing. IEEE Trans Med Imaging 2012;31:1713–1723.

[144] Todd N, Prakash J, Odeen H, De Bever J, Payne A, Yalavarthy P, Parker DL. Toward real-time availability of 3D temperature maps created with temporally constrained reconstruction. Magnetic Resonance in Medicine 2013;71:1394–1404.

[145] Odeen H, Todd N, Diakite M, Minalga E, Payne A, Parker DL. Sampling strategies for subsampled segmented EPI PRF thermometry in MR guided high intensity focused ultrasound. Med Phys 2014;41:092301.

[146] de Zwart J, Salomir R, Vimeux F, Klaveness J, Moonen C. On the feasibility of local drug delivery using thermo-sensitive liposomes and MR-guided focused ultrasound. In Proceedings of the 8th Scientific Meeting of ISMRM, Sydney. 2000; p. 43.

[147] Hynynen K, McDannold N, Vykhodtseva N, Jolesz F. Noninvasive MR Imaging-guided Focal Opening of the Blood-Brain Barrier in Rabbits. Radiology 2001; 220:640–646.

[148] Reinhard M, Hetzel A, Krüger S, Kretzer S, Talazko J, Ziyeh S, Weber J, Els T. Blood-brain barrier disruption by low-frequency ultrasound. Stroke 2006;37:1546–1548.

[149] Yuan J, Mei CS, Panych LP, McDannold NJ, Madore B. Towards fast and accurate temperature mapping with proton resonance frequency-based MR thermometry. Quant Imaging Med Surg 2012;2:21–32.

[150] Griswold MA, Jakob PM, Heidemann RM, Nittka M, Jellus V, Wang J, Kiefer B, Haase A. Generalized autocalibrating partially parallel acquisitions (GRAPPA). Magn Reson Med 2002;47:1202–1210.

[151] Weidensteiner C, Kerioui N, Quesson B, Denis de Senneville B, Trillaud H, Moonen CTW. Stability of real-time MR temperature mapping in healthy and diseased human liver. J Magn Reson Imaging 2004;19:438–446.

[152] Bankson JA, Stafford RJ, Hazle JD. Partially parallel imaging with phase-sensitive data: Increased temporal resolution for magnetic resonance temperature imaging. Magn Reson Med 2005;53:658–665.

[153] Guo JY, Kholmovski EG, Zhang L, Jeong EK, Parker DL. K-space Inherited Parallel Acquisition (KIPA): application on dynamic magnetic resonance imaging thermometry. Magn Reson Med 2006;24:903–915.

[154] Streicher MN, Schafer A, Muller D, Kogler C, Reimer E, Dhital B, Trampel R, Rivera D, Pampel A, Ivanov D, Turner R. Frequency-selective asymmetric spin-echo EPI with parallel imaging for fast internally referenced MR Thermometry. In Proceedings of the 19th Scientific Meeting of ISMRM, Montreal. 2011; p. 529.

[155] Gaur P, Grissom WA. Direct reconstruction of proton resonance frequency-shift temperature maps from k-space data for highly accelerated thermometry. In Proceedings of the 21st Scientific Meeting of ISMRM, Salt Lake City. 2013; p. 1805.

[156] Gaur P, Grissom WA. MRI temperature map reconstruction from highly undersampled data. In 13th International Symposium on Therapeutic Ultrasound, Shanghai. 2013; .

[157] Holbrook AB, Ghanouni P, Santos JM, Medan Y, Pauly KB. In vivo MR acoustic radiation force imaging in the porcine liver. Med Phys 2011;38:5081.

[158] Pruessmann KP, Weiger M, Börnert P, Boesiger P. Advances in sensitivity encoding with arbitrary k-space trajectories. Magn Reson Med 2001;46:638–651.

[159] Fessler JA, Sutton BP. Nonuniform fast fourier transforms using min-max interpolation. IEEE Trans Signal Process 2003;51:560–574.

[160] Sutton BP, Noll DC, Fessler JA. Fast, iterative image reconstruction for MRI in the presence of field inhomogeneities. IEEE Trans Med Imaging 2003;22:178–188.

[161] Lustig M, Pauly JM. SPIRiT: Iterative Self-consistent Parallel Imaging Reconstruction From Arbitrary k-Space. Magn Reson Med 2010;64:457–471.

[162] Wright SM. 2D Full Wave Modeling of SENSE Coil Geometry Factors at High Fields. In Proceedings of the 10th Scientific Meeting of ISMRM, Honolulu. 2002; p. 854.

[163] Funai AK, Fessler JA, Yeo D, Olafsson VT, Noll DC. Regularized field map estimation in MRI. IEEE Trans Med Imaging 2008;27:1484–1494.

[164] de Zwart JA, Vimeux FC, Delalande C, Canioni P, Moonen CT. Fast lipid-suppressed MR temperature mapping with echo-shifted gradient-echo imaging and spectral-spatial excitation. Magn Reson Med 1999;42:53–59.

[165] Gaur P, Grissom WA. Temperature map reconstruction directly from k-space with compensation for heating-induced geometric distortions. In Proceedings 22nd Scientific Meeting, International Society for Magnetic Resonance in Medicine, Milan. 2014; p. 2362.

[166] Todd N, Vyas U, de Bever J, Payne A, Parker D. Reconstruction of fully three-dimensional high spatial and temporal resolution MR temperature maps for retrospective applications. Magn Reson Med 2012;67:724–730.

[167] Gaur P, Grissom WA. Accelerated MRI thermometry by direct estimation of temperature from undersampled k-space data. Magn Reson Med 2015;73:1914–1925.

[168] Allen JS, Damasio H, Grabowski TJ. Normal neuroanatomical variation in the human brain: An MRI-volumetric study. American journal of physical anthropology 2002;118:341–358.

[169] Rothstein EL, Hartzell R, Manson L, Kritchevsky D. Effects of D_2O on cellular components of mammalian cells grown in tissue culture. Annals of the New York Academy of Sciences 1960;84:721–726.

[170] Gross PR, Harding CV. Blockade of deoxyribonucleic acid synthesis by deuterium oxide. Science 1961;133:1131–1133.

[171] Hartmann J, Bader Y, Horvath Z, Saiko P, Grusch M, Illmer C, Madlener S, Fritzer-Szekeres M, Heller N, Alken RG, et al. Effects of heavy water (D_2O) on human pancreatic tumor cells. Anticancer research 2005;25:3407–3411.

[172] Kushner D, Baker A, Dunstall T. Pharmacological uses and perspectives of heavy water and deuterated compounds. Canadian journal of physiology and pharmacology 1999;77:79–88.

[173] Neimatallah MA, Chenevert TL, Carlos RC, Londy FJ, Dong Q, Prince MR, Kim HM. Subclavian MR arteriography: Reduction of susceptibility artifact with short echo time and dilute gadopentetate dimeglumine 1. Radiology 2000;217:581–586.

[174] Parker DL, Goodrich KC, Alexander AL, Buswell HR, Blatter DD, Tsuruda JS. Optimized visualization of vessels in contrast enhanced intracranial MR angiography. Magnetic resonance in medicine 1998;40:873–882.

[175] Sasaki M, Shibata E, Kanbara Y, Ehara S. Enhancement effects and relaxivities of

gadolinium-dtpa at 1.5 versus 3 tesla: a phantom study. Magnetic Resonance in Medical Sciences 2005;4:145–149.

[176] Roberts A. Magnetic resonance-guided focused ultrasound for uterine fibroids. In Seminars in interventional radiology. Thieme Medical Publishers, volume 25, 2008; p. 394.

[177] Feshitan JA, Vlachos F, Sirsi SR, Konofagou EE, Borden MA. Theranostic gd (iii)-lipid microbubbles for mri-guided focused ultrasound surgery. Biomaterials 2012; 33:247–255.

[178] Peters RD, Hinks RS, Henkelman RM. Heat-source orientation and geometry dependence in proton-resonance frequency shift magnetic resonance thermometry. Magn Reson Med 1999;41:909–918.

[179] Baron P, Deckers R, de Greef M, Merckel LG, Bakker CJG, Bouwman JG, Bleys RLAW, van den Bosch MAAJ, Bartels LW. Correction of proton resonance frequency shift MR-thermometry errors caused by heat-induced magnetic susceptibility changes during high intensity focused ultrasound ablations in tissues containing fat. Magn Reson Med 2014;72:1580–89.

[180] Enholm JK, Köhler MO, Quesson B, Mougenot C, Moonen CTW, Sokka SD. Improved volumetric MR-HIFU ablation by robust binary feedback control. Biomedical Engineering, IEEE Transactions on 2010;57:103–113.

[181] de Senneville BD, Quesson B, Desbarats P, Salomir R, Palussiere J, Moonen CTW. Atlas-based motion correction for on-line MR temperature mapping. In Proceedings of IEEE ICIP, 2004. p. 2571–2574.

[182] de Senneville BD, Mougenot C, Moonen CTW. Real-time adaptive methods for treatment of mobile organs by MRI-controlled high-intensity focused ultrasound. Magn Reson Med 2007;57:319–330.

[183] Dragonu I, de Senneville BD, Quesson B, Moonen C, Ries M. Real-time geometric distortion correction for interventional imaging with echo-planar imaging (EPI). Magn Reson Med 2009;61:994–1000.

[184] Jezzard P, Balaban RS. Correction for geometric distortion in echo planar images from B_0 field variations. Magn Reson Med 1995;34:65–73.

[185] Noll DC, Schneider W. Theory, simulation, and compensation of physiological motion artifacts in functional MRI. In Image Processing, 1994. Proceedings. ICIP-94., IEEE International Conference. IEEE, volume 3, 1994; pp. 40–44.

[186] Glover GH, Li TQ, Ress D. Image-based method for retrospective correction of physiological motion effects in fMRI: RETROICOR. Magnetic Resonance in Medicine 2000;44:162–167.

[187] Dagli MS, Ingeholm JE, Haxby JV. Localization of cardiac-induced signal change in fMRI. Neuroimage 1999;9:407–415.

[188] Otazo R, Candès E, Sodickson DK. Low-rank plus sparse matrix decomposition for accelerated dynamic MRI with separation of background and dynamic components. Magnetic Resonance in Medicine 2015;73:1125–1136.

[189] Doneva M, Börnert P, Eggers H, Stehning C, Sénégas J, Mertins A. Compressed sensing reconstruction for magnetic resonance parameter mapping. Magnetic Resonance in Medicine 2010;64:1114–1120.

[190] Watkins RD, Cline HE. Thermal imaging of fat and muscle using a simultaneous phase and magnitude double echo sequence, 2003. US Patent 6,618,608.

[191] Hernando D, Kellman P, Haldar J, Liang ZP. Robust water/fat separation in the presence of large field inhomogeneities using a graph cut algorithm. Magnetic Resonance in Medicine 2010;63:79–90.

[192] Berglund J, Kullberg J. Three-dimensional water/fat separation and T_2^* estimation based on whole-image optimization—Application in breathhold liver imaging at 1.5 T. Magnetic Resonance in Medicine 2012;67:1684–1693.

[193] Hu HH, Börnert P, Hernando D, Kellman P, Ma J, Reeder S, Sirlin C. ISMRM workshop on fat–water separation: insights, applications and progress in MRI. Magnetic Resonance in Medicine 2012;68:378–388.

[194] Sprinkhuizen SM, Bakker CJ, Ippel JH, Boelens R, Viergever MA, Bartels LW. Temperature dependence of the magnetic volume susceptibility of human breast fat tissue: an nmr study. Magnetic Resonance Materials in Physics, Biology and Medicine 2012;25:33–39.

[195] Björk M, Berglund J, Kullberg J, Stoica P. Signal modeling and the cramér-rao bound for absolute magnetic resonance thermometry in fat tissue. In Signals, Systems and Computers (ASILOMAR), 2011 Conference Record of the Forty Fifth Asilomar Conference on. IEEE, 2011; pp. 80–84.

[196] Sprinkhuizen SM, Bakker CJ, Bartels LW. Absolute mr thermometry using time-domain analysis of multi-gradient-echo magnitude images. Magnetic resonance in medicine 2010;64:239–248.

[197] Welch E, Gifford A, Towse T. Phantom validation of temperature mapping using fat-water mri with explicit fitting of water peak location. In Proceedings 22nd Scientific Meeting, International Society for Magnetic Resonance in Medicine, Milan. volume 22, 2014; p. 3065.

[198] Gifford A, Towse T, Avison M, Welch E. Temperature mapping in human brown adipose tissue using fat-water mri with explicit fitting of water peak location. In Proceedings 22nd Scientific Meeting, International Society for Magnetic Resonance in Medicine, Milan 22nd Annual Meeting of ISMRM. 2014; p. 2354.

[199] Ma D, Gulani V, Seiberlich N, Liu K, Sunshine JL, Duerk JL, Griswold MA. Magnetic resonance fingerprinting. Nature 2013;495:187–192.